

Dissertation
submitted to the
Combined Faculties for the Natural Sciences and for Mathematics
of the Ruperto–Carola University of Heidelberg, Germany
for the degree of
Doctor of Natural Sciences

presented by
M.Sc. Bo Zhao
born in Donggang Liaoning (P. R. China)

Oral examination: July 16th 2008

Robust and Efficient Quantum Repeater with Atomic Ensembles and Linear Optics

Referees: Prof. Dr. Jian-Wei Pan
Prof. Dr. Peter Schmelcher

Zusammenfassung

Robuste und effiziente Quanten-repeater mit atomaren Ensembles und linearer Optik

Die Arbeit, die in dieser Dissertation vorgestellt wird, untersucht theoretisch und experimentell die Quantenkommunikation über lange Strecken (long-distance quantum communication) mit atomaren Ensembles und linearer Optik. Ein robustes und effiziente Quantenrepeaterarchitektur aufbauend auf einem Originalprotokoll von Duan-Lukin-Cirac-Zoller (DLCZ) wird vorgestellt. Die neue Architektur basiert auf der Zweiphotonen Hong-Ou-Mandel-typischen Interferenz, um so die Anforderungen an die Stabilität über weite Entfernungen um circa 7 Größenordnungen zu reduzieren. Darüber hinaus verwenden wir die nichtklassischen Korrelationen um eine deterministische Einzelphotonenquelle, den Hong-Ou-Mandel Dip zwischen zwei einzelnen Photonen, einen Quantenspeicher mit langer Lebenszeit in einer optischen Dipolfalle und die Quantenteleportation zwischen einem Photon als Qubit und einem atomaren Speicherqubit zu demonstrieren. Abschließend wird mithilfe einer neuen Quelle zur Verschränkung von atomaren Ensembles und Photonen ein Baustein für einen robusten Quantenrepeater realisiert. Der theoretische und experimentelle Fortschritt, der in dieser Arbeit dargestellt wird, erlaubt die zuverlässige Implementierung eines robusten Quantenrepeaters und öffnet einen realistischen Weg für die relevante Quantenkommunikation über lange Strecken.

Abstract

Robust and efficient quantum repeater with atomic ensembles and linear optics

The work presented in this thesis is the theoretical and experimental investigation of long-distance quantum communication with atomic ensembles and linear optics. A robust and efficient quantum repeater architecture building on the original Duan-Lukin-Cirac-Zoller protocol (DLCZ) is proposed. The new architecture is based on two-photon Hong-Ou-Mandel-type interference, which relaxes the long distance stability requirements by about 7 orders of magnitude. Moreover, by exploiting the local generation of quasi-ideal entangled pair, the new architecture is much faster than all the previous protocols with similar ingredients. We then report our recent experimental efforts towards the quantum repeater with atomic ensembles and linear optics. By exploiting the nonclassical correlation, we demonstrated a deterministic single photon source, Hong-Ou-Mandel dip between two single photons, long-lived quantum memory with optical trap, and quantum teleportation between a photonic qubit and a memory qubit. Moreover, by the aid of the new atom-photon entanglement source, a building block of the robust quantum repeater is realized. The theoretical and experimental progress presented in this work allows a faithfully implementation of a robust quantum repeater, and enables a realistic avenue for relevant long-distance quantum communication.

Contents

Abstract	i
Contents	iii
List of figures	vii
List of Tables	xv
1 Introduction	1
1.1 Quantum computation	1
1.2 Quantum communication	2
1.2.1 Quantum cryptography	2
1.2.2 Quantum repeater	3
1.3 The objective of this work.	4
2 Atomic memory for a quantum repeater	7
2.1 Introduction	7
2.2 Spontaneous Raman scattering	8
2.3 Retrieval of the stored collective excitation	12
2.4 The nonclassical correlation	15
3 Duan-Lukin-Cirac-Zoller protocol and the drawbacks	17
3.1 Introduction	17
3.2 Basic protocol	18
3.3 Phase stabilization problem	20
3.3.1 Phase instability analysis I	20
3.3.2 Phase instability analysis II	22
3.4 The scalability analysis	24
4 Robust creation of entanglement between remote memory qubits	27
4.1 Introduction	27
4.2 Entanglement generation	28
4.3 Entanglement connection and scalability	32
4.4 Entanglement purification	33
4.5 Discussion	34
5 A fast quantum repeater with high-quality local entanglement	37
5.1 Introduction	37
5.2 Locally generated quasi-ideal entangled pair	39
5.3 Repeater Protocol	43
5.4 Implementation	45

6	Deterministic single-photon source based on a quantum memory	49
6.1	Introduction	49
6.2	Basic protocol	50
6.3	Experiment	52
6.4	Discussion	58
7	Synchronized independent narrow-band single photons	59
7.1	Introduction	59
7.2	Experiment	60
7.2.1	Theoretical description of HOM dip	63
7.2.2	The measurement of HOM dip	64
7.2.3	Time resolved two-photon interference	66
7.2.4	Test Bell inequality	66
7.3	Discussion	67
8	Quantum teleportation between photonic and atomic qubits	69
8.1	Introduction	69
8.2	Experimental scheme	70
8.3	Experimental realization	72
8.3.1	Preparation of the entanglement	72
8.3.2	Phase locking	73
8.3.3	Experimental results	74
8.4	Noise estimation	75
8.4.1	Bell-state measurement	75
8.4.2	Teleportation fidelity	76
8.5	Conclusion	77
9	Demonstration of a stable atom-photon entanglement source	79
9.1	Introduction	79
9.2	Experimental scheme	80
9.3	Characterization of atom-photon entanglement	82
9.3.1	Entanglement visibility	82
9.3.2	Storage of entanglement	84
9.4	Discussion	86
10	Entanglement swapping between Light and matter	87
10.1	Introduction	87
10.2	Experiment	89
10.2.1	Atom-photon entanglement source	89
10.2.2	Entanglement swapping	92
10.2.3	Phase stabilization method	95
10.3	Conclusion	96
11	Quantum memory with optically trapped atoms	99
11.1	Introduction	99
11.2	Experiment	100
11.3	Discussion	105
12	A long-lived quantum memory for scalable quantum networks	107
12.1	Introduction	107
12.2	Experiment	108
12.3	Discussion	114
13	Conclusion and outlook	115
	Appendix: Associated Publications	117

Acknowledgement	119
Bibliography	121

List of Figures

1.1	An illustration of the quantum repeater protocol. The communication distance is extended by entanglement swapping, and the fidelity of the entangled pair is improved by entanglement purification.	4
2.1	An illustration of the interaction between atomic ensemble and light. The excited state $ e\rangle$, and two ground states $ g\rangle$ and $ s\rangle$ form the Λ -type three-level atom. In the write process, an off resonant write light pulse with Rabi frequency Ω_w and detune Δ is applied to the atomic ensemble. A Stokes photon is emitted and simultaneously a collective excitation is generated due to spontaneous Raman scattering. In the EIT-based read process, an on resonance read light pulse with Rabi frequency Ω_R is applied to convert the collective excitation to an anti-Stokes photon.	8
2.2	A schematic view of the write process. The Stokes light is emitted along all the directions in the spontaneous Raman scattering process. The Stokes light in the blue cone can be treated as one mode if we detect the scattered light along the axial direction.	11
2.3	A schematic view of the read process. The anti-Stokes light is emitted along the backward direction where the mode match condition is satisfied. Constructive interference occurs in the red cone.	12
3.1	Setups for entanglement generation and entanglement swapping in the DLCZ protocol. (a) Forward scattered Stokes photons, generated by an off-resonant write laser pulse via spontaneous Raman transition, are directed to the beam splitter (BS) at the middle point. Entanglement is generated between atomic ensembles at sites a and b , once there is a click on either of the detectors. (b) Entanglement has been generated between atomic ensembles (a, b^L) and (b^R, c) . The atomic ensembles at site b are illuminated by near resonant read laser pulses, and the retrieved anti-Stokes photons are subject to the BS at the middle point. A click on either of the detectors will prepare the atomic ensembles at a and c into an entangled state	18
3.2	In the DLCZ protocol, two entangled pairs are generated in parallel. The relative phase between the two entangled states has to be stabilized during the entanglement generation process.	21
3.3	Elementary entangled pairs are created locally. Entanglement swapping is performed remotely to connect atomic ensembles between adjacent nodes a and b	22
3.4	Entangled pairs are generated between neighboring communication nodes as shown in Fig. 3.3. The entangled pairs are connected by performing further entanglement swapping to construct entanglement between remote communication sites A and B . The entanglement connection process, as well as the accumulated phase, is shown step by step.	23
3.5	Entanglement distribution rate as a function of the communication distance.	25

4.1	Setup for entanglement generation between sites A and B . Forward-scattered Stokes photons, generated by an off-resonant write laser pulse via spontaneous Raman transition, are subject to BSM-I at the middle point. The Stokes photons generated at the same site are assumed to have different polarization, i.e., $ H\rangle$ and $ V\rangle$. PBS (PBS_{\pm}) reflects photons with polarization $ V\rangle$ ($ -\rangle$) and transmits photons with polarization $ H\rangle$ ($ +\rangle$), where $ \pm\rangle = \frac{1}{\sqrt{2}}(H\rangle \pm V\rangle)$. After passing through the PBS_{\pm} and PBS successively, the Stokes photons are detected by single photon detectors. A coincidence count between single photon detectors D_1 and D_4 (D_1 and D_3) or D_2 and D_3 (D_2 and D_4) will project the four atomic ensembles into the complex entangled state $ \psi\rangle_{AB}$ up to a local unitary transformation.	29
4.2	Setup for entanglement connection between sites A and C via entanglement swapping. Complex entangled states have been prepared in the memory qubits between sites (A, B_L) and (B_R, C) . The memory qubits at site B are illuminated by near resonant read laser pulses, and the retrieved anti-Stokes photons are subject to BSM-II at the middle point. The anti-Stokes photons at the same site have different polarizations $ H\rangle$ and $ V\rangle$. After passing through PBS and PBS_{\pm} successively, the anti-Stokes photons are detected by single photon detectors. Coincidence counts between D_1 and D_4 (D_1 and D_3) or D_2 and D_3 (D_2 and D_4) are registered. The memory qubits will be projected into an effectively maximally entangled state ρ_{AC} up to a local unitary transformation. Note that the sequence of PBSs in BSM-II is different from BSM-I. This helps to eliminate the spurious contributions from second-order excitations.	30
4.3	Setup for quantum entanglement purification. Effectively entangled states have been prepared in the memory qubits between two distant sites I and J . The memory qubits at the two sites are illuminated by near resonant read laser pulse, and the retrieved entangled photon pairs are directed to two PBS respectively. The photons in modes b_1 and b_2 are detected in $ \pm\rangle = \frac{1}{\sqrt{2}}(H\rangle \pm V\rangle)$ basis and the left photons in modes a_1 and a_2 are restored in the memory qubits at the two sites respectively.	34
5.1	Deterministic single-photon polarization entangler. PBS (PBS_{\pm} ; $\text{PBS}_{R/L}$) reflects photons with vertical polarization $ V\rangle$ ($ -\rangle$; $ L\rangle$) and transmits photons with horizontal-polarization $ H\rangle$ ($ +\rangle$; $ R\rangle$). Here $ \pm\rangle = \frac{1}{\sqrt{2}}(H\rangle + V\rangle)$; $ R/L\rangle = \frac{1}{\sqrt{2}}(H\rangle \pm i V\rangle)$. The four single photons are prepared on demand in an initial state $ -\rangle_1 V\rangle_2 +\rangle_{1'} H\rangle_{2'}$. After passing through the first PBS and PBS_{\pm} , one selects the ‘four-mode’ case where there is one and only one photon in each of the four output modes. Then the BSM will collapse photons in modes a and b into a Bell state conditioned on the result of the BSM. In our case, a coincidence count between single-photon detectors D_1 and D_4 (D_1 and D_3) or between D_2 and D_3 (D_2 and D_4) leaving photons along paths a and b deterministically entangled in $ \psi^+\rangle_{ab}(\phi^-\rangle_{ab})$	39
5.2	Quantum memory for photonic polarization qubits. Two ensembles are driven by a classical control field. Classical and quantized light fields are fed into the first PBS and will leave at two different outputs of the second PBS. As each atomic cell works as quantum memory for single photons with polarization $ H\rangle$ or $ V\rangle$ via the adiabatic transfer method, the whole setup is then quantum memory of any single-photon polarization states. The inset shows the relevant level structure of the atoms. The $ e\rangle - s\rangle$ transition is coherently driven by the classical control field of Rabi frequency Ω_c , and the $ g\rangle - e\rangle$ transition is coupled to a quantized light field.	40

5.3	Setup for generating high-fidelity entangled pairs of atomic excitations. Yellow squares represent atomic ensembles which probabilistically emit Stokes photons (green dots). The conditional detection of a single Stokes photon heralds the storage of one atomic spin-wave excitation. In this way an atomic excitation is created and stored independently in each ensemble. Then all four ensembles are simultaneously read out partially, creating a probability amplitude to emit an anti-Stokes photon (red dots). The coincident detection of two photons in d_+ and \tilde{d}_+ projects non-destructively the atomic cells into the entangled state $ \Phi_{ab}\rangle$ of Eq. (5.5); $d_+-\tilde{d}_-$, $d_--\tilde{d}_+$, and $d_--\tilde{d}_-$ coincidences, combined with the appropriate one-qubit transformations, also collapse the state of the atomic cells into $ \Phi_{ab}\rangle$. Half-circles represent photon detectors. Vertical bars within squares label polarizing beam splitters (PBS) that transmit (reflect) H (V)-polarized photons. The central PBS with a circle performs the same action in the $\pm 45^\circ$ ($H + V/H - V$) basis.	42
5.4	(A) Long-distance entanglement creation using two four-ensemble sources as shown in Fig. 5.3. The A and D ensembles are entangled by the detection of two photons emitted from the B and C ensembles, using the same setup as in chapter 4. Note that the AB source is separated from the CD source by a long distance. (B) Entanglement swapping. The same set of linear optical elements allows one to entangle the A and H ensembles belonging to two adjacent elementary links. Note that the D and E ensembles are at the same location.	44
5.5	Comparison of different quantum repeater protocols that all use only atomic ensembles and linear optics. The quantity shown is the average time needed to distribute a single entangled pair for the given distance. A: as a reference, the time required using direct transmission of photons through optical fibers, with losses of 0.2 dB/km, corresponding to the best available telecom fibers at a wavelength of 1.5 μm , and a pair generation rate of 10 GHz. B: the original DLCZ protocol that uses single-photon detections for both entanglement generation and swapping. C: The protocol that uses quasi-ideal single photon sources (which can be implemented with atomic ensembles, cf. text) plus single-photon detections for generation and swapping. D: The protocol that locally generates high-fidelity entangled pairs by using four single photons. E: the proposed new protocol which uses an improved method of partial retrieval to generate local entanglement. For all the curves we have assumed memory and detector efficiencies of 90%. The numbers of links in the repeater chain are optimized for curves B and C, e.g. giving 4 links for 600 km and 8 links for 1000 km for both protocols. For curves D and E, we imposed a maximum number of 16 links (cf. text), which is used for all distances greater than 400 km.	46
6.1	(a) Illustration of the experimental setup and (b) the time sequence with the feedback circuit for the write and read process. The atomic ensemble is firstly prepared in the initial state $ a\rangle$ by applying a pump beam resonant with the transition $ b\rangle$ to $ e'\rangle$. A write pulse with the Rabi frequency Ω_w is applied to generate the spin excitation and an accompanying photon of the mode \hat{a}_{AS} . Waiting for a duration Δt , a read pulse is applied with orthogonal polarization and spatially overlap with the write beam in PBS1. The photons, whose polarization is orthogonal to that of the write beam, in the mode \hat{a}_{AS} are spatially extracted from the write beam by PBS2 and detected by detector D1. Similarly, the field \hat{a}_s is spatially extracted from the Read beam and detected by detector D2 (or D3). Here, FC1 and FC2 are two filter cells, BS is a 50/50 beamsplitter, and AOM1 and AOM2 are two acousto-optic modulators.	53
6.2	Intensity correlation function $g_{AS,S}^{(2)}$ along the excitation probability p_{AS} with $\delta t = 500$ ns (a) and along the time delay δt between read and write pulses with $p_{AS} = 3 \times 10^{-3}$ (b). The black dots are obtained from current experiment and the curves correspond to a least-square fit procedure according to Eq. (6.18). The observed lifetime is $\tau_c = 12.5 \pm 2.6 \mu\text{s}$	55

6.3	The anti-correlation parameter as a function of p_{AS} (a) and Δt (b). In panel (a), the data in black correspond to the experiment without feedback circuit, in which each write sequence is followed by one read pulse. The data in red corresponds to the experiment with feedback circuit, in which 12 successive write sequences are followed by one read pulse. The red curve is the theoretical evaluation taking into account the fitted background of the black dots. In panel (b), 12 write sequences were applied in each trial while measuring.	57
7.1	Illustration of the relevant energy levels of the atoms and arrangement of laser beams (a) and the experimental setup (b). Alice and Bob each keeps a single-photon source at two remote locations. As elucidated in chapter 6, Alice applies write pulses continuously until an anti-Stokes photon is registered by detector D1. Then she stops the write pulse, holds the spin excitations and meanwhile sends a synchronization signal to Bob and waits for his response (This is realized by the feedback circuit and the acousto-optic modulators, AOM). In parallel Bob prepares a single excitation in the same way as Alice. After they both agree that each has a spin excitation, each of them will apply a read pulse simultaneously to retrieve the spin excitation into a light field \hat{a}_S . The two Stokes photons propagate to the place for entanglement generation and Bell measurement. They overlap at a 50:50 beam splitter (BS) and then will be analyzed by latter half-wave plates ($\lambda/2$), polarized beam splitters (PBS) and single photon detectors Da, Db, Dc, and Dd.	61
7.2	Hong-Ou-Mandel dips in time domain (upper panel) and frequency domain (lower panel). The circle in the lower panel was obtained by setting the polarization of the two photons perpendicular to each other and zero detuning between two read lasers. The Gaussian curves that roughly connect the data points are only shown to guide the eye. The dashed line shows the plateau of the dip. Error bars represent statistical errors, which are ± 1 standard deviation.	65
7.3	Hong-Ou-Mandel dips in time domain with coincidence window (2 ns) much shorter than the wave-packet length. The red spots are measured under perpendicular polarization and the black ones are measured under parallel cases.	67
8.1	Experimental setup for teleportation between photonic and atomic qubits. The inset shows the structure and the initial populations of atomic levels for the two ensembles. At Bob's site the anti-Stokes fields emitted from U and D are collected and combined at PBS ₁ , selecting perpendicular polarizations. Then the photon travels 7 m through fibers to Alice's side to overlap with the initial unknown photon on a beam-splitter (BS) to perform the BSM. The results of the BSM are sent back to Bob via a classical channel. Bob can then perform the verification of the teleported state in the U and D ensembles by converting the atomic excitation to a photonic state. A unitary operation on the converted photon is performed according to the classical information from the results of BSM.	71
8.2	Schematic drawing of the phase locking setup. Two Mach-Zehnder interferometers are used to actively stabilize the phases between the arms of write and read paths (a) and between the arms of anti-Stokes and Stokes paths (b), respectively. H/V denotes the horizontal/vertical polarization, and AOM denotes an acousto-optic modulator. A polarizer (Pol.) is set at 45° to erase the polarization information. The HWPs ($\lambda/2$) are set at 45° as well to rotate the horizontal polarization to vertical. AS (S) denotes the anti-Stokes (Stokes) photon.	74
8.3	Fidelity of the teleported state in atomic ensembles along storage time. The initial state to be teleported is $(H\rangle + i V\rangle)/\sqrt{2}$. Until $8 \mu s$ the fidelity is still well beyond the classical limit of $2/3$. Each experimental point is measured for about four hours (averagely). The curve is a Gaussian fit, due to the Gaussian decay of the retrieve efficiency. The error bars represent the statistical error, i.e., ± 1 standard deviation.	75

9.1	Illustration of the experimental scheme and the relevant energy levels of the ^{87}Rb atoms. Cold ^{87}Rb atoms captured by MOT are initially prepared in state $ a\rangle$. A weak write pulse Ω_w with a beam waist of $240\ \mu\text{m}$ illuminates the atom cloud to generate the spin excitation. The spontaneous Raman scattered anti-Stokes field AS_L and AS_R are detected at $\pm 3^\circ$ to the propagating direction of the write beam, with the beam waist of $70\ \mu\text{m}$, defining the spatial mode of the atomic ensembles L and R , respectively. The two anti-Stokes field are combined on a polarizing beam splitter PBS_1 and sent to the polarization analyzer. This creates the entanglement between the polarization of the anti-Stokes field and the spatial modes of spin excitation of atoms in atomic ensemble. To verify the entanglement after a storage time τ , a vertical polarized read pulse counter-propagating with write pulse is applied to retrieve the spin excitation to the Stokes fields S_L and S_R . The polarization of S_L is rotated by 90° , combined with S_R on PBS_2 and sent to the polarization analyzer.	81
9.2	Visibility of the interference fringes V between anti-Stokes fields and Stokes fields versus the changing of the detected rate of anti-Stokes field p_{AS} . The solid line is the fit corresponding to Eq. (9.5). The dashed line shows the bound of $1/\sqrt{2}$ which marks the limit to violate the CHSH-type Bell inequality.	83
9.3	The decay of retrieve efficiency and cross correlation $g_{12}^{(2)}$ with the storage time τ . The anti-Stokes detection rate is fixed at $p_{AS} = 2 \times 10^{-3}$. The square dots show the decay process of the retrieve efficiency of the Stokes fields, round dots show the decay of the cross correlation $g_{AS,S}^{(2)}$ between anti-Stokes field and Stokes field.	84
9.4	Decay of the S parameter in the Bell inequality measurement with the storage time τ . The dashed line shows the classical bound of $S = 2$	85
10.1	The experimental scheme for entanglement swapping. Upper Panel: photons 2 and 3 overlap at BSM through which the entanglement is generated between the two atomic ensembles I and II. Lower-left Panel: energy levels $\{ a\rangle, b\rangle, e\rangle\} = \{ 5S_{1/2}, F = 2\rangle, 5S_{1/2}, F = 1\rangle, 5P_{1/2}, F = 2\rangle\}$ and the configuration of light beams. Lower-right Panel: the time sequence of the experimental procedure at each site. For 6 m (300 m) fiber connection, there are 250 (200) experiment cycles in 5 ms and ΔT is 16 μs (20 μs) for one cycle which contains $N=10$ ($N=8$) write sequences. The interval between two neighboring write pulses is $\delta t_w = 1\ \mu\text{s}$ (1.5 μs) and δt_s is the storage time. Whenever there is a desired coincidence event between photons 2 and 3, the following write sequence is stopped by a feedback circuit and the retrieve process can be started. Abbreviations: PBS–Polarizing beam splitter, HWP–Half-wave plate, M–Mirror, SMF–single mode fiber.	89
10.2	The decay of cross correlation $g_{AS,S}^{(2)}$ with the storage time. The detection probability of anti-Stokes photons is fixed at 2×10^{-3}	91
10.3	Decay of the S parameter in the Bell inequality with the storage time at excitation rate of 2×10^{-3} . The solid squares are the measured data and the circles are calculated from the correlation function $g_{AS,S}^{(2)}$. The dashed line shows the classical bound of $S = 2$	92
10.4	Correlation functions of a CHSH-type Bell inequality with the storage time $\delta t_s = 500$ ns. Error bars represent statistical errors, which are ± 1 standard deviation.	93
10.5	Visibility as a function of the storage time with 6 m fiber connection. Black dots are for the visibility and the dashed line shows the threshold for the violation of the CHSH-type Bell inequality. Error bars represent statistical errors, which are ± 1 standard deviation.	94
10.6	Experimental outcomes of the fractions at different polarization settings with 300 m fiber connection. The polarization bases are chosen as (a) $ +\rangle$ and $ -\rangle$, (b) $ H\rangle$ and $ V\rangle$, and (c) $ \odot\rangle$ and $ \ominus\rangle$ respectively.	95
10.7	Phase stabilization method. The prism P1 is mounted on a piezo and the phase difference between the two arms L and R can be controlled by driving this piezo.	96

11.1	A schematic of the experiment. (a) The atoms are confined in an optical trap formed by a red-detuned, focused beam. The optical-trapping beam is overlapped with write and read beams, counter-propagating to each other, on the dichroic mirror (DM) and is blocked by a beam dump (BD) on the other side of the atoms. Single-photon detectors, D1 and D2, are placed at an angle of 3° with respect to the optical trap to detect the Stokes and anti-Stokes fields, respectively. (b) An absorption image of optically trapped atoms.	101
11.2	Time sequence of one experimental cycle and the relevant atomic transitions in the experiment. (a) After the MOT is switched off, the atoms are loaded into an optical trap with a transfer efficiency of $\sim 5\%$. Typically, 10000 write and read pulses are employed during a single experimental cycle, with a pulse length of 100 ns and 500 ns respectively. (b) The left and right diagrams illustrate the atomic levels involved in the write and read processes, where $ g\rangle = 5S_{1/2}, F = 1\rangle$, $ s\rangle = 5S_{1/2}, F = 1\rangle$, and $ e\rangle = 5P_{3/2}, F = 2\rangle$. The relevant Zeeman states are the $ F, m_F\rangle = 1, -1\rangle, 2, 1\rangle$ (clock states) and $ F, m_F\rangle = 1, 0\rangle, 2, 2\rangle$ (non-clock states).	102
11.3	Normalized cross-correlation function $g_{1,2}$ of the Stokes and anti-Stokes fields as a function of storage times. (a) Non-classical correlation is observed for storage times up to $70 \mu\text{s}$. The curve is a Gaussian fit with a $1/e$ lifetime of $65 \mu\text{s}$. (b) With an improved compensation of the earth magnetic field, two different time scales of the decay have been observed. The fast decay with $\tau_f = 10 \mu\text{s}$ corresponds to the atoms in the non-clock states and the subsequent slow decay is due to the atoms in the clock states. The dashed and solid curves are the Gaussian fits with one and two time constants, respectively. The error bars represent the statistical error. The dotted line illustrates the classical limit, $g_{1,2} = 2$	104
12.1	(A) Schematic view of the experiment. A weak σ^- polarized write pulse is applied to generate the SW and Stokes photon via spontaneous Raman transition. The Stokes photon are detected at an angle of θ relative to the write beam. After a controllable delay, a strong σ^+ polarized read light converts the SW into an anti-Stokes photon. (B) The structure of atomic transitions (^{87}Rb) under a weak magnetic field. The left panel corresponds to the experiment with $(1, 0\rangle, 2, 0\rangle)$. The right one corresponds to the experiment with $(1, 1\rangle, 2, -1\rangle)$. (C) Illustration of the SW dephasing induced by atomic random motion. The blue curve represents the SW initially stored in the quantum memory. The perturbed SW is represented by the red curve. (D) The wavelength of the SW can be controlled by changing the detection configuration.	109
12.2	The cross correlation $g_{\text{S,AS}}$ versus the storage time δt for $(1, 0\rangle, 2, 0\rangle)$ at $\theta = 3^\circ$. The data are fitted by using $g_{\text{S,AS}}(\delta t) = 1 + C \exp(-\delta t^2/\tau_{\text{D}}^2)$. Our data give a lifetime of $\tau_{\text{D}} = 25 \pm 1 \mu\text{s}$, which is much less than the theoretical estimation for the ‘‘clock state’’. Error bars represent statistical errors.	110
12.3	The cross correlation $g_{\text{S,AS}}$ versus the storage time δt for different angles (A)-(C) and the measured lifetime τ_{D} as a function of detection angle θ (D). Panels (A) and (B) are for $(1, 0\rangle, 2, 0\rangle)$ at $\theta = 1.5^\circ$ and 0.6° , respectively. The data are fitted by using $g_{\text{S,AS}}(\delta t) = 1 + C \exp(-\delta t^2/\tau_{\text{D}}^2)$, where τ_{D} is the lifetime due to dephasing. Panel (C) is for $(1, 1\rangle, 2, -1\rangle)$ at $\theta = 0.2^\circ$. In this case we take into account the effect of loss of atoms and fit the data by using $g_{\text{S,AS}}(\delta t) = 1 + C \exp(-\delta t^2/\tau_{\text{D}}^2)/(1 + A\delta t^2)$, with A the fitting parameter obtained from the collinear configuration. The fitted lifetime for each case is: (A) $\tau_{\text{D}} = 61 \pm 2 \mu\text{s}$, (B) $\tau_{\text{D}} = 144 \pm 9 \mu\text{s}$, (C) $\tau_{\text{D}} = 283 \pm 18 \mu\text{s}$. The first data are a little bit higher than the fitted curves, which might be caused by the imperfection in the pumping process. By reducing the angle, the lifetime is increased from $25 \mu\text{s}$ to $283 \mu\text{s}$, which implies the decoherence is mainly caused by the dephasing induced by atomic random motion. Panels (D) depicts the measured lifetime τ_{D} as a function of detection angle θ , where the horizontal error bars indicate measurement errors in the angles. The solid line is the theoretical curve with $T \simeq 100 \mu\text{K}$. The experimental results are in good agreement with the theoretical predications. The vertical error bars indicate statistical errors.	112

-
- 12.4 The cross correlation $g_{S,AS}$ versus the storage time δt for $\theta = 0^\circ$ and $(|1, 1\rangle, |2, -1\rangle)$. The data are fitted by using $g_{S,AS}(\delta t) = 1 + \frac{C}{1+A\delta t^2}$, with A the fitting parameter. Our data give a lifetime of $\tau_L = 1.0 \pm 0.1$ ms, when the retrieval efficiency $\gamma(\delta t) = \frac{1}{1+A\delta t^2}$ has dropped to $1/e$. Error bars represent statistical errors. 113

List of Tables

7.1	Correlation functions E and the resulting S	67
8.1	Fidelities of teleporting a photonic qubit at a storage time of $0.5 \mu s$. Data for teleporting each state are collected two hours. The error bars represent the statistical error, i.e., ± 1 standard deviation.	75

Chapter 1

Introduction

Quantum information processing is a new interdisciplinary research field with the potential to cause revolutionary advances in the fields of computation and communication by exploiting the information theory and the physical law of quantum mechanics.

The fundamental unit of quantum information is a qubit, which is the counterpart of a classical bit in classical computing. Any two-level quantum mechanical system can serve as a qubit, e.g., the electronic spin or the polarization state of light. The most distinguishing feature between a qubit and a classical bit is that the qubit can be in a linear superposition of all the classically allowed states, according to the superposition principle of quantum mechanics. The superposition of two or more qubits exhibits quantum entanglement, which is a nonclassical phenomenon and has no counterpart in classical computing. Quantum entanglement is one of the most important resources of quantum information processing. By exploiting quantum entanglement, one can teleport an arbitrary quantum state from one point to another distant point [1, 2], or establish entanglement between two remote qubits that never interact with each other [3, 4].

Quantum information processing mainly contains two subfields, quantum computation and quantum communication. Quantum computation holds the promise to solve certain difficult problems that can't be efficiently solved by classical computers [5]. Quantum communication has the potential to achieve secure long-distance communication which cannot be intercepted by any eavesdropper [6].

1.1 Quantum computation

The concept of quantum computation was originally put forward by R.P. Feynman, who found that a computer running according to the physical law of quantum mechanics could solve problems much faster than a classical one due to quantum parallelism. Later in 1985, D. Deutsch showed that any physical process could in principle be modelled by a quantum computer, and the universal quantum computation can be implemented by a series of single-qubit rotation gates and two-qubit controlled-not gates [7]. The year of 1994 witnessed the breakthrough in quantum computation. In this year, P. Shor proposed a quantum algorithm to solve an important problem in the number theory, namely factorization, by using quantum computer [8]. Shor's algorithm makes the task of factor-

ing large prime numbers exponentially faster than using conventional computers [9]. Two years later, Grover proposed a search algorithm for finding a certain number over unsorted database [10]. Grover's search algorithm scales with the square root of the database's size, where classically the task scales linearly. Shor's factorization algorithm and Grover's search algorithm, together with Deutsch's algorithm are all the quantum algorithms known up to now.

Motivated by the development in quantum computing theory, physicists are trying to find the quantum systems suitable for the task of quantum computation. Nuclear magnetic resonance (NMR) system is the first physical system used to demonstrate the ideas of quantum computation. Shor's factorization algorithm to factor 15 was realized by using a 7-qubit NMR quantum computer [11]. However, current NMR implementations are not scalable and thus is not a real quantum computation[12].

In 1995, I. Cirac and P. Zoller proposed to implement a scalable quantum computation by manipulating a string of trapped ions whose electronic states represent the qubits [13]. In recent years, remarkable progress has been accomplished towards the ion-trap quantum computation. The controlled-not gate between two ions in a linear Paul trap was realized, quantum teleportation between atoms at a distance of a few micron was demonstrated [14, 15], and even 8-qubit entangled state has been generated [16, 17]. The scalable quantum computation can also be implemented by using only linear optics and single photon sources, as suggested by E. Knill, R. Laflamme and G. Milburn [18]. In contrast to the ion-trap systems, there is no interaction between photonic qubits and the nonlinearity is induced by the indistinguishability between the photons and single photon detection [19, 20, 21]. The KLM scheme can also be implemented by using guided atoms [22, 23]. Most recently, five and six photonic entangled states have been prepared and used to demonstrate open-destination teleportation [24] and teleportation of a composite system [25], respectively. In 2001, a new concept of quantum computation, i.e., "one way quantum computing" is proposed by H.-J. Briegel and R. Raussendorf [26]. Different from the conventional circuit computation where the entanglement is introduced in the computation process, a complex entangled state, i.e., graph state, is prepared at the beginning of one way computing. Once the graph state is prepared, quantum computation can be implemented simply by performing single qubit measurement. The 4-qubit [27] and 6-qubit [28] graph states have been created by using linear optics, and the simplest one-way Grover's search algorithm [27, 29] and Deutsch's algorithm [30] has been demonstrated.

1.2 Quantum communication

1.2.1 Quantum cryptography

The beautiful idea of quantum cryptography was proposed by C. Bennett and G. Brassard (BB84), who suggested to implement secure long-distance quantum communication by using only single photon sources, single photon detectors and random number generators [31]. The BB84 protocol can be described as follows. Assume Alice and Bob are the two communication users, and Eve is the eavesdropper. In the first step, Alice randomly selects the polarization states of a sequence of single photons and sends them to Bob's side, where

the photons are detected by single photon detectors via randomly choosing the detection bases. In the second step, they compare the sending bases and detection bases used in the first step through classical communication. Once the bases are the same, the results are kept for the security key, otherwise the results are discarded. If Eve is intercepting the communication channel, due to the non-cloning theorem, she has to detect a photon and resend another one to Bob, which will introduce errors in Bob's measurement results. Therefore, Alice and Bob can check the presence of Eve by comparing a part of their security key. In contrast to classical cryptography, where the security is based on the complexity of factoring a large prime number, the security of quantum cryptography is based on the physical principle of quantum mechanics and thus is completely secure [6].

The first demonstration of quantum cryptography was performed over a distance of 30 cm in the IBM laboratory. Since then, tremendous progress has been made, and quantum communication outside laboratory has been realized. However, in practice, the BB84 protocol suffers from several serious technical problems, i.e., the lack of perfect single photon sources, the dark counts of single photon detectors and the low transmission rate of communication channel [6]. Even with the improved protocol, e.g., decoy state protocol, the upper limit of secure quantum key distribution is only about a few hundred kilometers [32, 33]. The experimental record of 144 km was achieved by implementing quantum key distribution over two islands in the sea [34].

The serious problems in BB84 protocol might be bypassed by the entanglement based protocol proposed by A. Ekert (Ekert91) [35]. In Ekert91 protocol, Alice and Bob share many maximally entangled states. When implementing quantum key distribution, they just measure the qubits at their hands by randomly choosing the detection basis. As in the BB84 protocol, they only keep the results where the detection bases are the same. It can be demonstrated that as long as the entangled pair shared between them can violate the Bell inequality, the quantum cryptography is secure [6].

1.2.2 Quantum repeater

To implementing quantum cryptography by Ekert91, one has to establish entanglement between two distant communication sites. Directly transferring one photon of a locally entangled pair to the other remote location is impossible due to the exponential transmission loss. In 1998, H.-J. Briegel *et al.* proposed a quantum repeater protocol to establish entanglement between two remote sites by combing entanglement swapping, entanglement purification and quantum memory [36, 37]. The principle of a quantum repeater is illustrated in Fig. 1.1. Assume the communication distance is divided into many segments and we have created entanglement between neighboring sites. The entanglement between the nearest sites can be connected to extend the communication length by entanglement swapping. In practice, entanglement swapping is not perfect and the fidelity of the entanglement will decrease significantly after a few connection steps. Therefore, entanglement purification [38, 39] has to be implemented to improve the quality of the entangled pairs generated during connection. As shown in Fig. 1.1, a nesting purification scheme is implemented by iterating entanglement swapping and entanglement purification until finally a remote entangled pair with high fidelity is established between the two distant communi-

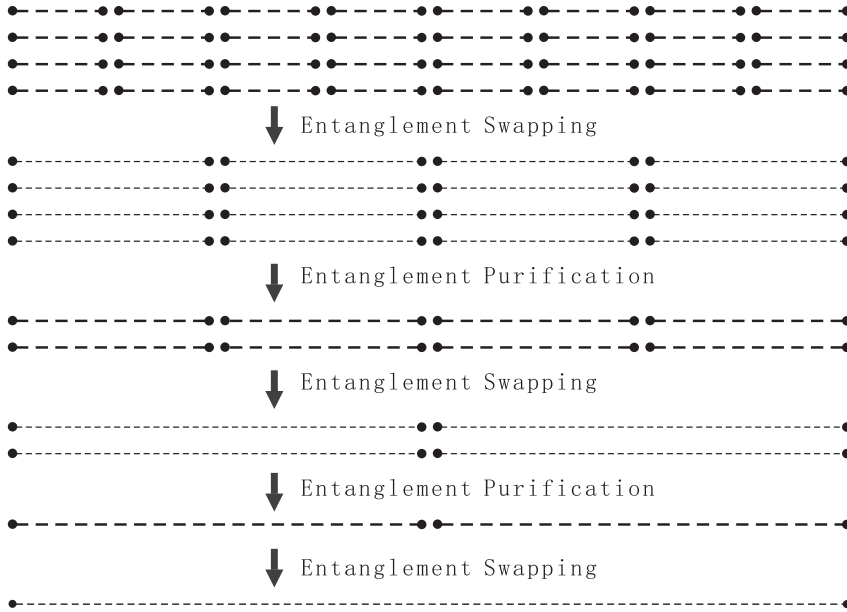


Figure 1.1: An illustration of the quantum repeater protocol. The communication distance is extended by entanglement swapping, and the fidelity of the entangled pair is improved by entanglement purification.

cation sites. It was demonstrated that the time overhead and the sources needed to create the remote entangled pair scales polynomially with the distance.

Early physical implementations of a quantum repeater were based on atoms trapped in high-finesse cavities, where strong coupling between atoms and photons is required [40, 41]. In a seminal paper, Duan-Lukin-Cirac-Zoller (DLCZ) proposed an implementation of the quantum repeater by using atomic ensembles and linear optics [42]. In this protocol atomic ensembles are used as memory qubits to avoid the challenging request for strong coupling between atoms and photons. Besides, the DLCZ protocol has built-in entanglement purification and thus is photon-loss tolerant. In the efforts of realizing the atomic-ensemble-based quantum repeater protocol, significant experimental advances have been achieved. Non-classical correlated photons were generated in atomic ensembles [43, 44], controllable single photon sources were realized by using feed back circuit [45, 46], and entanglement between two atomic ensembles at a distance of 3 meter is constructed [47]. The DLCZ protocol is attractive since it uses relatively simple ingredients. However, it also has several inherent drawbacks which are severe enough to make long-distance quantum communication impossible [48, 49].

1.3 The objective of this work.

This thesis covers our recent theoretical and experimental work towards realistic long-distance quantum communication with atomic ensembles and linear optics. Part of this work was published in joint theoretical and experimental articles. Note that when describ-

ing the experimental details, the pronoun “we” refers to the individuals who performed the experiments, and not the author of this thesis. The remainder of this thesis is organized as follows.

- In chapter 2, we review the theory of atomic-ensemble-based quantum memory. A detailed analysis is presented to describe the write and read process. The nonclassical correlation between the photons generated from atomic ensembles is also discussed.
- In chapter 3, we review the DLCZ protocol and give a detailed analysis on its drawbacks. It will be shown that the phase stabilization requirement is an experimental forbidden task for current technology. The low scalability is also a serious problem for long-distance quantum communication.
- In chapter 4, we propose a new architecture of quantum repeater protocol based on two-photon interference and two-photon detection, which relax the long-distance stability requirements by about 7 orders of magnitude.
- In chapter 5, we improve the new protocol by means of local generation of high-quality entanglement. The improved protocol is much faster than any other protocols with similar ingredients.
- In chapter 6, we propose and demonstrate a deterministic single photon source based on atomic ensembles by the aid of feedback circuit.
- In chapter 7, we report the synchronized generation of two indistinguishable photons from independent atomic ensembles. The Hong-Ou-Mandel dip is observed in both time domain and frequency domain.
- In chapter 8, we demonstrate the quantum teleportation between a photonic qubit (flying qubit) and a memory qubit (stationary qubit). The teleportation fidelity is still beyond the classical threshold after a storage time of 8 μ s.
- In chapter 9, we propose and demonstrate a novel way to efficiently create a stable entanglement between a memory qubit and a photonic qubit. The new approach can be generalized to generate higher dimensional entanglement.
- In chapter 10, we report the realization of entanglement swapping between photonic and atomic qubits, which is a building block of the robust and efficient quantum repeater. Entanglement between two sites at a distance of 300 meter is generated.
- In chapter 11, we report the observation of non-classical photon pair generated from a quantum memory trapped in optical dipole trap. The cross-correlation function of the photon pair was found to violate the Cauchy-Schwarz inequality for storage times up to 70 μ s.
- In chapter 12, we demonstrate a long-lived quantum memory for scalable quantum networks. By exploiting “clock state” and generating a long wavelength spin wave, we succeed in extending the storage time of the quantum memory to 1 ms.

We conclude this thesis in chapter 13, by summarizing the main results and providing an outlook to future work.

Chapter 2

Atomic memory for a quantum repeater

In this chapter, we review the theory of atomic-ensemble-based quantum memory. A detailed description of the write and retrieve process is presented, where the decoherence mechanisms and the effects on the lifetime of the quantum memory are also discussed. The nonclassical correlation between photons generated from the atomic ensemble is characterized by a violation of the Cauchy-Schwarz inequality.

2.1 Introduction

In the atomic-ensemble-based quantum repeater protocols, a quantum state is imprinted in a collective state of an atomic ensemble when a Stokes photon is generated in the write process. The atomic collective excitation can be retrieved out and converted back to an anti-Stokes photon in the electromagnetically induced transparency (EIT) based retrieval process. The nonclassical correlation between the photons generated from the atomic ensemble is essential for the quantum repeater protocols [42].

We consider the Λ -type three-level atomic systems. The energy level structure is depicted in Fig. 2.1, where the upper state $|e\rangle$ is the excited state, and two lower states $|g\rangle$, $|s\rangle$ are the two ground states used to store the quantum state. At the beginning, all atoms are prepared in the ground state $|g\rangle$ by optical pumping.

In the write process, an off-resonant weak classical laser pulse coupling the ground state $|g\rangle$ and the excited state $|e\rangle$ is applied to the atomic ensemble. A small quantity of the atoms will be excited and transferred to the other ground state $|s\rangle$, and at the same time Stokes photons are generated due to spontaneous Raman scattering. According to the energy conservation, the number of the atoms transferred to the $|s\rangle$ state is equal to the number of Stokes photons emitted from the atomic ensemble. Assume the write pulse is so weak that only one Stokes photon is generated. In this case, there is only one atom changes to the $|s\rangle$ state, but it is impossible to know which atom it is, even in principle. Therefore, after the Stokes photon is detected, the atomic ensemble is projected into an equally weighted superposition state $|\psi\rangle = \frac{1}{\sqrt{N}} \sum_i |g\rangle_1 \dots |s\rangle_i \dots |g\rangle_N$, which is a collective

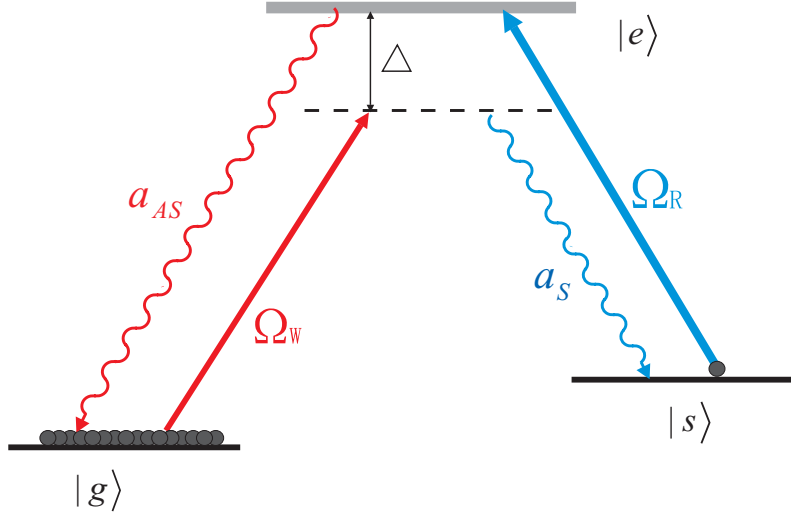


Figure 2.1: An illustration of the interaction between atomic ensemble and light. The excited state $|e\rangle$, and two ground states $|g\rangle$ and $|s\rangle$ form the Λ -type three-level atom. In the write process, an off resonant write light pulse with Rabi frequency Ω_w and detune Δ is applied to the atomic ensemble. A Stokes photon is emitted and simultaneously a collective excitation is generated due to spontaneous Raman scattering. In the EIT-based read process, an on resonance read light pulse with Rabi frequency Ω_R is applied to convert the collective excitation to an anti-Stokes photon.

excited state. That is to say, in the write process a quantum state is imprinted into the collective excited state of the atomic ensemble conditional on detecting a Stokes photon. Since the two ground states $|s\rangle$ and $|g\rangle$ are immune to spontaneous emission and the collective state is robust against single-atom or multi-atom decoherence processes, the collective excitation can be stored in the atomic ensemble for a long time [50].

After a while when we need the quantum state for further application, we can shine in an on resonance strong classical read light pulse, which will couple the excited state $|e\rangle$ and the ground state $|s\rangle$, to convert the excitation in the atomic ensemble into an anti-Stokes photon. The read process is usually described by an EIT-based process [50, 51], and in ideal case the excitation stored in the atomic ensemble can be fully retrieved out. The Stokes photon and anti-Stokes photon are nonclassically correlated, which leads to a violation of the Cauchy-Schwarz inequality.

In the following we will present a detailed description of the write and read process. We describe the spontaneous Raman scattering by using perturbation theory. The read process is discussed by treating the atoms as classical point light sources. In both cases, a diffraction mode is presented to determine the spatial modes. The dark-state-polariton theory is also used to describe the retrieve process.

2.2 Spontaneous Raman scattering

Let us consider a pencil-shaped cold atomic ensemble containing N atoms trapped in magnetic-optical trap or optical dipole trap. We denote the axial direction as z direction

and assume the zero point is at the center of the atomic ensemble. At the beginning, all the atoms are in the ground state $|g\rangle$. The off-resonant classical write pulse coupling the excited state $|e\rangle$ and the ground state $|g\rangle$ is given by $\mathbf{E}_W(\mathbf{r}, t) = \hat{\mathbf{e}}_W E_W(\mathbf{r}, t)e^{i\mathbf{k}_W \cdot \mathbf{r} - i\omega_W t} + \text{H.c.}$, where $\hat{\mathbf{e}}_W$ is the polarization unit vector, $\omega_W = ck_W$ is the frequency of the write light. For simplicity, we assume the write light pulse propagating along the axial direction $\mathbf{k}_W = k_W \hat{z}$. The Stokes field coupling the excited state and ground state $|s\rangle$ is quantum mechanically described as $\mathbf{E}_S(\mathbf{r}, t) = \sum_{\mathbf{k}} \hat{\mathbf{e}}_{\mathbf{k}} \varepsilon_{\mathbf{k}} a_{\mathbf{k}} e^{i\mathbf{k} \cdot \mathbf{r} - i\omega_{\mathbf{k}} t} + \text{H.c.}$, where $\varepsilon_{\mathbf{k}} = \sqrt{\frac{\hbar\omega_{\mathbf{k}}}{2\epsilon_0 V}}$, $\omega_{\mathbf{k}} = ck$, $\hat{\mathbf{e}}_{\mathbf{k}}$ is the polarization unit vector, and $a_{\mathbf{k}}$ is the annihilation operator of mode \mathbf{k} . In the cold atomic ensemble, because of the extremely low temperature and the short pulse length of the write light, we can safely assume the atoms are fixed at certain positions during the write process and denote the coordinate of the i th atom by \mathbf{r}_i . The total Hamiltonian in the rotating frame is given by

$$H = \sum_i^N \{ \hbar \Delta \sigma_{ee}^i + [-\hbar \Omega_W(\mathbf{r}_i, t) e^{i\mathbf{k}_W \cdot \mathbf{r}_i} \sigma_{eg}^i + \sum_{\mathbf{k}} \hbar g_{\mathbf{k}} a_{\mathbf{k}} e^{i\mathbf{k} \cdot \mathbf{r}_i - i\Delta\omega_{\mathbf{k}} t} \sigma_{es}^i + \text{H.c.}] \}, \quad (2.1)$$

where the detuning $\Delta = \omega_{eg} - \omega_W$ and $\Delta\omega_{\mathbf{k}} = \omega_{\mathbf{k}} - \omega_W - \omega_{sg}$, with $\omega_{eg} = \omega_e - \omega_g$ and $\omega_{sg} = \omega_s - \omega_g$ the difference between atomic levels. The spin operators $\sigma_{lm}^i = |l\rangle_i \langle m|$ ($l, m = e, g, s$) are the transition operators of i th atom, $\Omega_W(\mathbf{r}, t) = \frac{\mathbf{d}_{eg} \cdot \hat{\mathbf{e}}_W E_W(\mathbf{r}, t)}{\hbar}$ is the Rabi frequency of the write light, and $g_{\mathbf{k}} = -\frac{\mathbf{d}_{es} \cdot \hat{\mathbf{e}}_{\mathbf{k}} \varepsilon_{\mathbf{k}}}{\hbar}$ is the coupling coefficient of each mode of the Stokes light.

If the Rabi frequency of the write light and the linewidth of the excited state are both significantly smaller than the detuning Δ , the upper state $|e\rangle$ can be adiabatically eliminated, and each atom is described by a two-level model. The resulting adiabatic Hamiltonian is given by [52]

$$H = \sum_i^N \left[\sigma_{sg}^i \frac{\Omega_W(\mathbf{r}_i, t) e^{i\mathbf{k}_W \cdot \mathbf{r}_i}}{\Delta} \sum_{\mathbf{k}} \hbar g_{\mathbf{k}} a_{\mathbf{k}}^\dagger e^{-(i\mathbf{k} \cdot \mathbf{r}_i - i\Delta\omega_{\mathbf{k}} t)} + \text{H.c.} \right], \quad (2.2)$$

where for simplicity we have neglected the small AC Stark shift. This adiabatic Hamiltonian describes the spontaneous emission of N atoms from the pseudo excited state $|g\rangle$ to the pseudo ground state $|s\rangle$, where the frequency of the emitted Stokes light is centered at $\omega_S = \omega_W - \omega_{sg}$. The the linewidth of the pseudo excited state is $\Gamma' = \frac{\Omega_W^2}{\Delta^2} \Gamma$, with Γ the decay rate from $|e\rangle$ to $|s\rangle$. This Hamiltonian has been extensively investigated in last two decades [53, 54, 55]. The initial stage can be well described by spontaneous emission where the Stokes photon is emitted along all the directions. After a time of $1/\Gamma'$, the Stokes light will dominate along the axial direction and enter the superradiance regime. In our case, the interaction time T is determined by the pulse duration of the write beam which is short compared to the lifetime $1/\Gamma'$, and thus we are in the spontaneous emission regime. Therefore we can simply solve the Schrödinger equation by using perturbation theory. To the first order of the perturbation, the atom-light system is described by

$$|\psi\rangle = \left[1 - i \int_0^T H(\tau) d\tau \right] |vac\rangle + o(p) \quad (2.3)$$

with $|vac\rangle = |0\rangle_a|0\rangle_p$, where $|0\rangle_a = \otimes_i |g\rangle_i$ denotes the atomic vacuum state and $|0\rangle_p$ is the light vacuum. Integrating out τ , we obtain

$$|\psi\rangle = |0\rangle_a|0\rangle_p + \sum_i^N \frac{\Omega_W(\mathbf{r}_i)e^{i\mathbf{k}_W \cdot \mathbf{r}_i}}{\Delta} |g\dots s_i\dots g\rangle |\gamma\rangle_i, \quad (2.4)$$

where $|\gamma\rangle_i = -i \int_0^T \sum_{\mathbf{k}} g_{\mathbf{k}} a_{\mathbf{k}}^\dagger e^{-i(\mathbf{k} \cdot \mathbf{r}_i - \Delta\omega_{\mathbf{k}}t)} |0\rangle_p$ is the spontaneous emitted Stokes light for the i th atom, and we have assumed the Rabi frequency is time independent. It can be easily seen that in the spontaneous emission regime the atoms emit Stokes photons into all the directions independently from each other.

As is discussed in standard quantum optics books [56, 57], the spatial wave function of the photon emitted from i th atom can be described by $E_i(\Delta r_i) = \frac{\varepsilon_0}{\Delta r_i} e^{ik_S \Delta r_i}$, where $k_S = \omega_S/c$, ε_0 is the constant proportional to the electro-dipole transition matrix element, $\Delta r = |\mathbf{r} - \mathbf{r}_i|$ is the distance between the i th atom and observation point \mathbf{r} . Assume we observe the Stokes light along the axial direction as depicted in Fig. 2.2. Then under the paraxial axial approximation $|z - z_i|^2 \gg x^2, y^2, x_i^2, y_i^2$, the wave function on the observation surface is expressed as

$$E_i(\mathbf{r}) = \frac{\varepsilon_0}{z - z_i} \exp\left[ik_S \left(z - z_i + \frac{x_i^2 + y_i^2}{2(z - z_i)} + \frac{x^2 + y^2}{2(z - z_i)}\right) - ik_S \frac{x_i x + y_i y}{z - z_i}\right] \quad (2.5)$$

$$\begin{aligned} &\simeq \frac{\varepsilon_0}{z} \exp(-ik_S z_i) \exp\left[ik_S \left(z + \frac{x_i^2 + y_i^2}{2z} + \frac{x^2 + y^2}{2z} - \frac{x_i x + y_i y}{z}\right)\right] \\ &\times \exp\left[ik_S \left(\frac{x_i^2 + y_i^2}{2z^2} z_i + \frac{x^2 + y^2}{2z^2} z_i - \frac{x_i x + y_i y}{z^2} z_i\right)\right], \end{aligned} \quad (2.6)$$

where $|z_i| \ll z$ is assumed. We define two diffraction angles $\theta_{w_a} = \frac{1}{k_S w_a}$ and $\theta_L = \left(\frac{1}{k_S L}\right)^{\frac{1}{2}}$, where w_a and L are the waist and length of the atomic ensemble, respectively. It can be readily seen that if the detection angle $\theta \leq \min(\theta_{w_a}, \theta_L)$, all the phase factors in Eq. (2.6) related to coordinates of the atoms, except $\exp(-ik_S z_i)$, can be safely neglected. Thus the Stokes light on the observation surface can be regarded as one mode, and the spatial wave function is described by

$$E_i(\mathbf{r}) \simeq \frac{\varepsilon_0}{z} \exp\left[ik_S \left(z + \frac{x^2 + y^2}{2z}\right)\right] \exp(-ik_S z_i) \quad (2.7)$$

$$= \zeta_S(\mathbf{r}) \exp(-i\mathbf{k}_S \cdot \mathbf{r}_i) \quad (2.8)$$

with $\zeta_S(\mathbf{r}) = \frac{\varepsilon_0}{z} \exp\left[ik_S \left(z + \frac{x^2 + y^2}{2z}\right)\right]$ and $\mathbf{k}_S = k_S \hat{z}$ the wave vector of the detected Stokes light. We approximate the detected Stokes photon state by $|\gamma\rangle_i = \sqrt{p} a_S^\dagger \exp^{-i\mathbf{k}_S \cdot \mathbf{r}_i} |0\rangle_p$, where a_S^\dagger is a single mode creation operator, and $p = \Gamma T \frac{\Omega_W^2}{\Delta^2} d\Omega \ll 1$ is the small probability for one atom to scatter one Stokes photon into the detection solid angle $d\Omega$. Substituting $|\gamma\rangle_i$ into Eq. (2.4), we obtain

$$|\psi\rangle = [1 + \sqrt{p} \left(\sum_i^N e^{i\Delta\mathbf{k} \cdot \mathbf{r}_i} \sigma_{sg}^i a_S^\dagger\right)] |vac\rangle, \quad (2.9)$$

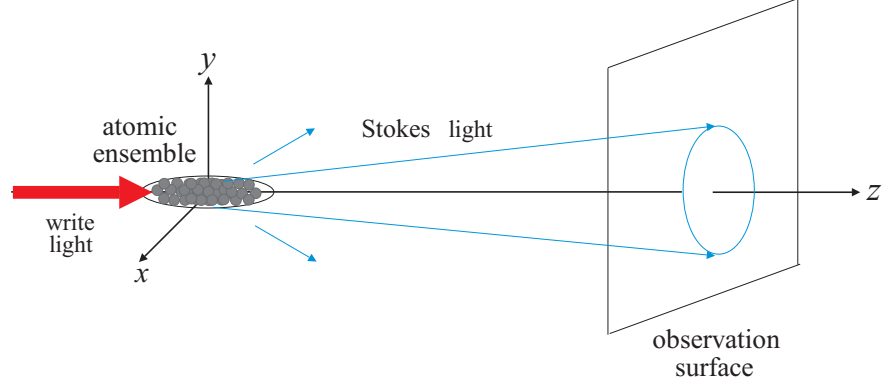


Figure 2.2: A schematic view of the write process. The Stokes light is emitted along all the directions in the spontaneous Raman scattering process. The Stokes light in the blue cone can be treated as one mode if we detect the scattered light along the axial direction.

where $\Delta\mathbf{k} = \mathbf{k}_w - \mathbf{k}_s$ is the momentum difference between the write light and the detected Stokes mode, and we have assumed the Rabi frequency Ω_w is a constant in the atomic ensemble. Defining a bosonic collective state operator

$$S^\dagger = \frac{1}{\sqrt{N}} \sum_i^N e^{i\Delta\mathbf{k}\cdot\mathbf{r}_i} \sigma_{sg}^i, \quad (2.10)$$

we have $[S, S^\dagger] \simeq 1$. The atom-light system is described by

$$|\psi\rangle = [1 + \sqrt{\chi} S^\dagger a_s^\dagger] |vac\rangle \quad (2.11)$$

with $\chi = Np$ the probability to detect one Stokes photon in write process. It is easily to see when a Stokes photon is detected, the atomic ensemble is projected into the collective excited state, or in other words a spin wave is imprinted into the atomic ensemble.

The conventional single mode condition that the Fresnel number $F = \frac{A}{\lambda L} \simeq 1$ [53] with the cross section area $A = \pi w_a^2$, can be obtained by assuming the two diffraction angles are equal $\theta_{w_a} \simeq \theta_L$. In this case, the detection solid angle can be approximated by λ^2/A . Then we have the total excitation probability $\chi = N\Gamma T \frac{\Omega_w^2}{\Delta^2} \frac{\lambda^2}{A} \sim d_0 \gamma_s T$, where $d_0 \sim N\sigma_0/A$ with $\sigma_0 = \frac{\lambda^2}{2\pi}$ and $\gamma_s \sim \Gamma \frac{\Omega_w^2}{\Delta^2}$, which is consistent with the results in Ref. [51]. To ensure we are in the spontaneous Raman scattering regime, we require the excitation probability $\chi \ll 1$.

Note that in write process, there is no constructive interference in the forward direction, because when one atom scattering a Stokes photon, it changes to another ground state $|s\rangle$ and thus all the N terms in Eq. (2.9) are orthogonal to each other. The detection solid angle is determined by the shape (the waist and the length) of the atomic ensemble. In principle, one can detect the Stokes photon along any direction.

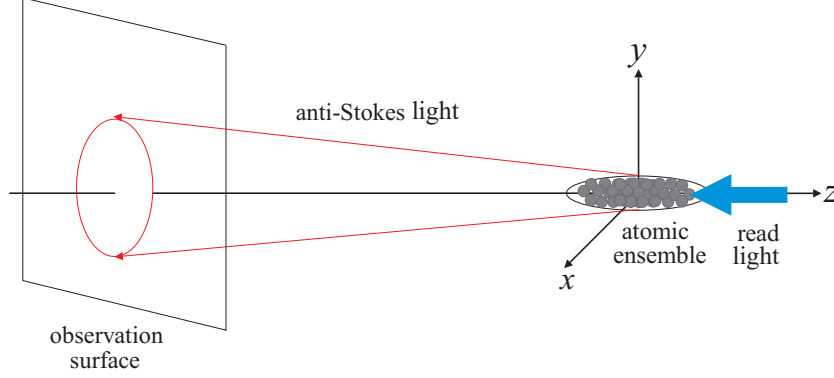


Figure 2.3: A schematic view of the read process. The anti-Stokes light is emitted along the backward direction where the mode match condition is satisfied. Constructive interference occurs in the red cone.

2.3 Retrieval of the stored collective excitation

In read process, a strong classical read light is applied to the atomic ensemble to convert the collective excitation into an anti-Stokes photon. The weak anti-Stokes field and the strong read light satisfy the EIT condition [58], and thus the anti-Stokes field is not absorbed by the atoms in ground state $|g\rangle$.

Assume the strong classical read light coupling the excited state $|e\rangle$ and ground state $|s\rangle$ is counter-propagating with the write light $\mathbf{k}_R = -k_R \hat{z}$. The atom in state $|s\rangle$ is excited by the read light and transferred back to ground state $|g\rangle$, generating an anti-Stokes photon simultaneously. In contrast to the write process, the light emitted from different atoms will interfere with each other, and constructive interference will occur in the direction where mode match condition is satisfied. The read process can be described by

$$\frac{1}{\sqrt{N}} \sum_i^N e^{i\Delta\mathbf{k}\cdot\mathbf{r}_i} |g\dots s_i\dots g\rangle \Rightarrow \otimes_i |g\rangle_i E(\mathbf{r}'). \quad (2.12)$$

The spatial wave function of the anti-Stokes field on the observation point \mathbf{r}' can be expressed as

$$E(\mathbf{r}') = \frac{1}{\sqrt{N}} \sum_i^N e^{i\Delta\mathbf{k}\cdot\mathbf{r}_i} e^{i\mathbf{k}_R\cdot\mathbf{r}_i} \frac{\varepsilon_0}{\Delta r'_i} e^{ik_{AS}\Delta r'_i} \quad (2.13)$$

with $\Delta r'_i = |\mathbf{r}' - \mathbf{r}_i|$, where the atoms are treated as point light sources. Assume we observe anti-Stokes light along the backward direction (see Fig. 2.3). Under the paraxial approximation, we can write the anti-Stokes light as,

$$E(\mathbf{r}') = \sum_i^N \left(e^{i(\Delta\mathbf{k}+\mathbf{k}_R)\cdot\mathbf{r}_i} e^{-i\mathbf{k}_{AS}\cdot\mathbf{r}_i} \frac{\varepsilon_0}{|z' - z_i|} \times \exp\left[ik_{AS} \left(|z'| + \frac{x_i^2 + y_i^2}{2|z' - z_i|} + \frac{x'^2 + y'^2}{2|z' - z_i|} \right) - ik_{AS} \frac{x_i x' + y_i y'}{|z' - z_i|} \right] \right). \quad (2.14)$$

It can be readily seen that the once the mode match condition $\mathbf{k}_W - \mathbf{k}_S + \mathbf{k}_R - \mathbf{k}_{AS} = 0$

is satisfied, constructive interference will be observed on the detection surface. The anti-Stokes field can be described by

$$\begin{aligned} E(\mathbf{r}') &= \frac{1}{\sqrt{N}} \sum_i^N \frac{\varepsilon_0}{|z' - z_i|} \exp[ik_{AS}(|z'| + \frac{x_i^2 + y_i^2}{2|z' - z_i|} + \frac{x'^2 + y'^2}{2|z' - z_i|}) - ik_{AS} \frac{x_i x' + y_i y'}{|z - z_i|}] \\ &\simeq \sqrt{N} \int d\mathbf{r}'' n(\mathbf{r}'') \frac{\varepsilon_0}{z'} \exp[-ik_{AS}(z' + \frac{x'^2 + y'^2}{2z'})] = \sqrt{N} \zeta_{AS}(\mathbf{r}'), \end{aligned} \quad (2.15)$$

where $\zeta_{AS}(\mathbf{r}') = \frac{\varepsilon_0}{z'} \exp[-ik_{AS}(z' + \frac{x'^2 + y'^2}{2z'})]$, $n(\mathbf{r})$ is the density distribution, and we have assumed the detection angle $\theta' \leq \min(\theta_{w_a}, \theta_L)$. In general, the spatial mode function can be calculated by numerically integrating Eq. (2.15). One can also see that the intensity of the anti-Stokes light is proportional to the atomic number N and the detection solid angle. The retrieval efficiency can be estimated by

$$\eta_{ret} \sim \frac{\gamma N d\Omega}{\gamma N d\Omega + \gamma} = \frac{N d\Omega}{N d\Omega + 1}, \quad (2.16)$$

where N is the number of atoms, and $d\Omega$ is the solid angle in which we have constructive interference. As discussed above, the detection solid angle is determined by the shape of the atomic ensemble. Under the single mode condition $d\Omega \sim \frac{\lambda^2}{A}$, a direct calculation shows that the retrieval efficiency $\eta_{ret} \sim 1 - 1/d_0$ is determined by the optical depth. Note that taking into account the narrow EIT window, the error in retrieval efficiency scales as $\frac{1}{\sqrt{d_0}}$ [59].

The anti-Stokes field couples the excited state and ground state $|g\rangle$, while it won't be absorbed since the atom-light system fulfills the EIT condition. In this case the anti-Stokes light propagates in the atomic ensemble slower than the read light. Thus we require the read light pulse is sufficient long so that all the anti-Stokes light can propagate out of the atomic ensemble.

The collective state excitation stored in the atomic ensemble suffers from several decoherence mechanisms, e.g., the Larmor precession in a residual magnetic field \mathbf{B} [60] and the thermal atomic motion at a temperature of T_{tem} . After a storage time of t , the i th atom will move to $\mathbf{r}_i(t)$ and the collective state will evolve to

$$|\phi_e(t)\rangle = \frac{1}{\sqrt{N}} \sum_i^N e^{i\Delta\mathbf{k}\cdot\mathbf{r}_i} e^{-i\delta\omega_{sg}^i t} |g\dots s_i\dots g\rangle, \quad (2.17)$$

with $\delta\omega_{sg}^i$ the relative shift between $|g\rangle$ and $|s\rangle$. If the magnetic field is along the axial direction and there is a gradient in the magnetic field, we will have $\delta\omega_i \sim \alpha z_i$ with α a constant determined by the gradient of the magnetic field. The anti-Stokes field on the observation surface is given by

$$E(\mathbf{r}', t) = \frac{\zeta(\mathbf{r}')}{\sqrt{N}} \sum_i^N e^{i\Delta\mathbf{k}\cdot\delta\mathbf{r}_i(t)} e^{-i\delta\omega_{sg}^i t} \quad (2.18)$$

$$\simeq \sqrt{N} \zeta(\mathbf{r}') \int d\mathbf{r}'' n(\mathbf{r}'') e^{i\Delta\mathbf{k}\cdot\delta\mathbf{r}''(t)} e^{-i\alpha z'' t} \quad (2.19)$$

with $\delta \mathbf{r}_i(t) = \mathbf{r}_i - \mathbf{r}_i(t)$, where we have assumed $\mathbf{k}_W - \mathbf{k}_S + \mathbf{k}_R - \mathbf{k}_{AS} = 0$ and neglected energy shift induced by thermal motion. If the magnetic field is well compensated and the clock state is used, the effect of the residual magnetic field can be neglected [61]. Approximating the atomic motion by a Boltzmann distribution, we obtain the time dependent retrieval efficiency

$$\eta_{ret}(t) = \frac{Nd\Omega e^{-\Delta k^2 t^2 v^2}}{Nd\Omega e^{-\Delta k^2 t^2 v^2} + 1} \sim e^{-\Delta k^2 t^2 v^2} \quad (2.20)$$

with $v = \sqrt{\frac{k_B T_{lem}}{m}}$. Thus we get the lifetime due to thermal motion $\tau_m \sim \frac{1}{\Delta k v}$.

To get a more clearer picture, we use the dark-state polariton theory [62, 63] to describe the read process. The read light is given by $\mathbf{E}_R(\mathbf{r}, t) = \hat{\epsilon}_R E_R(\mathbf{r}, t) e^{i\mathbf{k}_R \cdot \mathbf{r} - i\omega_R t} + \text{H.c.}$, where $\hat{\epsilon}_R$ is the polarization unit vector, $\omega_R = ck_R$ is the frequency of the read light. The retrieved anti-Stokes field is approximated by a single mode light $\mathbf{E}_{AS}(\mathbf{r}, t) = \hat{\epsilon}_{AS} a_{AS} e^{i\mathbf{k}_{AS} \cdot \mathbf{r} - i\omega_{AS} t} + \text{H.c.}$ The Hamiltonian describing the read process is given by

$$H = \sum_i^N \{ \hbar\omega_{eg} \sigma_{ee}^i + \hbar\omega_{sg} \sigma_{ss}^i + [-\hbar\Omega_R(\mathbf{r}_i, t) e^{i\mathbf{k}_R \cdot \mathbf{r}_i - i\omega_R t} \sigma_{es}^i + \hbar g_{AS} a_{AS} e^{i\mathbf{k}_{AS} \cdot \mathbf{r}_i - i\omega_{AS} t} \sigma_{eg}^i + \text{H.c.}] \} \quad (2.21)$$

with $\Omega_R(\mathbf{r}, t)$ the Rabi frequency of the read light and g_{AS} the coupling coefficient. This Hamiltonian has a series of adiabatic eigenstates with vanishing excited state component, dark state polariton. The simplest dark state polariton can be described by

$$|D, 1\rangle = (\cos\theta a_{AS}^\dagger - \sin\theta S'^\dagger) |vac\rangle, \quad (2.22)$$

where $\tan\theta = \frac{g\sqrt{N}}{\Omega_R(t)}$ and $S'^\dagger = \frac{1}{\sqrt{N}} \sum_i^N e^{i\Delta\mathbf{k}' \cdot \mathbf{r}_i} \sigma_{sg}^i$ with $\Delta\mathbf{k}' = \mathbf{k}_R - \mathbf{k}_{AS}$. If the Rabi frequency adiabatically change from 0 to a relatively large value, θ will vary from $\pi/2$ to 0. Consequently, the dark state polariton will change from the collective excited state to the ground state and simultaneously emit an anti Stokes photon. Therefore, if the collective state imprinted in the write process $S^\dagger|0\rangle_a$ is the same as the collective state $S'^\dagger|0\rangle_a$ which can be fully retrieved out during the read process, the retrieve efficiency will reach the maximum. Again we obtain the mode match condition $\mathbf{k}_W - \mathbf{k}_S + \mathbf{k}_R - \mathbf{k}_{AS} = 0$. The retrieve efficiency after a storage time of t can be estimated by the overlap between Eq. (2.17) and $|\phi'_r(t)\rangle = \frac{1}{\sqrt{N}} \sum_i^N e^{i\Delta\mathbf{k} \cdot \mathbf{r}_i(t)} |g \dots s_i \dots g\rangle$. A straight forward calculation shows

$$\begin{aligned} Q(t) &= |\langle \phi_\epsilon(t) | \phi'_r(t) \rangle|^2 = \left| \frac{1}{N} \sum_i^N e^{i\Delta\mathbf{k} \cdot \Delta\mathbf{r}_i(t)} e^{-i\delta\omega_{sg}^i t} \right|^2 \\ &= \left| \int d\mathbf{r}'' n(\mathbf{r}'') e^{i\Delta\mathbf{k} \cdot \Delta\mathbf{r}''(t)} e^{-i\alpha z'' t} \right|^2. \end{aligned} \quad (2.23)$$

The retrieve efficiency can be expressed as

$$\eta_{ret}(t) = \frac{Nd\Omega Q(t)}{Nd\Omega Q(t) + 1}. \quad (2.24)$$

It can be easily seen that the two methods are equivalent to each other. In the above

discussion, we already assumed the adiabatic condition is satisfied, and the write and read light are homogeneous in the atomic ensemble. A detailed calculation considering more practical conditions can be found in Ref. [59].

After the retrieval process, the whole state of Stokes and anti-Stokes photon can be expressed as

$$|\psi\rangle = [1 + \sqrt{\chi}a_{AS}^\dagger a_S^\dagger]|vac\rangle_p. \quad (2.25)$$

It can be easily seen that once there is a photon detected in the Stokes field with a probability χ , we can obtain an anti-Stokes photon with certainty. This quantum mechanical correlation is the characteristic of the nonclassical correlated light generated from atomic ensembles.

2.4 The nonclassical correlation

In the above section, we only expand the perturbation theory to the first order. Taking into account higher excitation, the whole state of Stokes and anti-Stokes field can be described by [64]

$$\begin{aligned} |\psi\rangle &= [1 + \sqrt{\chi}a_{AS}^\dagger a_S^\dagger + \chi a_{AS}^{\dagger 2} a_S^{\dagger 2} / 2]|vac\rangle \\ &= |0_S 0_{AS}\rangle + \sqrt{\chi}|1_S 1_{AS}\rangle + \chi|2_S 2_{AS}\rangle, \end{aligned} \quad (2.26)$$

where $|n_S n_{AS}\rangle$ ($n = 0, 1, 2$) are the photon number states. The correlation between the Stokes photon and anti-Stokes photon is characterized by the Cauchy-Schwarz equality

$$[g_{S,AS}^{(2)}]^2 \leq g_S^{(2)} g_{AS}^{(2)} \quad (2.27)$$

with $g_{S,AS}^{(2)} = \langle a_S a_{AS} a_S^\dagger a_{AS}^\dagger \rangle / (\langle a_S a_S^\dagger \rangle \langle a_{AS} a_{AS}^\dagger \rangle)$ the cross-correlation between the Stokes photon and anti-Stokes photon, and $g_S^{(2)} = \langle a_S^2 a_S^{\dagger 2} \rangle / \langle a_S a_S^\dagger \rangle^2$ and $g_{AS}^{(2)} = \langle a_{AS}^2 a_{AS}^{\dagger 2} \rangle / \langle a_{AS} a_{AS}^\dagger \rangle^2$ the second order self-correlation. If the two photons are classically correlated, the Cauchy-Schwarz inequality is satisfied, otherwise the two field are nonclassically correlated. In our case we have $g_{S,AS}^{(2)} = 1/\chi$, and $g_S^{(2)} = g_{AS}^{(2)} = 2$. Therefore as long as the excitation probability is $\chi \ll 1$, the Cauchy-Schwarz inequality is significantly violated and we obtain two quantum mechanically correlated photons. Since the anti-Stokes photon is stored in the atomic ensemble, the nonclassical correlation can be exploited to implement deterministic single photon source [45, 46].

Chapter 3

Duan-Lukin-Cirac-Zoller protocol and the drawbacks

The Duan-Lukin-Cirac-Zoller protocol for long-distance quantum communication is attractive since it uses relatively simple ingredients, i.e., atomic ensembles and linear optics. Entanglement is generated and connected between memory qubits by exploiting single photon interference and single photon detection. In this chapter, we will review the DLCZ protocol and present a detailed analysis about the phase stabilization problem and entanglement distribution rate.

3.1 Introduction

Quantum communication ultimately aims at absolutely secure transfer of classical messages by means of quantum cryptography or faithful teleportation of unknown quantum states [6]. Photons are ideal quantum information carriers for quantum communication. Unfortunately, photon losses and the decrease in the quality of entanglement scale exponentially with the length of the communication channel. The quantum repeater protocol combining entanglement swapping and purification enables to establish high-quality long-distance entanglement with resources increasing only polynomially with transmission distance [36].

To implement the quantum repeater protocol, one has to generate entanglement between nearest memory qubits, store them for a sufficiently long time, and manipulate them by entanglement swapping and purification. Early physical implementations of a quantum repeater were based on atoms trapped in high-finesse cavities, where strong coupling between atoms and photons is required. In a seminal paper, Duan *et al.* (DLCZ) proposed an implementation of the quantum repeater by using atomic ensembles and linear optics [42]. In this protocol, atomic ensembles are used as memory qubits to avoid the challenging request for strong coupling between atoms and photons. The time overhead grows polynomially with the communication distance. In recent years, significant progress has been achieved along this direction. Entanglement between two atomic ensembles at a distance of 3 m is established [47], and the segment of DLCZ protocol is created by manipulating two pairs of atomic ensembles in parallel [65].

However, the DLCZ protocol has several severe drawbacks which make a realistic long-

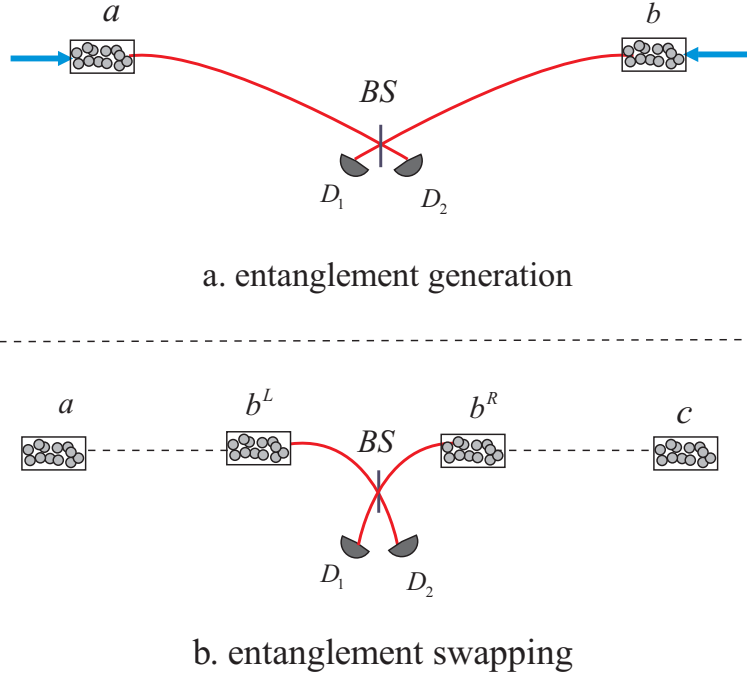


Figure 3.1: Setups for entanglement generation and entanglement swapping in the DLCZ protocol. (a) Forward scattered Stokes photons, generated by an off-resonant write laser pulse via spontaneous Raman transition, are directed to the beam splitter (BS) at the middle point. Entanglement is generated between atomic ensembles at sites a and b , once there is a click on either of the detectors. (b) Entanglement has been generated between atomic ensembles (a, b^L) and (b^R, c) . The atomic ensembles at site b are illuminated by near resonant read laser pulses, and the retrieved anti-Stokes photons are subject to the BS at the middle point. A click on either of the detectors will prepare the atomic ensembles at a and c into an entangled state

distance quantum communication impossible. Single photon Mach-Zehnder interference is used in both entanglement generation and entanglement swapping, which is sensitive to path length fluctuations [66]. The vacuum term and errors grow fast during entanglement connection [49, 67]. In order to obtain high fidelity, one has to choose an extremely small excitation probability, which implies a relatively low entanglement distribution rate [68]. In the following, we will first introduce the basic protocol and then analyze the drawbacks.

3.2 Basic protocol

Let us first consider a pencil shaped atomic sample of N atoms with Λ -type level structure. As we have discussed in chapter 2, the write laser pulse induces a spontaneous Raman process, which prepares the forward-scattered Stokes mode and collective atomic state into a two-mode squeezed state. The light-atom system is described as

$$|\psi\rangle = |0_a 0_s\rangle + \sqrt{\chi} S^\dagger a_s^\dagger |0_a 0_s\rangle \quad (3.1)$$

by neglecting higher-order terms, where $|0_a\rangle = \otimes_i |g\rangle_i$ is the ground state of the atomic ensemble and $|0_s\rangle$ denotes the vacuum state of the Stokes photons. The creation operator of the Stokes mode is a_s^\dagger , and the collective atomic excitation operator is defined by $S^\dagger = \frac{1}{\sqrt{N}} \sum_i \sigma_{sg}^i$, where we have neglected the wave vector $\Delta \mathbf{k}$ for simplicity. The small excitation probability $\chi \ll 1$ can be achieved by manipulating the write laser pulse.

The entanglement generation setup is shown in Fig. 3.1a. Let us consider two atomic ensembles at site a and b at a distance of $L_0 \leq L_{att}$, with L_{att} the channel attenuation length. The two atomic ensembles are excited simultaneously, and the Stokes photons generated from both sites are directed to the middle point. Then we combine the photons from two sites at the beam splitter (BS) and detect them by single photon detectors. Once there is a click on one of the detectors, entanglement between the atomic ensembles at sites a and b is established, described as

$$|\psi_{\phi_{ab}}\rangle_{a,b} = (S_a^\dagger + e^{i\phi_{ab}} S_b^\dagger) / \sqrt{2} |vac\rangle, \quad (3.2)$$

with ϕ an unknown phase generated due to the path length difference between the left and right channel.

Once the entanglement between nearest communication nodes are established. It can be extended to longer distance by performing entanglement swapping [3]. The entanglement swapping setup is depicted in Fig. 3.1b. Assume we have created entangled states between atomic ensembles (a, b^L) and (b^R, c) , where b^L and b^R are at the same site. The two atomic ensembles at site b are illuminated simultaneously by read laser pulses. The retrieved anti-Stokes photons are subject to the BS, and detected by single photon detectors. A click on either of the single photon detectors will prepare the atomic ensembles at sites a and c into a mixed entangled state with vacuum terms, described by

$$\rho_{a,c} = \frac{1}{c+1} (c |\psi_{\phi'}\rangle_{a,c} \langle \psi_{\phi'}| + |0\rangle_{a,c} \langle 0|), \quad (3.3)$$

where the coefficient c is determined by the retrieve efficiency and detection efficiency, and the new phase factor $\phi' = \phi_{ab} + \phi_{ac}$. The entangled state can be connected to arbitrary distance via entanglement swapping.

In practice we create two entangled pairs between two remote locations in parallel. When we are going to implement quantum cryptography via Ekert91 protocol [35], the entanglement between the two memory qubits are converted to photonic entanglement and detected by randomly choosing the detection bases. Only when there is a coincidence count between the two communication sites, the results are kept to generate the security key, otherwise they are discarded. From this point of view, the existence of vacuum term doesn't affect the quantum key distribution and the mixed entangled state is equivalent to a maximally entangled state. It is not difficult to find that the time needed to create the remote entangled pair scales polynomial with distance.

The DLCZ protocol has attracted many interests because it uses only linear optics and atomic ensembles to implement quantum repeater. However, it has severe practical drawbacks, i.e., phase stabilization problem and low entanglement distribution rate, which make a realistic long-distance quantum communication impossible.

3.3 Phase stabilization problem

3.3.1 Phase instability analysis I

In the DLCZ protocol, the single-photon Mach-Zehnder interference is used in both entanglement generation and entanglement swapping process. Thus the phase is sensitive to path length fluctuations on the order of photons' sub-wavelength. To implement quantum cryptography or Bell inequality detection, one has to create two pairs of entangled atomic ensembles in parallel. The entanglement generated between the two pairs of atomic ensembles is equivalent to a polarization maximally entangled state. In this case, the relative phase between the two entangled pairs needs to be stabilized, which is helpful to improve the phase instability [65]. However, the requirement to stabilize the relative phase in the DLCZ scheme is still extremely demanding for current techniques.

As shown in Fig. 3.2, in entanglement generation process the entanglement is established between the atomic ensembles (a_u, b_u) and (a_d, b_d) in parallel during a time interval $t_0 = \frac{T_{cc}}{\chi e^{-L_0/L_{att}}}$, where $T_{cc} = L_0/c$ is the classical communication time. Note that one requests $2^n \chi \ll 1$ to make the overall fidelity imperfection small, where n is the connection level. The entanglement generated between the two pairs of atomic ensembles can be described by

$$|\psi_{\phi_u}\rangle_{a_u, b_u} = (S_{a_u}^\dagger + e^{i\phi_u} S_{b_u}^\dagger)/\sqrt{2}|vac\rangle, \quad (3.4)$$

$$|\psi_{\phi_d}\rangle_{a_d, b_d} = (S_{a_d}^\dagger + e^{i\phi_d} S_{b_d}^\dagger)/\sqrt{2}|vac\rangle, \quad (3.5)$$

where $\phi_u = kx_u$ ($\phi_d = kx_d$) denotes the difference of the phase shifts in the left and the right side of channel u (d), with x_u (x_d) the length difference between the left and the right side channel u (d). Here k is the wave vector of the photons. For simplicity we have assumed the lasers on the two communication nodes have been synchronized, and the phase instability is caused by the path length fluctuations. The entanglement generated in this process is equivalent to a maximally entangled polarization state between the four atomic ensembles,

$$|\psi_{\delta\phi}\rangle_{PME} = (S_{a_u}^\dagger S_{b_u}^\dagger + e^{i\delta\phi} S_{a_d}^\dagger S_{b_d}^\dagger)/\sqrt{2}|vac\rangle, \quad (3.6)$$

where the relative phase between the entangled states of the two pairs of the remote ensembles is denoted by $\delta\phi = k\delta x$ with $\delta x = x_u - x_d$.

In practice, a series of write pulses are sent into the atomic ensembles and the induced Stokes pulses are directed to the detectors. The time interval between neighboring write pulses is larger than the classical communication time. When there is a click on the detectors, the entanglement is generated and classical information is sent back to the communication nodes to stop the subsequent write pulses. In this case, the change of environment due to imperfections will always induce path length fluctuations and thus phase instability. If the entanglement between the two pairs of memory qubits is always established at the same time, one can consider the Stokes photons detected at the same time experience the same environment. Thus it is easy to find $\delta x = x_u - x_d = 0$ and no phase stabilization is needed.

However entanglement generation process is probabilistic. The experiment has to be

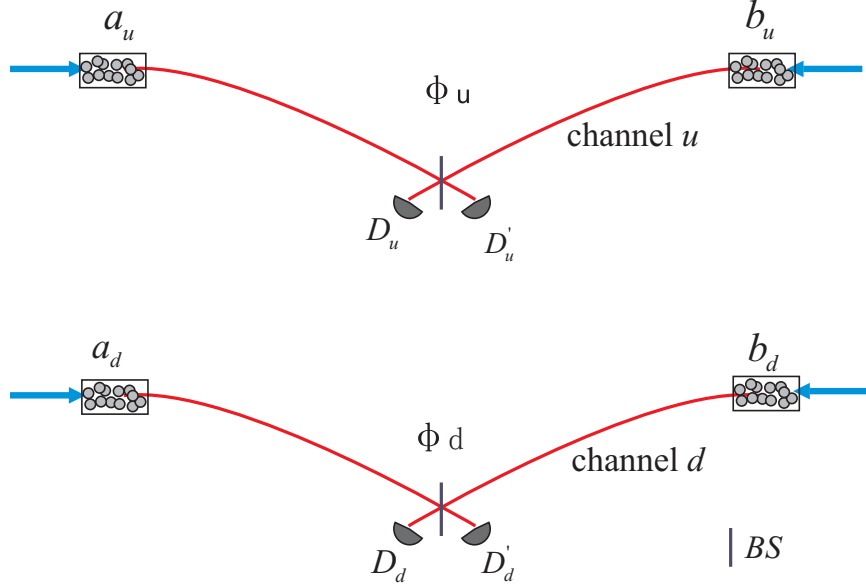


Figure 3.2: In the DLCZ protocol, two entangled pairs are generated in parallel. The relative phase between the two entangled states has to be stabilized during the entanglement generation process.

repeated about $1/(\chi e^{-L_0/L_{att}})$ times to ensure that there is a click on the detectors. The two phases ϕ_u and ϕ_d achieved at different runs of the experiments are usually different due to the path length fluctuations in this time interval. For instance, the entanglement between the first pair may be constructed after the first run of the experiment, and thus we get the phase $\phi_u = kx_u$, while the entanglement between the second pair may be established until the last run of the experiment, and thus we obtain the phase $\phi_d = kx_d$. Therefore to get a high fidelity entangled pair, the relative phase $\delta\phi = k\delta x$ has to be stabilized during the whole length of the communication. To stabilize the phase instability within $\delta\phi \leq 2\pi/10$, one must control the path length instability $\delta x \leq 0.1 \mu\text{m}$ during the whole entanglement generation process.

The path length instability is equivalent to the timing jitter of the arrival time of the Stokes pulses after transmitting the channel over kilometer-scale distances. To stabilize the path length instability $\delta x = c\delta t \leq 0.1 \mu\text{m}$, the timing jitter δt of the Stokes pulse must be controlled on the order of sub-femto second.

The time needed in entanglement generation process can be estimated as follows. The distance between two communication sites is considered to be $L_0 = 10 \text{ km}$, and thus the classical communication time $T_{cc} = L_0/c$ is about $33 \mu\text{s}$. Usually we have $2^n \approx 100$, and thus $\chi \approx 0.0001$. In optical fibers, the photon loss rate is considered to be 2 dB/km for photons at a wavelength of about 800 nm , and thus the duration t_0 of the entanglement generation process can be estimated to be about 30 seconds. Therefore, phase stabilization in DLCZ protocol requires that over a timescale of about a few tens of seconds, one must control the timing jitter after transferring a pulse sequence over several kilometers on the

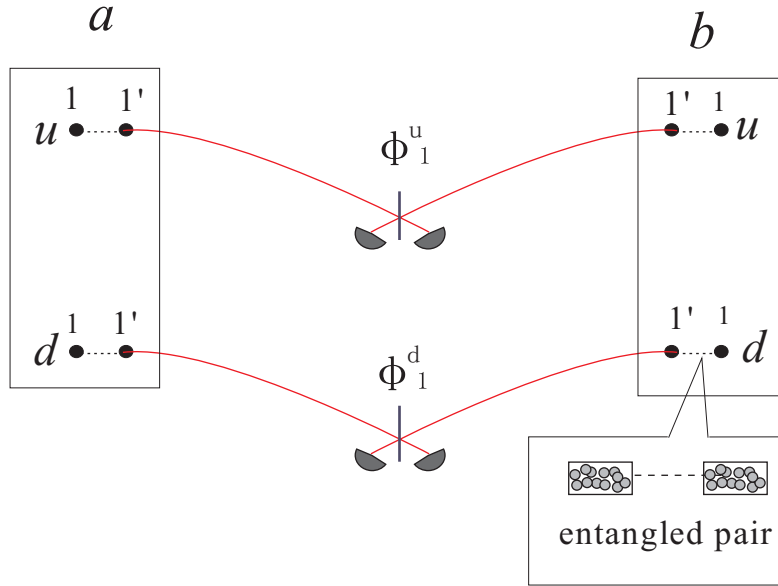


Figure 3.3: Elementary entangled pairs are created locally. Entanglement swapping is performed remotely to connect atomic ensembles between adjacent nodes a and b .

order of sub-femto second. This demand is extremely difficult for current technology. The lowest reported jitter for transferring of a timing signal over kilometer-scale distances is a few femto-seconds for averaging times of $\geq 1s$, which is 2 orders of magnitude worse than the timing jitter needed in the DLCZ protocol [69]. In free space, the photon loss rate is about 0.1 dB/km and t_0 is about 0.5 second. In this case, the path length instability due to atmosphere fluctuations is even worse. The timing jitter is on the order of a few nanoseconds over a timescale of 1 second [70].

3.3.2 Phase instability analysis II

From the above analysis, we know that in the standard DCLZ protocol, the requirement to stabilize the relative phase between the two entangled pairs is severe even in the entanglement generation stage. One may consider if entanglement generation is performed locally, the time needed in entanglement generation process is short and thus the requirement can be alleviated. However, that is not the case. It is a misunderstanding that the phase only needs to be stabilized in entanglement generation process. In the DLCZ protocol, the single-photon Mach-Zehnder interference is also utilized in entanglement swapping process. When performing entanglement swapping to connect the neighboring communication nodes, the phases have to be stabilized, too. In this subsection, we will give a detailed analysis to show that the phases between neighboring nodes have to be stabilized until the desired remote entangled pairs are constructed.

Suppose elementary entangled pairs are created locally at each node and the entanglement between neighboring nodes is generated via entanglement swapping, as shown in Fig. 3.3. In the entanglement swapping process, one has to send pulse sequences over a long

step	communication length and accumulated phase	time
1		t_1
2		$t_2 = t_1 / p_1$
3		$t_3 = t_2 / p_2$
4		$t_4 = t_3 / p_3$

Figure 3.4: Entangled pairs are generated between neighboring communication nodes as shown in Fig. 3.3. The entangled pairs are connected by performing further entanglement swapping to construct entanglement between remote communication sites A and B . The entanglement connection process, as well as the accumulated phase, is shown step by step.

distance and thus the path length fluctuations have to be controlled. The two entangled pairs obtained after entanglement swapping can be described by

$$|\psi_{\phi_1^u}\rangle_{a_{u_1}, b_{u_1}} = (S_{a_{u_1}}^\dagger + e^{i\phi_1^u} S_{b_{u_1}}^\dagger) / \sqrt{2} |vac\rangle, \quad (3.7)$$

$$|\psi_{\phi_1^d}\rangle_{a_{d_1}, b_{d_1}} = (S_{a_{d_1}}^\dagger + e^{i\phi_1^d} S_{b_{d_1}}^\dagger) / \sqrt{2} |vac\rangle. \quad (3.8)$$

Assume we are going to create the *up* and *down* entangled pairs between two remote communication sites A and B at a distance of $L = 2^3 L_0$. The entanglement connection process is shown step by step in Fig. 3.4. The entangled pairs between neighboring nodes are created as shown in Fig. 3.3 and then connected via further entanglement swapping which is also performed locally. After 4 steps, two remote entangled pairs between sites A and B are created,

$$|\Psi_{\Phi_u}\rangle_{A_u, B_u} = (S_{A_u}^\dagger + e^{i\Phi_u} S_{B_u}^\dagger) / \sqrt{2} |vac\rangle, \quad (3.9)$$

$$|\Psi_{\Phi_d}\rangle_{A_d, B_d} = (S_{A_d}^\dagger + e^{i\Phi_d} S_{B_d}^\dagger) / \sqrt{2} |vac\rangle, \quad (3.10)$$

where the accumulated phases are $\Phi_u = \sum_i \phi_i^u$ and $\Phi_d = \sum_i \phi_i^d$. The effectively maximally entangled pair can be described as

$$|\Psi_{\delta\Phi}\rangle_{PME} = (S_{A_u}^\dagger S_{B_u}^\dagger + e^{i\delta\Phi} S_{A_d}^\dagger S_{B_d}^\dagger) / \sqrt{2} |vac\rangle, \quad (3.11)$$

where $\delta\Phi = \Phi_u - \Phi_d = \sum_i (\phi_i^u - \phi_i^d)$ is the phase difference between the *up* and *down* entangled pairs. Note that the phases ϕ_i^u or ϕ_i^d ($i = 1, 2, \dots, 8$) between different nodes are independent from each other, and thus phase stabilization requires $\phi_i^u = \phi_i^d$ ($i = 1, 2, \dots, 8$).

Because entanglement swapping in every step is probabilistic, if the entanglement swapping does not succeed in one step, one has to repeat all the previous steps to reconstruct the entangled pairs. In this case, the phase has to be stabilized until the desired entangled pairs $|\Psi_{\Phi_u}\rangle_{A_u, B_u}$ and $|\Psi_{\Phi_d}\rangle_{A_d, B_d}$ are both generated. For example, suppose after step 3 we have created two *up* entangled pairs and two *down* entangled pairs in parallel. In step 4, we will connect the *up* and *down* pairs respectively via entanglement swapping to obtain the two desired entangled pairs between remote sites *A* and *B*. Since entanglement swapping is probabilistic, it could be that we succeed in connecting the *up* pairs and acquiring $|\Psi_{\Phi_u}\rangle_{A_u, B_u}$, but fail to connect the *down* pairs after performing entanglement swapping once. In this case, we have to repeat step 1, 2 and 3 to reconstruct the two *down* entangled pairs and then connect them by entanglement swapping to obtain $|\Psi_{\Phi_d}\rangle_{A_d, B_d}$. Since the phase Φ_u of the *up* pair has been fixed, the phases of the *down* pairs ϕ_i^d ($i = 1, 2, \dots, 8$) have to be stabilized to satisfy $\phi_i^u = \phi_i^d$ ($i = 1, 2, \dots, 8$), until the *down* pair $|\Psi_{\Phi_d}\rangle_{A_d, B_d}$ is successfully generated. The total time needed in these processes is $t_4 = t_1 / (p_1 p_2 p_3)$. In other words, the phases ϕ_i^u ($i = 1, 2, \dots, 8$) and ϕ_i^d ($i = 1, 2, \dots, 8$) have to be stabilized over a time interval $t_4 = t_1 / (p_1 p_2 p_3)$, until the desired remote entangled pairs $|\Psi_{\Phi_u}\rangle_{A_u, B_u}$ and $|\Psi_{\Phi_d}\rangle_{A_d, B_d}$ are both generated. For long-distance quantum communication, the total time needed is on the order of several hours [67, 68]. Even in the ideal case, it is still on the order of a few seconds. Therefore, phase stabilization in the DLCZ protocol requires that one has to stabilize the path length fluctuations over a long time interval after sending a pulse sequence over kilometer-scale distances. As we discussed above, it is extremely difficult for current technique to meet this demanding requirement.

3.4 The scalability analysis

Besides the phase stabilization problem, the entanglement distribution rate of the DLCZ protocol is extremely slow. The time needed to create a remote entangled pair can be calculated by [68]

$$T_{tot} = \left(\frac{3}{2}\right)^{n+1} \frac{L_0}{c} \frac{1}{P_0 P_1 \dots P_n P_{pr}}, \quad (3.12)$$

with $2^n = L/L_0$ the number of links, P_i ($i = 1, 2, \dots, n$) the success probability of *i*th entanglement swapping, and P_{pr} the probability to get a maximally entangled pair from the final mixed state. The total time needed to establish a remote entangled pair as a function of the communication distance is shown in Fig 3.5. In our calculation, the retrieval efficiency and the detection efficiency are assumed to be 90%, and the fidelity of the final entangled

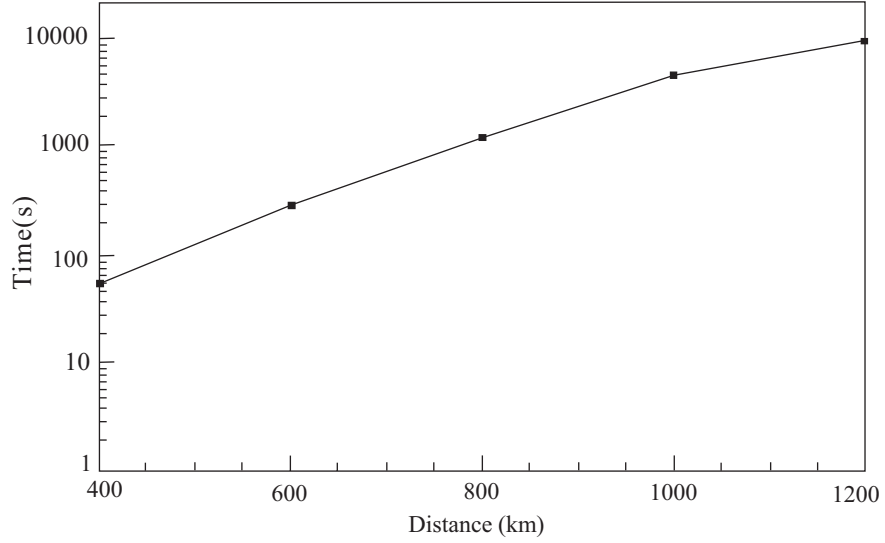


Figure 3.5: Entanglement distribution rate as a function of the communication distance.

state is 90 % as well.

One can see that it will cost a few hours to generate one entangled pair over 1000 km. The low entanglement distribution rate is mainly because the single-photon detections in entanglement swapping leads to the growth of the vacuum component in the generated state, and result in the rapid (quadratic with the number of links) growth of errors due to multiple emissions from individual ensembles. In order to suppress these errors, one then has to work with very low emission probabilities. These factors together lead to rather low entanglement distribution rates for the DLCZ protocol. Moreover, the DLCZ protocol does not contain a procedure for entanglement purification (of phase errors in particular), which limits the total number of links that can be used.

Chapter 4

Robust creation of entanglement between remote memory qubits

In this chapter we propose a robust quantum repeater architecture with atomic ensembles and linear optics. The architecture is based on two-photon Hong-Ou-Mandel-type interference which relaxes the long distance stability requirements by about 7 orders of magnitude, from sub wavelength for the single photon interference required by DLCZ to the coherence length of the photons. Our proposal provides an exciting possibility for robust and realistic long-distance quantum communication.

4.1 Introduction

Quantum communication holds the promise in achieving long-distance secure message transmission by exploiting quantum entanglement between remote locations [6]. For long-distance quantum communication one must realize quantum network via quantum repeater protocol, a combination of entanglement swapping, entanglement purification and quantum memory [36, 37]. In a seminal paper, Duan *et al.* (DLCZ) proposed a promising implementation of the quantum repeater with atomic ensembles as local memory qubits and linear optics [42]. In the effort of realizing the DLCZ protocol, significant progress has been achieved in recent years.

However, entanglement generation and entanglement swapping in the DLCZ protocol depend on Mach-Zehnder-type interference. The relative phase between two remote entangled pairs is sensitive to path length instabilities, which has to be kept constant within a fraction of photon's wavelength. Moreover, entanglement generation and entanglement swapping are probabilistic. If connecting neighboring entangled pairs doesn't succeed after performing entanglement swapping, one has to repeat all previous procedures to reconstruct the entangled pairs. This means the path length fluctuation must be stabilized until the desired remote entangled pairs are successfully generated. As we have discussed in chapter 3, to maintain path length phase instabilities at the level of $\lambda/10$ (λ :wavelength;

typically $\lambda \sim 1 \mu\text{m}$ for photons generated from atomic ensembles) requires the fine control of timing jitter at a sub-femto second level over a timescale of a few tens of seconds, no matter whether entanglement generation is performed locally or remotely. It is extremely difficult for current technology to meet this demanding requirement, since the lowest reported jitter is about a few tens of femto-seconds for transferring a timing signal over kilometer-scale distances for averaging times of $\geq 1 \text{ s}$ [69].

As is well known, the two-photon Hong-Ou-Mandel-type interference is insensitive to phase instability [71, 72, 73]. The path length fluctuations should be kept on the length scale within a fraction of photon's coherence length (say, 1/10 of the coherence length, which is about 3 m for photons generated from atomic ensembles [74, 75]). Therefore the robustness is improved about 7 orders of magnitude higher in comparison with the single-photon Mach-Zehnder-type interference in the DLCZ protocol. The interference of two photons from independent atomic ensembles has been reported recently [76, 77, 78]. This type of two-photon interference has been widely used in quantum communication and quantum computation [79, 80].

To exploit the advantage of two-photon interference, it is natural to extend the DLCZ protocol by polarization encoding a memory qubit with two atomic ensemble, and entangling two memory qubits at neighboring sites via a two-photon Bell-state measurement (BSM) [81]. Unfortunately, the BSM won't create the desired entangled state, but a complex superposition state with spurious contributions from second-order excitations, which preclude further entanglement manipulation (see details below).

In this chapter, we explore this problem and find that by appropriate designing the BSM, the spurious contributions from second-order excitations can be automatically eliminated when entanglement swapping is performed. Motivated by this advance we propose a robust quantum repeater architecture with atomic ensembles and linear optics. This scheme makes use of the two-photon Hong-Ou-Mandel-type interference, which is about 7 orders of magnitude more insensitive to path length phase instability than the DLCZ scheme, and thus enables a robust and feasible implementation of long-distance quantum communication.

4.2 Entanglement generation

Let us consider two sites A and B at a distance of $L_0 \leq L_{att}$, with L_{att} the channel attenuation length (see Fig. 4.1). Each site has two atomic ensembles encoded as one memory qubit and the two atomic ensembles at each node are excited simultaneously by write laser pulses. For each atomic ensemble, the quantum state of the light-atom system is given by

$$|\psi\rangle = |0_a 0_s\rangle + \sqrt{\chi} S^\dagger a_s^\dagger |0_a 0_s\rangle + \chi \frac{(S^\dagger a_s^\dagger)^2}{2} |0_a 0_s\rangle, \quad (4.1)$$

where we have expanded the quantum state to the second order because of the two-photon coincidence detection used in our protocol. We assume the Stokes photons generated from the two atomic ensembles at the same site have orthogonal polarization state, e.g., $|H\rangle$ and $|V\rangle$, which denote horizontal and vertical linear polarization respectively. In this way

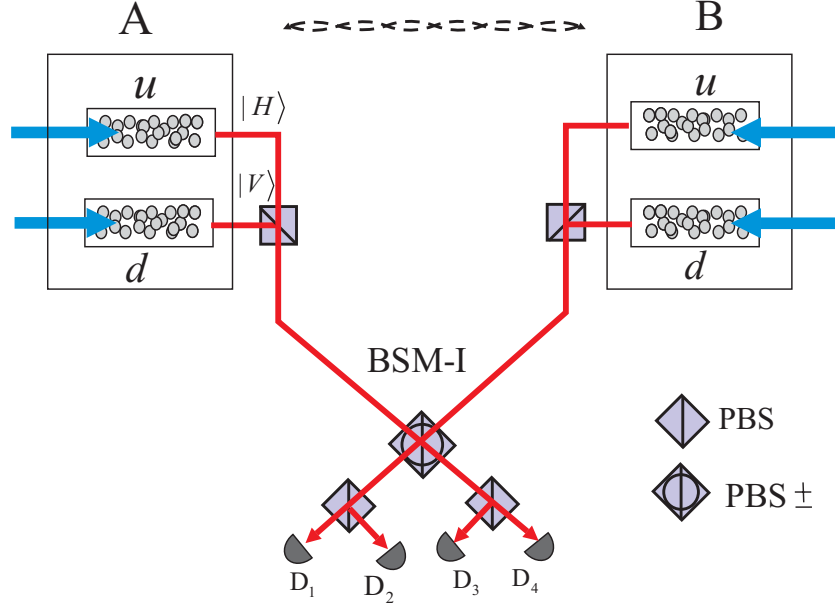


Figure 4.1: Setup for entanglement generation between sites A and B . Forward-scattered Stokes photons, generated by an off-resonant write laser pulse via spontaneous Raman transition, are subject to BSM-I at the middle point. The Stokes photons generated at the same site are assumed to have different polarization, i.e., $|H\rangle$ and $|V\rangle$. PBS (PBS_{\pm}) reflects photons with polarization $|V\rangle$ ($|-\rangle$) and transmits photons with polarization $|H\rangle$ ($|+\rangle$), where $|\pm\rangle = \frac{1}{\sqrt{2}}(|H\rangle \pm |V\rangle)$. After passing through the PBS_{\pm} and PBS successively, the Stokes photons are detected by single photon detectors. A coincidence count between single photon detectors D_1 and D_4 (D_1 and D_3) or D_2 and D_3 (D_2 and D_4) will project the four atomic ensembles into the complex entangled state $|\psi\rangle_{AB}$ up to a local unitary transformation.

the memory qubit is effectively entangled with the polarization state of the emitted Stokes photon.

The Stokes photons generated from both the sites are directed to the polarization beam splitter (PBS) and subject to BSM-I at the middle point to entangle the two neighboring memory qubits. However, the two-photon state generated in the second-order Spontaneous Raman process will also induce a coincidence count on the detectors. Thus BSM-I can only prepare the neighboring memory qubits into a complex superposition state with spurious contributions from second-order excitations. For instance, a coincidence count between D_1 and D_4 projects the two memory qubits into

$$\begin{aligned}
 |\psi\rangle_{AB} = & \left[\frac{e^{i(\phi_A + \phi_B)}}{2} (S_{u_A}^\dagger S_{u_B}^\dagger + S_{d_A}^\dagger S_{d_B}^\dagger) \right. \\
 & \left. + \frac{1}{4} (e^{i2\phi_A} S_{u_A}^{\dagger 2} + e^{i2\phi_B} S_{u_B}^{\dagger 2} - e^{i2\phi_A} S_{d_A}^{\dagger 2} - e^{i2\phi_B} S_{d_B}^{\dagger 2}) |vac\rangle \right], \quad (4.2)
 \end{aligned}$$

where the atomic ensembles are distinguished by subscript (u, d) and (A, B) , and ϕ_A and ϕ_B are the phases that the photons acquire from site A and B respectively during the BSM-I. The first part is the maximally entangled state needed for further operation, while the second part is the unwanted two-excitation state coming from second-order excitations.

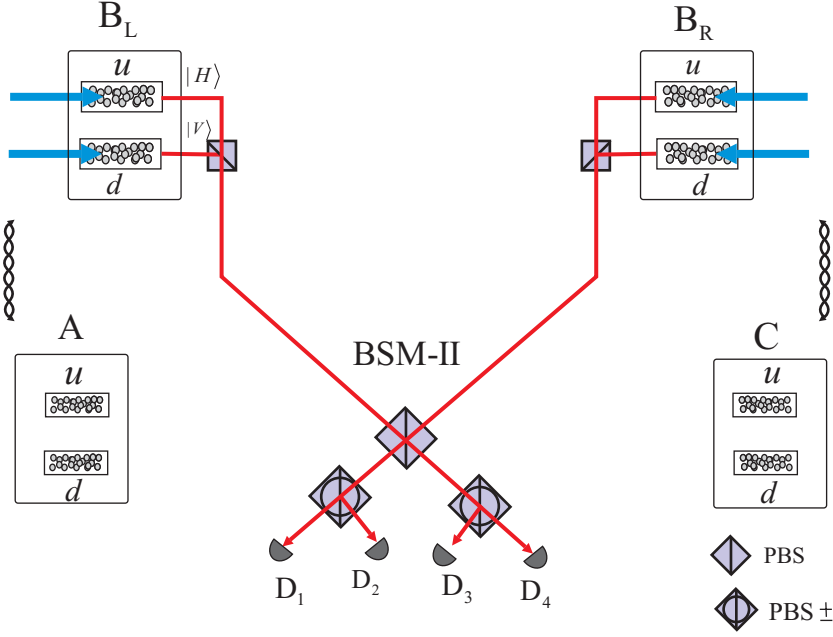


Figure 4.2: Setup for entanglement connection between sites A and C via entanglement swapping. Complex entangled states have been prepared in the memory qubits between sites (A, B_L) and (B_R, C) . The memory qubits at site B are illuminated by near resonant read laser pulses, and the retrieved anti-Stokes photons are subject to BSM-II at the middle point. The anti-Stokes photons at the same site have different polarizations $|H\rangle$ and $|V\rangle$. After passing through PBS and PBS_\pm successively, the anti-Stokes photons are detected by single photon detectors. Coincidence counts between D_1 and D_4 (D_1 and D_3) or D_2 and D_3 (D_2 and D_4) are registered. The memory qubits will be projected into an effectively maximally entangled state ρ_{AC} up to a local unitary transformation. Note that the sequence of PBSs in BSM-II is different from BSM-I. This helps to eliminate the spurious contributions from second-order excitations.

The success probability is on the order of $O(\chi^2 \eta_d^2 e^{-L_0/L_{att}})$ by considering the channel attenuation, where η_d is the detection efficiency. The time needed in this process is $T_0 \approx \frac{T_{cc}}{\chi^2 \eta_d^2 e^{-L_0/L_{att}}}$, with $T_{cc} = L_0/c$ the classical communication time.

It is obvious that the phases ϕ_A and ϕ_B only lead to a multiplicative factor $e^{i(\phi_A + \phi_B)}$ before the desired entangled state and thus have no effect on the desired entanglement. The prize to pay is that some spurious coincidence counts from the two-excitation terms are also registered, which obviously prevents further entanglement manipulation and must be eliminated by some means. However, we find that it is not necessary to worry about these terms, because they can be automatically washed out if the BSM in the entanglement swapping step is carefully designed. In the ideal case a maximally entangled state can be created by implementing entanglement swapping.

The entanglement swapping setup is depicted in Fig. 4.2. Let us consider three communication sites A, B and C , and assume that we have created the complex entangled states $|\psi\rangle_{AB_L}$ and $|\psi\rangle_{B_R C}$ between (A, B_L) and (B_R, C) , respectively. The memory qubits B_L and B_R at site B are illuminated simultaneously by read laser pulses. The retrieved anti-Stokes photons are subject to BSM-II. Note that the sequence of the PBSs in BSM-II is different from BSM-I. The BSM-II is designed like this in order that the two-photon

states converted from the spurious two-excitation terms are directed into the same output and thus will not induce a coincidence count on the detectors. In the ideal case, if the retrieve efficiency is unity and perfect photon detectors are used to distinguish photon numbers, only the two-photon coincidence count will be registered and project the memory qubits into a maximally entangled state. For instance, when a coincidence count between D_1 and D_4 is registered one will obtain

$$|\phi^+\rangle_{AC} = (S_{u_A}^\dagger S_{u_C}^\dagger + S_{d_A}^\dagger S_{d_C}^\dagger)/\sqrt{2}|vac\rangle. \quad (4.3)$$

In this way a maximally entangled state across sites A and C is generated by performing entanglement swapping. The maximally entangled state can be extended by further entanglement swapping as usual. Both the entanglement creation and entanglement connection in our scheme rely on two-photon interference, so the improvement in insensitivity to path length fluctuations, as compared to the DLCZ scheme, is about 7 orders of magnitude.

However, for realistic atomic ensembles the retrieve efficiency η_r is determined by optical depth of the atomic ensemble [82], and current single photon detectors are incapable of distinguishing photon numbers. Taking into account these imperfections, the multi-photon coincidence counts in BSM-II have to be considered. Through some simple calculations, one can find that the coincidence counts will prepare the memory qubits into a mixed entangled state of the form

$$\rho_{AC} = p_2\rho_2 + p_1\rho_1 + p_0\rho_0, \quad (4.4)$$

where the coefficients p_2 , p_1 and p_0 are determined by the retrieve efficiency and detection efficiency. The unnormalized coefficients are calculated to be

$$p_2^{(u)} = \frac{\eta_r^2 \eta_d^2}{32}, \quad (4.5)$$

$$p_1^{(u)} = \frac{\eta_r^2(1-\eta_r)\eta_d^2}{16} + \frac{\eta_r^3}{32}\left(\frac{\eta_d\eta_2}{2} + \eta_d^2\right), \quad (4.6)$$

$$p_0^{(u)} = \frac{\eta_r^3}{32}(1-\eta_r)\left(\frac{1}{2}\eta_d\eta_2 + \eta_d^2\right) + \frac{\eta_r^2(1-\eta_r)^2\eta_d^2}{32} + \frac{\eta_r^4}{64}\left(\frac{1}{4}\eta_2^2 + \eta_d^2\right), \quad (4.7)$$

with $\eta_2 = \eta_d^2 + 2\eta_d(1-\eta_d)$ the detection efficiency for two photon state. The success probability of entanglement swapping is $p = p_2^{(u)} + p_1^{(u)} + p_0^{(u)}$. Here $\rho_2 = |\phi^+\rangle_{AC}\langle\phi^+|$ is a maximally entangled state, ρ_1 is a maximally mixed state, where only one of the four atomic ensembles has one excitation, and ρ_0 is the vacuum state that all the atomic ensembles are in the ground states.

It is easy to see that ρ_{AC} is in fact an effectively maximally entangled states, which can be projected automatically to a maximally entangled state in the entanglement based quantum cryptography schemes. When implementing quantum cryptography via the Ekert protocol, we randomly choose the detection basis at the remote sites and detect the photons retrieved from the atomic ensembles. Then we compare the detection basis by classical communication. In this process, only the coincidence counts are registered and

used for quantum cryptography. In our case only the first term ρ_2 will contribute to a coincidence count between the detectors at the two sites and will be registered after classical communication. The maximally mixed state term ρ_1 and the vacuum term ρ_0 have no contribution to the experimental results, and thus ρ_{AC} is equivalent to the Bell state $|\phi^+\rangle_{AC} = (S_{u_A}^\dagger S_{u_C}^\dagger + S_{d_A}^\dagger S_{d_C}^\dagger)/\sqrt{2}|vac\rangle$.

4.3 Entanglement connection and scalability

The effectively entangled state can be connected to longer communication distance via further entanglement swapping. Taking into account high-order excitations in the spontaneous Raman process, the effectively entangled pair can be described by $\rho' = \rho + p'_2\rho'_2 + p'_3\rho'_3$. Here we introduce two-excitation density matrix ρ'_2 , containing the terms $S_{u_A}^{\dagger 2}, S_{d_C}^{\dagger 2}, S_{u_A}^\dagger S_{d_A}^\dagger, S_{u_A}^\dagger S_{u_C}^\dagger$ etc., and three-excitation density matrix ρ'_3 , containing the terms $S_{u_A}^{\dagger 2} S_{u_C}^\dagger, S_{d_C}^{\dagger 2} S_{u_A}^\dagger, S_{u_A}^\dagger S_{u_C}^\dagger S_{d_C}^\dagger, S_{u_A}^\dagger S_{d_A}^\dagger S_{u_C}^\dagger$ etc., to denote the contributions from higher-order excitations. The small efficient p'_2 and p'_3 are on the order of $O(\chi) \ll 1$. After the j -th ($j \geq 2$) swapping step, the effective entangled pair can be described as

$$\rho'_{s_j} = p_{2s_j}\rho_{2s_j} + p_{1s_j}\rho_{1s_j} + p_{0s_j}\rho_{0s_j} + p'_{2s_j}\rho'_{2s_j} + p'_{3s_j}\rho'_{3s_j} \quad (4.8)$$

Here ρ_{2s_j} is the maximally entangled state between two memory qubits at a distance of $L = 2^j L_0$, and ρ_{1s_j}, ρ_{0s_j} are also the maximally mixed state and vacuum state respectively. Note that $\rho'_{s_1} = \rho'$ is just the mixed entangled state created after the first entanglement swapping step. The unnormalized coefficients can be calculated to be

$$p_{2s_j}^{(u)} \approx \frac{1}{2}p_{2s_{j-1}}^2 \eta^2, \quad (4.9)$$

$$p_{1s_j}^{(u)} \approx \frac{1}{2}\eta^2[p_{1s_{j-1}}p_{2s_{j-1}} + O(p_{2s_{j-1}}p'_{2s_{j-1}}) + O(p_{1s_{j-1}}p'_{2s_{j-1}}) + O(p_{0s_{j-1}}p'_{3s_{j-1}})], \quad (4.10)$$

$$p_{0s_j}^{(u)} \approx \frac{1}{8}\eta^2[p_{1s_{j-1}}^2 + O(p_{0s_{j-1}}p'_{2s_{j-1}})], \quad (4.11)$$

$$p_{2s_j}^{(u)} \sim O(p_{2s_{j-1}}p_{2s_{j-1}}^2 \eta) + O(p_{1s_{j-1}}p'_{3s_{j-1}} \eta), \quad (4.12)$$

$$p_{3s_j}^{(u)} \sim O(p_{2s_{j-1}}p'_{3s_{j-1}} \eta), \quad (4.13)$$

with $\eta = \eta_d \eta_r$, where the three-photon coincidence counts are safely neglected. From the above equations, we find that

$$p_{3s_j}^{(u)}/p_{2s_j}^{(u)} \sim O(p'_{3s_{j-1}}/p_{2s_{j-1}}) \sim O(\chi/p_2), \quad (4.14)$$

$$p_{2s_j}^{(u)}/p_{2s_j}^{(u)} \sim O(p'_{2s_{j-1}}/p_{2s_{j-1}}) + O(p'_{3s_{j-1}}/p_{2s_{j-1}}) \sim O(j\chi/p_2), \quad (4.15)$$

$$p_{1s_j}^{(u)}/p_{2s_j}^{(u)} \approx p_{1s_{j-1}}/p_{2s_{j-1}} + O(p'_{3s_{j-1}}/p_{2s_{j-1}}) + O(p'_{2s_{j-1}}/p_{2s_{j-1}}), \quad (4.16)$$

$$p_{0s_j}^{(u)}/p_{2s_j}^{(u)} \approx \frac{1}{4}(p_{1s_{j-1}}/p_{2s_{j-1}})^2 + O(p'_{2s_{j-1}}/p_{2s_{j-1}}), \quad (4.17)$$

where we have considered the coefficients $p_{2s_{j-1}}, p_{1s_{j-1}}$, and $p_{0s_{j-1}}$ are on the same order of magnitude. Finally, we conclude that during the nesting entanglement connection process,

the coefficients can be estimated to be

$$p'_{3s_j} \sim O(\chi), p'_{2s_j} \sim O(j\chi), \quad (4.18)$$

$$p_{\alpha s_j} \approx p_{\alpha s_{j-1}} + O(j\chi), (\alpha = 0, 1, 2). \quad (4.19)$$

The success probability of the j -th entanglement connection is $p_{s_j} = p_{2s_j}^{(u)} + p_{1s_j}^{(u)} + p_{0s_j}^{(u)}$.

It is readily seen that the contributions from higher-order excitations can be safely neglected, as long as the small excitation probability fulfills $j\chi \ll 1$, which can be easily achieved by tuning the write laser pulse. One can also see that the coefficients p_{2s_j} , p_{1s_j} and p_{0s_j} are stable to the first order, therefore the probability to find an entangled pair in the remaining memory qubits is almost a constant and will not decrease significantly with distance during the entanglement connection process. The time needed for the j -th connection step satisfies the iteration formula $T_{s_j} = \frac{1}{p_{s_j}}[T_{s_{j-1}} + 2^{j-1}T_{cc}]$ with p_{s_j} the success probability of the j -th swapping step. The total time needed for the entanglement connection process is

$$T_{tot} \approx T_0 \prod_j p_{s_j}^{-1} \approx \frac{T_{cc}}{\chi^2 \eta_d^2} e^{L_0/Latt} (L/L_0)^{\log_2(1/\eta^2)}, \quad (4.20)$$

where $\eta = \eta_r \eta_d$ is the product of the retrieval efficiency and the detection efficiency. The excitation probability can be estimated to be $\chi \sim L_0/L$, and then the time needed in the entanglement connection process $T_{tot} \propto (L/L_0)^{2+\log_2(1/\eta^2)}$ scales polynomially or quadratically with the communication distance.

4.4 Entanglement purification

With imperfect entanglement and erroneous local operations, entanglement connection, together with decoherence, will reduce the fidelity of entanglement. Then at certain stage of entanglement connection, the less entangled states have to be actively purified via the entanglement purification protocol to enable further entanglement connection [39, 83, 84]. Fig. 4.3 shows how to achieve linear optical entanglement purification between any specified two nodes, e.g., nodes I and J across which one has less entangled pairs of quantum memories.

Suppose we have generated an effectively mixed entangled state $\rho_m = p_{2m}\rho_{2m} + p_{1m}\rho_{1m} + p_{0m}\rho_{0m}$ of fidelity F across nodes I and J . For simplicity, we assume the mixed state is of the form $\rho_{2m} = F|\phi^+\rangle_{IJ}\langle\phi^+| + (1-F)|\psi^+\rangle_{IJ}\langle\psi^+|$, with $|\phi^+\rangle_{IJ} = (S_{u_I}^\dagger S_{u_J}^\dagger + S_{d_I}^\dagger S_{d_J}^\dagger)/\sqrt{2}|vac\rangle$ and $|\psi^+\rangle_{ij} = (S_{u_I}^\dagger S_{d_J}^\dagger + S_{d_I}^\dagger S_{u_J}^\dagger)/\sqrt{2}|vac\rangle$. As shown in Fig. 4.3, the effectively entangled states stored in the four memory qubits are converted into entangled photons by the read laser pulses, and then subject to two PBSs respectively. The photons in modes b_1 and b_2 are detected in $|\pm\rangle = \frac{1}{\sqrt{2}}(|H\rangle \pm |V\rangle)$ basis by single photon detectors, and will project the photons in modes a_1 and a_2 into an effectively maximally entangled state of higher fidelity $F' = \frac{F^2}{F^2 + (1-F)^2}$, which can be described as

$$\rho_p = p_{2p}\rho_{2p} + p_{1p}\rho_{1p} + p_{0p}\rho_{0p}, \quad (4.21)$$

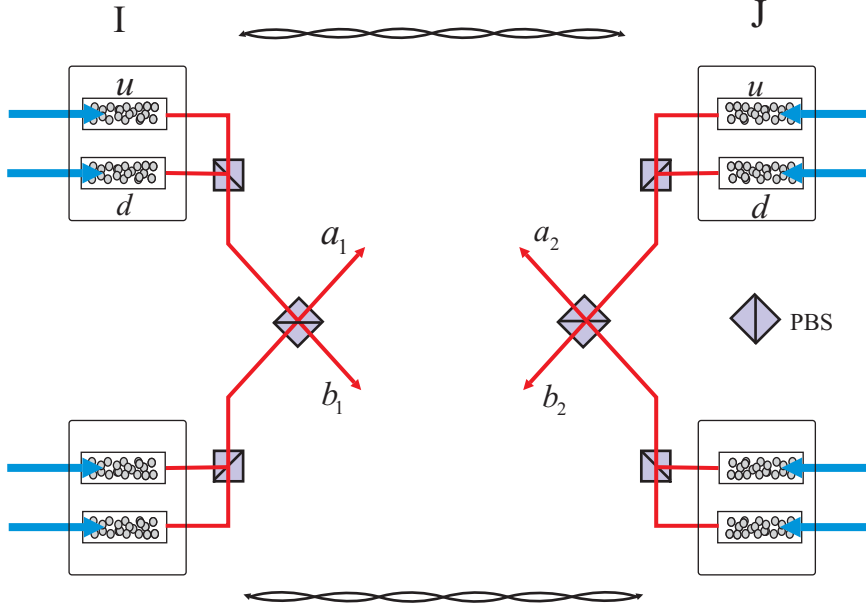


Figure 4.3: Setup for quantum entanglement purification. Effectively entangled states have been prepared in the memory qubits between two distant sites I and J . The memory qubits at the two sites are illuminated by near resonant read laser pulse, and the retrieved entangled photon pairs are directed to two PBS respectively. The photons in modes b_1 and b_2 are detected in $|\pm\rangle = \frac{1}{\sqrt{2}}(|H\rangle \pm |V\rangle)$ basis and the left photons in modes a_1 and a_2 are restored in the memory qubits at the two sites respectively.

with $\rho_{2p} = F'|\phi^+\rangle_{IJ}\langle\phi^+| + (1 - F')|\psi^+\rangle_{IJ}\langle\psi^+|$. The unnormalized coefficients are

$$p_{2p}^{(u)} = \frac{1}{2}p_{2m}^2\eta_r^4\eta_d^2[F^2 + (1 - F)^2], \quad (4.22)$$

$$p_{1p}^{(u)} = p_{2m}^2\eta_r^3(1 - \eta_r)\eta_d^2 + \frac{1}{2}p_{1m}p_{2m}\eta_r^3\eta_d^2 + p_{2m}^2\eta_r^4F(1 - F)\eta_d\eta_2, \quad (4.23)$$

$$\begin{aligned} p_{0p}^{(u)} &= p_{2m}^2\left[\frac{1}{4}\eta_r^4F^2\eta_2^2 + \eta_r^3(1 - \eta_r)F(1 - F)\eta_d\eta_2\right. \\ &\quad \left.+ \eta_r^2(1 - \eta_r)^2(F + 1/2)\eta_d^2 + \eta_r^3(1 - \eta_r)F^2\eta_d\eta_2\right] \\ &\quad \left.+ p_{2m}p_{1m}[\eta_r^2(1 - \eta_r)(F_m + 1/2)\eta_d^2 + \eta_r^3\frac{F}{2}\eta_d\eta_2] + \frac{1}{8}p_{1m}^2\eta_r^2\eta_d^2 + p_{2m}p_{0m}\eta_r^2F\eta_d^2. \right. \end{aligned} \quad (4.24)$$

The success probability of entanglement purification is $p_p = p_{2p}^{(u)} + p_{1p}^{(u)} + p_{0p}^{(u)}$.

4.5 Discussion

To generate a remote entangled pair, nested quantum purification has to be implemented. The total time overhead to create entanglement across two communication nodes at a distance of 1280 km can be numerically estimated. In our calculation, we assume the

distance $L_0 = 10$ km and the photon loss rate is considered to be 0.1 dB/km in free space [70]. The initial fidelity is assumed to be $F = 0.88$. To increase the efficiency, we assume high efficiency (99%) photon counting detectors based on atomic ensembles are used [85, 86], and the retrieve efficiency is considered to be 98%. Entanglement purification is performed twice during the whole process to improve the fidelity. Our scheme also relies on the ability to reliably transfer of photon's polarization states over a free-space or optical fiber channel. Two recent experiments demonstrated this ability up to 100 km in free space [33] and in fiber [32]. Our numerical results give a total time of about three hours to create an effectively entangled pair, with a probability of 0.85 to get the entangled pair of fidelity 95%.

Recently, several atomic-ensemble-based quantum repeater schemes were proposed building on the DLCZ protocol. These schemes still have phase stability problem since single-photon interference is also used in some stages. The scheme presented in Ref. [67] is similar to our protocol, where they gave a detailed analysis on the superior scalability of polarization encoding. However, single-photon interference is used in entanglement generation process, and thus entanglement generation should be performed locally. In Ref. [68], Simon *et al.* proposed a quantum repeater, where they suggested to make entanglement generation attempts many times with the help of photon pairs and multi-mode memories. The use of multi-mode memories promises a speedup in entanglement generation by several orders of magnitude. However, entanglement generation and entanglement swapping in this protocol need single-photon interference. The phase stabilization problem can be overcome by using those cases where the entanglement swapping succeeds at the same time for the upper and lower chains. Besides, the fidelity of the final entanglement is sensitive to phase instability due to the lack of entanglement purification. It was pointed out that in this type of protocol, an initial small phase error will induce the final entanglement fidelity no more than 65% [67].

The ideas of polarization encoding, two-photon BSM and active entanglement purification presented in our protocol is crucial to long distance quantum communication. The combination of these ideas enables a realistic fault-tolerant quantum repeater with atomic ensembles and linear optics.

Chapter 5

A fast quantum repeater with high-quality local entanglement

In this chapter, we show that the local generation of high-fidelity entangled pairs of atomic excitations, in combination with the use of two-photon detections for long-distance entanglement generation, permits the implementation of an attractive quantum repeater protocol. Such a repeater is robust with respect to phase fluctuations in the transmission channels, and at the same time achieves higher entanglement generation rates than other protocols using the same ingredients.

5.1 Introduction

The distribution of entangled states over long distances is difficult because of unavoidable transmission losses and the no-cloning theorem for quantum states. One possible solution is the use of quantum repeaters [36]. In this approach, entanglement is generated independently for relatively short elementary links and stored in quantum memories. Entanglement over longer distances can then be created by entanglement swapping [3].

The DLCZ protocol holds the promise to implement long distance quantum communication with relatively simple ingredients, i.e., atomic ensembles and linear optics [42]. Over the last few years there has been a lot of experimental activity towards its realization, including the creation of entanglement between separate quantum nodes [65] and the realization of teleportation between photonic and atomic qubits [87]. Conversion efficiencies from atomic to photonic excitations as high as 84 percent have recently been achieved for ensembles inside optical cavities [88].

However the DLCZ protocol has a certain number of serious practical drawbacks. On the one hand, the generation of entanglement via single-photon detections requires interferometric stability over the whole distance for a long time, which a priori seems quite challenging. For recent experimental work towards assessing the feasibility of this requirement for optical fiber links see Ref. [89]. On the other hand, the swapping of entanglement

using single-photon detections leads to the growth of a vacuum component in the generated state, and to the rapid (quadratic with the number of links) growth of errors due to multiple emissions from individual ensembles. In order to suppress these errors, one then has to work with very low emission probabilities. These factors together lead to rather low entanglement distribution rates for the DLCZ protocol. Moreover, the DLCZ protocol does not contain a procedure for entanglement purification which limits the total number of links that can be used.

Ref. [67] recently proposed a modification of the DLCZ protocol in which entanglement is still generated by single-photon detections, but entanglement swapping is based on two-photon detections. As a consequence, the vacuum component remains constant under entanglement swapping, multi-photon errors grow only linearly, and entanglement purification with linear optics is possible. However the achieved rates are only slightly better than for the DLCZ protocol for distances of order 1000 km, mainly because errors in the elementary link due to multiple excitations still force one to work with low emission probabilities. Multiple excitations are hard to detect in the entanglement generation process because the corresponding Stokes photons have to propagate far and are lost with high probability.

Ref. [90] uses single-photon detections for entanglement generation and swapping, but the method of entanglement generation is different with respect to the DLCZ protocol, relying on single-photon sources. This makes it possible to improve the distribution rate of entangled states, thanks to the suppression of multi-photon errors. This protocol can be realized with atomic ensembles and linear optics because a quasi-ideal single-photon source can be constructed based on atomic ensembles of the DLCZ type. The probabilistic emission of the Stokes photon heralds the creation of an atomic excitation in the ensemble. The charged memory can now be used as a single-photon source by reconvertng the stored excitation into an anti-Stokes photon. The probability for this source to emit two anti-Stokes photons can be made arbitrarily small by working with a small emission probability for the Stokes photon. The price to pay is that the preparation of the source requires many attempts until the Stokes photon is emitted. However, these attempts are purely local and can thus be repeated very fast. The protocol of Ref. [90] is faster than the DLCZ protocol. However it shares the need for phase stability, the amplification of vacuum and multi-photon components, and the absence of a known entanglement purification procedure.

In chapter 4 we proposed a scheme in which both entanglement creation and swapping are based on two-photon detections. In addition to the advantages mentioned for Ref. [67], this protocol no longer requires interferometric stability over long distances. However, entanglement is directly generated over long distances. Since only a small excitation probability can be used for each entanglement generation attempt (in order to avoid multi-photon errors), and since after every attempt one has to communicate its success or failure over a long distance, the required entanglement generation time becomes longer than for the DLCZ protocol.

In the following we present an improved quantum repeater with locally generated high-fidelity entangled pairs and two-photon interference. We find that the use of locally generated entangled pairs leads to a significant improvement in the achievable entanglement

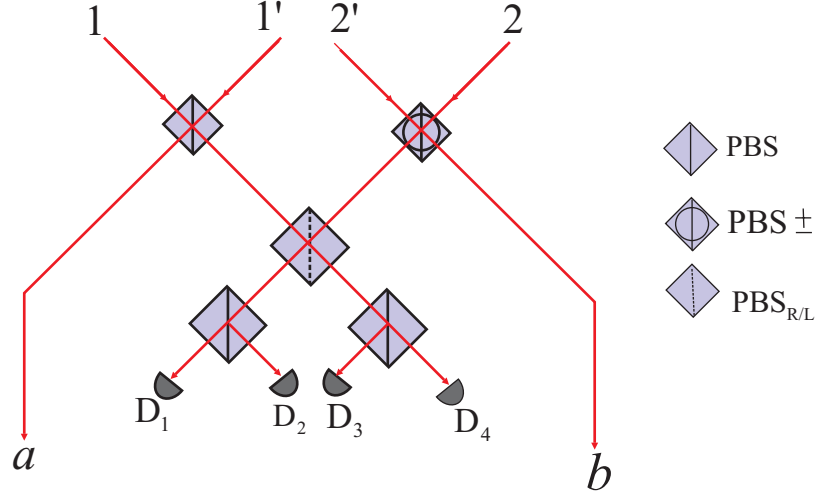


Figure 5.1: Deterministic single-photon polarization entangler. PBS (PBS_{\pm} ; $\text{PBS}_{R/L}$) reflects photons with vertical polarization $|V\rangle(|-\rangle; |L\rangle)$ and transmits photons with horizontal-polarization $|H\rangle(|+\rangle; |R\rangle)$. Here $|\pm\rangle = \frac{1}{\sqrt{2}}(|H\rangle + |V\rangle)$; $|R/L\rangle = \frac{1}{\sqrt{2}}(|H\rangle \pm i|V\rangle)$. The four single photons are prepared on demand in an initial state $|-\rangle_1|V\rangle_2|+\rangle_{1'}|H\rangle_{2'}$. After passing through the first PBS and PBS_{\pm} , one selects the ‘four-mode’ case where there is one and only one photon in each of the four output modes. Then the BSM will collapse photons in modes a and b into a Bell state conditioned on the result of the BSM. In our case, a coincidence count between single-photon detectors D_1 and D_4 (D_1 and D_3) or between D_2 and D_3 (D_2 and D_4) leaving photons along paths a and b deterministically entangled in $|\psi^+\rangle_{ab}(|\phi^-\rangle_{ab})$.

generation rate over long distances.

5.2 Locally generated quasi-ideal entangled pair

The high-fidelity local entangled pairs of atomic excitations can be generated using four single-photon sources, (which can be realized with DLCZ-type ensembles), linear optical elements, and two EIT-based quantum memories.

The deterministic single-photon polarization entangler is depicted in Fig. 5.1 [91]. In the ideal case where single photons can be created on demand and photon-number counting detectors are used to identify the Bell states, we will obtain two maximally entangled photons in $|\psi^+\rangle_{ab}$ or $|\phi^-\rangle_{ab}$, conditioned on a coincidence count in two of the four detectors with a success probability of $\frac{1}{8}$.

However, current single photon sources are probabilistic and the mostly used single photon detectors cannot distinguish between one and more than one detected photons. Due to these imperfections, the output state in a and b is not a pure state but a mixed entangled state. Assuming the single photon sources can generate single photons with probability p_r , it is easy to see that when there are 2 photons ($\{1, 2\}, \{1, 2'\}, \{1', 2\}, \{1', 2'\}$) with probability $p_r^2(1 - p_r)^2$, 3 photons ($\{1, 1', 2\}, \{1, 1', 2'\}, \{1, 2, 2'\}, \{1', 2, 2'\}$) with probability $p_r^3(1 - p_r)$ and 4 photons ($\{1, 1', 2', 2\}$) with probability p_r^4 emitted from single photon

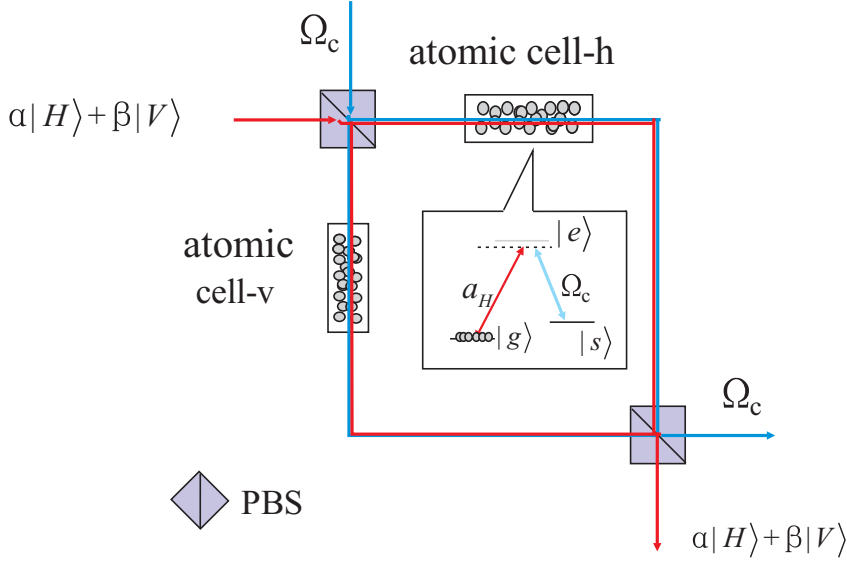


Figure 5.2: Quantum memory for photonic polarization qubits. Two ensembles are driven by a classical control field. Classical and quantized light fields are fed into the first PBS and will leave at two different outputs of the second PBS. As each atomic cell works as quantum memory for single photons with polarization $|H\rangle$ or $|V\rangle$ via the adiabatic transfer method, the whole setup is then quantum memory of any single-photon polarization states. The inset shows the relevant level structure of the atoms. The $|e\rangle - |s\rangle$ transition is coherently driven by the classical control field of Rabi frequency Ω_c , and the $|g\rangle - |e\rangle$ transition is coupled to a quantized light field.

sources, there will be a coincidence count between two of the detectors.

Considering all these possibilities, we find that if one of the four coincidence counts occurs, e.g., D_1 and D_4 is registered, the output state in a and b is equivalent to an effectively maximally entangled state

$$\rho_c = p_{2c}\rho_{2c} + p_{1c}\rho_{1c} + p_{0c}\rho_{0c}, \quad (5.1)$$

with the unnormalized coefficients

$$p_{2c}^{(u)} = \frac{p_r^4 \eta_d^2}{32}, \quad (5.2)$$

$$p_{1c}^{(u)} = \frac{p_r^3(1-p_r)\eta_d^2}{8} + \frac{p_r^4 \eta_d^2}{32} + \frac{p_r^4 \eta_d \eta_2}{64}, \quad (5.3)$$

$$p_{0c}^{(u)} = \frac{1}{32} [p_r^3(1-p_r)(2\eta_d^2 + \eta_d \eta_2) + p_r^4 \eta_d \eta_2 + 4p_r^2(1-p_r^2)\eta_d^2]. \quad (5.4)$$

Here ρ_{2c} is one of the maximally entangled Bell states, ρ_{1c} is the one-photon maximally mixed state and ρ_{0c} is the vacuum state, which indicates that all the input photons are

detected and there is no photon in the output a and b . The success probability for the event-ready entangler is $p_c = p_{2c}^{(u)} + p_{1c}^{(u)} + p_{0c}^{(u)}$.

After the event-ready mixed entangled state is successfully generated, it will be directed and stored into memory qubits at each communication node. Atomic ensembles can serve as a quantum memory to store a photonic state [75, 92]. By applying a time dependent classical control laser pulse of a Rabi frequency Ω_c , the whole system has a particular zero-energy eigenstate, i.e., the dark-state-polariton [63, 62]. The single-polariton state is $|D, 1\rangle = \frac{\Omega_c(t)}{\sqrt{\Omega_c^2(t) + g^2 N}} |1\rangle_p |0\rangle_a - \frac{g\sqrt{N}}{\sqrt{\Omega_c^2(t) + g^2 N}} |0\rangle_p S^\dagger |0\rangle_a$, with g being the coupling constant for the $|g\rangle - |e\rangle$ transition. Here $|0\rangle_p$ ($|1\rangle_p$) is the vacuum (single-photon) state of the quantized field to be stored. The quantum memory works by adiabatically changing $\Omega_c(t)$ such that one can coherently map $|D, 1\rangle$ onto either purely atom-like state $|0\rangle_p S^\dagger |0\rangle_a$ where the single photon is stored, or purely photon-like state $|1\rangle_p |0\rangle_a$, which corresponds to the release of the single photon.

To exploit the advantage of two-photon Hong-Ou-Mandel-type interference, we need a quantum memory for the photonic polarization qubits. Fig. 5.2 shows quantum memory for storing any single-photon polarization states by the dark-state-polariton method. Two atomic ensembles being a quantum memory for polarization qubits at each node are thus the required localized memory qubit in our scheme. Thus transformation between an arbitrary photon polarization state $\alpha |H\rangle + \beta |V\rangle$ and the corresponding state stored in atomic ensembles $(\alpha S_h^\dagger + \beta S_v^\dagger) |0\rangle$ can be achieved by adiabatically manipulating the control laser pulse. Importantly, our quantum memory works even when the two probability amplitudes in the stored state $\alpha |H\rangle + \beta |V\rangle$ are not c-numbers but quantum states of other photonic qubits. As a result, two memory qubits U and D at one site can be deterministically entangled in their ‘‘polarizations’’ by storing two polarization-entangled photons, e.g., $\frac{1}{\sqrt{2}}(S_{h_U}^\dagger S_{h_D}^\dagger + S_{v_U}^\dagger S_{v_D}^\dagger) |vac\rangle \leftrightarrow \frac{1}{\sqrt{2}}(|H\rangle |H\rangle + |V\rangle |V\rangle)$.

In the above protocol, four photons are emitted by the ensembles serving as sources, two of them are detected, two are absorbed again by the EIT memories. This double use of the memories (emission followed by storage) leads to relatively large errors (vacuum and single-photon contributions) in the created state if the memory efficiencies are smaller than one. These errors then have a negative impact on the success probabilities of the entanglement generation and swapping operations, and thus on the overall time needed for long-distance entanglement distribution.

Here we propose a different method for the local generation of high-fidelity entangled pairs of atomic excitations, which is based on the partial readout of ensemble memories. This scheme does not use any emission followed by storage. For the same memory and detection efficiency, it leads to higher quality entangled pairs compared to the method of Ref. [91], and as a consequence to a significantly improved rate for the overall quantum repeater protocol. We now describe the proposed method for local entanglement generation in detail.

The proposed setup uses four atomic ensembles. Atomic Raman transitions are coherently excited such that a Stokes photon can be emitted with a small probability χ . This Stokes photon has a well defined polarization: the horizontally (vertically) polarized modes are labelled by a_h^\dagger and b_h^\dagger (a_v^\dagger and b_v^\dagger), and are produced from upper (lower)

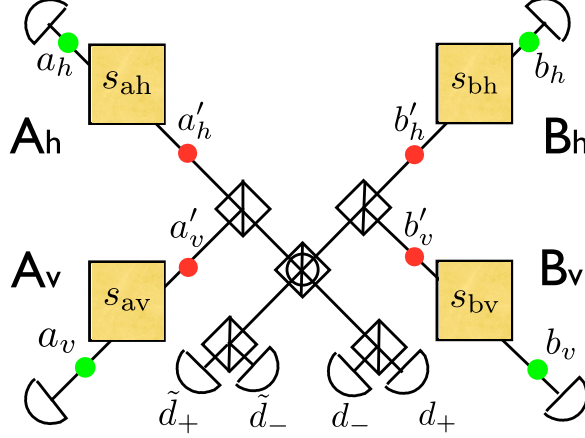


Figure 5.3: Setup for generating high-fidelity entangled pairs of atomic excitations. Yellow squares represent atomic ensembles which probabilistically emit Stokes photons (green dots). The conditional detection of a single Stokes photon heralds the storage of one atomic spin-wave excitation. In this way an atomic excitation is created and stored independently in each ensemble. Then all four ensembles are simultaneously read out partially, creating a probability amplitude to emit an anti-Stokes photon (red dots). The coincident detection of two photons in d_+ and \tilde{d}_+ projects non-destructively the atomic cells into the entangled state $|\Phi_{ab}\rangle$ of Eq. (5.5); $d_+-\tilde{d}_-$, $d_--\tilde{d}_+$, and $d_--\tilde{d}_-$ coincidences, combined with the appropriate one-qubit transformations, also collapse the state of the atomic cells into $|\Phi_{ab}\rangle$. Half-circles represent photon detectors. Vertical bars within squares label polarizing beam splitters (PBS) that transmit (reflect) H (V)-polarized photons. The central PBS with a circle performs the same action in the $\pm 45^\circ$ ($H + V/H - V$) basis.

atomic ensembles A_h and B_h (A_v and B_v) as represented in Fig. 5.2. The four atomic ensembles are repeatedly excited independently with a repetition rate r until a Stokes photon has been detected in each mode a_h^\dagger , a_v^\dagger , b_h^\dagger , and b_v^\dagger . The detection of a Stokes photon heralds the storage of a single atomic spin excitation in each ensemble, labelled by s_{ah}^\dagger , s_{av}^\dagger , s_{bh}^\dagger or s_{bv}^\dagger depending on the location. The average waiting time for successful charging of all four ensembles is approximately given by $T = \frac{1}{r\chi}(\frac{1}{4} + \frac{1}{3} + \frac{1}{2} + 1) = \frac{25}{12r\chi}$, with χ the excitation rate. Thanks to the independent creation and storage, it scales only like $1/\chi$. Once all ensembles are charged, the four stored spin-wave modes are then partially converted back into a photonic excitations. This is done using read pulses whose area is smaller than the standard value of π , such that the state of the system is given by $(\alpha a_h^\dagger + \beta s_{ah}^\dagger) \otimes (\alpha a_v^\dagger + \beta s_{av}^\dagger) \otimes (\alpha b_h^\dagger + \beta s_{bh}^\dagger) \otimes (\alpha b_v^\dagger + \beta s_{bv}^\dagger)|0\rangle$ with $|\alpha|^2 + |\beta|^2 = 1$. The primed modes a_h^\dagger , a_v^\dagger , (b_h^\dagger , b_v^\dagger) refer to the emitted anti-Stokes photons from memories located at A_h and A_v (B_h and B_v) respectively; $|0\rangle$ denotes the empty state. The released anti-Stokes photons are combined at a central station where they are detected in modes $d_\pm = a_h^\dagger + a_v^\dagger \pm b_h^\dagger \mp b_v^\dagger$ and $\tilde{d}_\pm = \pm a_h^\dagger \mp a_v^\dagger + b_h^\dagger + b_v^\dagger$, using the setup shown in Fig. 5.3. In the ideal case, a twofold coincident detection between d_+ and \tilde{d}_+ projects the state of the two remaining spin-wave modes non-destructively onto

$$|\Phi_{ab}\rangle = 1/\sqrt{2}(s_{ah}^\dagger s_{bh}^\dagger + s_{av}^\dagger s_{bv}^\dagger)|0\rangle. \quad (5.5)$$

The stored atomic excitations can be reconverted into photons as desired. In the proposed

quantum repeater protocol, one excitation (e.g. the one in the B ensembles) is reconverted into a photon right away and used for entanglement generation. The other excitation is reconverted later for entanglement swapping or for the final use of the entanglement. Note that the setup can also be used as a heralded source of single photon pairs [91, 93, 94].

Given an initial state where all four memories are charged, the probability for a coincidence between d_+ and \tilde{d}_+ is given by $\frac{1}{2}\alpha^4\beta^4$. Since the twofold coincidences $d_+-\tilde{d}_-$, $d_--\tilde{d}_+$, $d_--\tilde{d}_-$ combined with the appropriate one-qubit transformation also collapse the state of the atomic ensembles into $|\Phi_{ab}\rangle$, the overall success probability for the entangled pair preparation is given by $P_s = 2\alpha^4\beta^4$.

We now analyze the effect of non-unit detector efficiency η_d and memory recall efficiency η_r . The waiting time for the memories to be charged is now $T^\eta = T/\eta_d = \frac{25}{12r\chi\eta_d}$. Furthermore, the detectors can now give the expected coincidences when three or four anti-Stokes photons are released by the memories, but only two are detected. In this case, the created state contains additional terms including single spin-wave modes and a vacuum component,

$$\begin{aligned} \rho_{ab}^s &= c_2^s |\Phi_{ab}\rangle \langle \Phi_{ab}| \\ &+ c_1^s \left(|s_{ah}\rangle \langle s_{ah}| + |s_{av}\rangle \langle s_{av}| + |s_{bh}\rangle \langle s_{bh}| + |s_{bv}\rangle \langle s_{bv}| \right) \\ &+ c_0^s |0\rangle \langle 0|; \end{aligned} \quad (5.6)$$

where $c_2^s = 2\alpha^4\beta^4\eta^2/P_s^\eta$, $c_1^s = \alpha^6\beta^2\eta^2(1-\eta)/P_s^\eta$ and $c_0^s = 2\alpha^8(1-\eta)^2\eta^2/P_s^\eta$. Here $\eta = \eta_r\eta_d$ is the product of the memory recall efficiency and the (photon-number resolving) detector efficiency, and we have introduced a superscript s for ‘‘source’’. The probability for the successful preparation of this mixed state is $P_s^\eta = 2\eta^2\alpha^4(1-\alpha^2\eta)^2$. The fidelity of the conditionally prepared state is equal to the two-photon component $c_2^s = \beta^4/(1-\alpha^2\eta)^2$. As can be seen from the two previous equations, there is a tradeoff on the readout coefficients α, β . The creation of an entangled state with a high fidelity favors $\alpha \approx 0$, whereas a high success probability favors $\alpha \approx \beta \approx 1/\sqrt{2}$.

5.3 Repeater Protocol

We now include our source of heralded pairs within a quantum repeater protocol. Fig. 5.4A shows how entanglement between two remote sources (denoted AB and CD) is created by combining two anti-Stokes photons at a central station, where one photon is released from the B ensembles and the other from the C ensembles, and performing a projective measurement into the modes $D_\pm^{bc} = b'_h \pm c'_v$ and $D_\pm^{cb} = c'_h \pm b'_v$ using two-photon interference. The twofold coincident detection $D_+^{bc}-D_+^{cb}$ ($D_+^{bc}-D_-^{cb}$, $D_-^{bc}-D_+^{cb}$, or $D_-^{bc}-D_-^{cb}$ combined with the appropriate one-qubit operations) collapses the two remaining full memories into $|\Phi_{ad}\rangle$. Due to imperfections, the distributed state ρ_{ad}^0 includes vacuum and single spin-wave modes. One can show that their weights c_2^0, c_1^0, c_0^0 are unchanged compared with the weights of the source state ρ_{ab}^s , because $c_2^0 = \frac{(c_2^s)^2}{(c_2^s+2c_1^s)^2} = c_2^s$, $c_1^0 = \frac{c_1^s c_2^s}{(c_2^s+2c_1^s)^2} = c_1^s$ and $c_0^0 = \frac{4(c_1^s)^2}{(c_2^s+2c_1^s)^2} = c_0^s$. (The condition for having a stationary state is $c_0 c_2 = 4(c_1)^2$, which is fulfilled by c_2^s, c_1^s, c_0^s .) The success probability for the entanglement creation is given by $P_0 = 2\eta^2\eta_t^2 (c_2^s/2 + c_1^s)^2$.

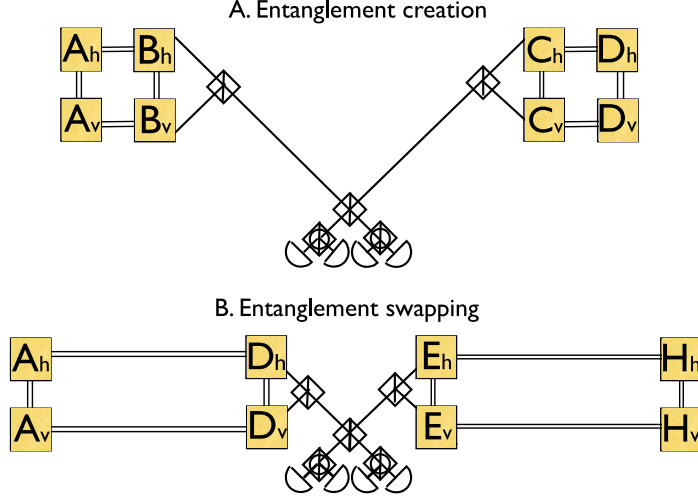


Figure 5.4: (A) Long-distance entanglement creation using two four-ensemble sources as shown in Fig. 5.3. The A and D ensembles are entangled by the detection of two photons emitted from the B and C ensembles, using the same setup as in chapter 4. Note that the AB source is separated from the CD source by a long distance. (B) Entanglement swapping. The same set of linear optical elements allows one to entangle the A and H ensembles belonging to two adjacent elementary links. Note that the D and E ensembles are at the same location.

Here η_t is the fiber transmission for each photon.

Fig. 5.4B shows how, using the same combination of linear optical elements and detectors, one can perform successive entanglement swapping operations, such that the state ρ_{az}^n is distributed between the distant locations A and Z after n swapping operations. In analogy to above, one can show that the distributed state ρ_{az}^n includes vacuum and single spin-wave components with unchanged weights with respect to the initial ones, i.e. $c_2^n = c_2^s$, $c_1^n = c_1^s$ and $c_0^n = c_0^s$. From the expression of P_0 and keeping in mind that the entanglement swapping operations are performed locally such that there are no transmission losses, one deduces the success probability for the i -th swapping, $P_i = 2\eta^2 (c_2^s/2 + c_1^s)^2$. The two-spin-wave component of the distributed mixed state $|\Phi_{az}\rangle$ is finally post-selected with the probability $P_{pr} = c_2^s \eta^2$.

The time required for a successful distribution of an entangled state $|\Phi_{az}\rangle$ is approximately given by

$$T_{\text{tot}} = \left(\frac{3}{2}\right)^{n+1} \frac{L_0}{c} \frac{1}{P_0 P_1 \dots P_n P_{\text{pr}}}, \quad (5.7)$$

where $L_0 = L/2^n$ is the length of an elementary link, L is the total distance and n is the nesting level of the repeater. Taking into account the expressions of P_0 , P_i (with $i \geq 1$) and P_{pr} , one can rewrite T_{tot} as

$$T_{\text{tot}} = 4 \times 3^{n-1} \times \frac{L_0}{c} \frac{(1 - \alpha^2 \eta)^{2(n+2)}}{\eta_t^2 \eta^{2(n+2)} \beta^{4(n+2)}}. \quad (5.8)$$

Here $\eta_t = e^{-L_0/(2L_{\text{att}})}$ is the fiber transmission, with the attenuation length L_{att} . In our numerical examples we use $L_{\text{att}} = 22$ km, corresponding to losses of 0.2 dB/km, which are

currently achievable at a wavelength of $1.5 \mu\text{m}$.

For these formulas to be strictly valid, the source preparation time has to be negligible compared to the communication time, i.e. in our case $T_s = \frac{3T_s^\eta}{2P_s^\eta} \ll \frac{L_0}{c}$. Otherwise one simply has to replace $\frac{L_0}{c}$ by $\frac{L_0}{c} + T_s$.

We calculate the total time needed to create an entangled pair over a distance from 400 km to 1200 km for all the different protocols using only atomic ensembles and linear optics. The results are shown in Fig. 5.5.

The quantity shown is the average time needed to distribute a single entangled pair for the given distance. Curve A shows the time required using direct transmission of photons through optical fibers, with losses of 0.2 dB/km, corresponding to the best available telecom fibers at a wavelength of $1.5 \mu\text{m}$, and a pair generation rate of 10 GHz. Curve B shows the performance of the original DLCZ protocol using single-photon detection for both entanglement generation and entanglement swapping. As we discussed in chapter 3, the distribution rate of DLCZ protocol is extremely low. Curve C is the protocol of Ref. [90] that uses quasi-ideal single photon sources (which can be implemented with atomic ensembles) plus single-photon detections for generation and swapping. Curve D shows the protocol of locally generating high-fidelity entangled pairs using single-photon sources and two-photon detections for entanglement generation and swapping. The performance of the improved protocol is shown as curve E. For the new protocol, the gain in time overhead clearly outweighs the modest increase in complexity compared to the fastest single-photon protocol. For instance, for a communication distance of about 1000 km the new protocol uses four times as many memories as Ref. [90], but it is about 18 times faster. The rate improvement compared to the DLCZ protocol, which uses the same number of memories, is by a factor of 300. It is thus not only robust, but also the most efficient repeater protocol known to us for the given ingredients.

We then consider the role of errors due to the creation of two excitations in a single memory. Note that in the local entanglement generation process of Fig. 5.3 a large part of such multi-photon events will be detected because both Stokes and anti-Stokes photons are detected locally and thus potentially with high efficiency. We find by explicit calculation that the fidelity of the distributed state at the first order in χ after $n = 4$ swapping levels (neglecting other errors) is given by

$$F \approx 1 - [(418 - 260\eta) + (47 - 205\eta)\alpha^2] (1 - \eta_d)\chi.$$

If one wants a fidelity of the final state $F = 0.9$, one can choose e.g. $\alpha^2 = 0.2$ and $\chi = 6 \times 10^{-3}$. This is the value of α used in Fig. 5.5. For these values, equality between the source preparation time T_s and the communication time L_0/c (e.g. for $L = 1000$ km and 16 links) is reached for a basic repetition rate r of order 60 MHz.

5.4 Implementation

In this section we discuss potential experimental implementations of the proposed protocol. There has recently been impressive progress on the efficiency of conversion from atomic excitation to photon, which sets the fundamental limit for the memory efficiency. Values

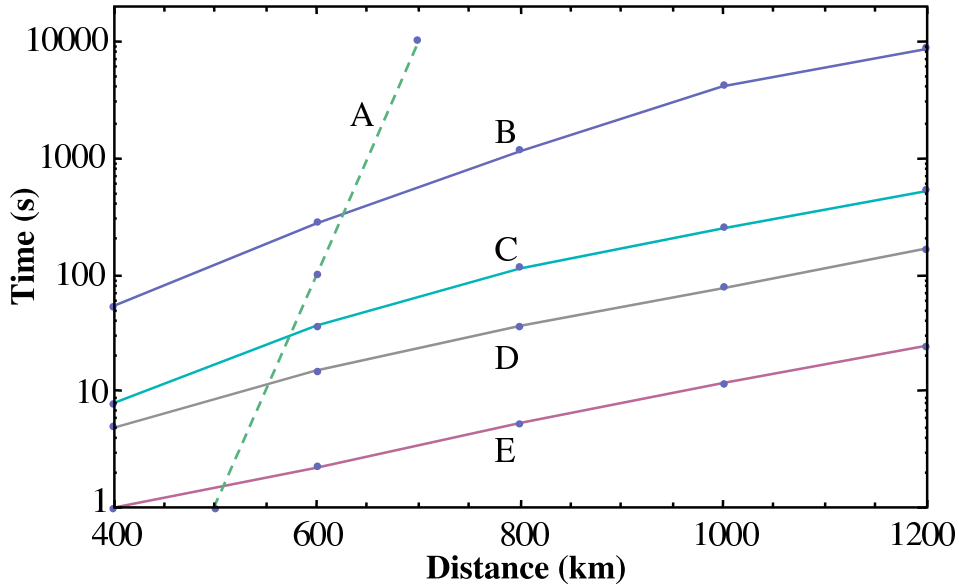


Figure 5.5: Comparison of different quantum repeater protocols that all use only atomic ensembles and linear optics. The quantity shown is the average time needed to distribute a single entangled pair for the given distance. A: as a reference, the time required using direct transmission of photons through optical fibers, with losses of 0.2 dB/km, corresponding to the best available telecom fibers at a wavelength of $1.5 \mu\text{m}$, and a pair generation rate of 10 GHz. B: the original DLCZ protocol that uses single-photon detections for both entanglement generation and swapping. C: The protocol that uses quasi-ideal single photon sources (which can be implemented with atomic ensembles, cf. text) plus single-photon detections for generation and swapping. D: The protocol that locally generates high-fidelity entangled pairs by using four single photons. E: the proposed new protocol which uses an improved method of partial retrieval to generate local entanglement. For all the curves we have assumed memory and detector efficiencies of 90%. The numbers of links in the repeater chain are optimized for curves B and C, e.g. giving 4 links for 600 km and 8 links for 1000 km for both protocols. For curves D and E, we imposed a maximum number of 16 links (cf. text), which is used for all distances greater than 400 km.

as high as 84 percent have been achieved with a cavity setup.

Current DLCZ-type experimental setups with atomic gases are very well suited for demonstrating the proposed ideas. Current repetition rates r in DLCZ-type experiments are of order a few MHz. To fully exploit the potential of the proposed protocol, the rates have to be increased, cf. above. Rates of tens of MHz, which could already bring the overall entanglement generation times to within a factor of 2 or 3 of the values given in Fig. 5.5, are compatible with typical atomic lifetimes. With atomic gases, further improvements in r could be achieved using the Purcell effect in high-finesse cavities to increase the atomic lifetimes.

Ref. [68] pointed out that the combination of a photon pair source and of a quantum memory which stores one of the photons is equivalent to a DLCZ-type atomic ensemble, which emits a photon that is correlated with an atomic excitation. This approach may make it possible to achieve even higher values of r , using e.g. photon pair sources based on parametric down-conversion and solid-state quantum memories based on controlled reversible inhomogeneous broadening [95, 96, 97, 98]. Solid-state atomic ensembles, e.g. rare-earth ion doped crystals, furthermore hold the promise of allowing very long storage times (which are essential for quantum repeaters), since the storage time is no longer limited by atomic motion, while the intrinsic atomic coherence times can be very high. For example, hyperfine coherence times as long as 30 s have been demonstrated in Pr:Y₂SiO₅ [99]. The best efficiency published so far for a CRIB memory (in the same material) is 15% [100], but experiments are progressing quite rapidly. This approach furthermore holds the promise of allowing temporal multiplexing, leading to a potential further improvement in the entanglement creation rate, provided that multi-mode memories with the required characteristics can be realized. The main requirements are sufficient optical depth and sufficient memory bandwidth. Other forms of multiplexing could also be possible and might allow to relax the requirements on the memory storage times [101]. Ideally the memories in the described protocol should operate at the optimal wavelength for telecom fibers, i.e. at 1.5 μm . This may be possible with Erbium-doped crystals [102, 103]. Alternatively, wavelength conversion techniques could be employed [104].

Good photon detectors with photon number resolution are also essential. Superconducting transition-edge sensor detectors can already resolve telecom-wavelength photons of 4 ns duration at a repetition rate of 50 kHz, with an efficiency of 0.88 and negligible noise [105, 106]. In the long run, NbN detectors are promising for achieving higher rates. The detection of 100 ps photons with 100 MHz rate has been reported in Ref. [107] with an efficiency of 0.56 and a noise smaller than 10/s.

Our results show the great interest for quantum repeaters of locally generating entangled pairs of excitations with high fidelity. This could also be achieved for physical systems other than atomic ensembles. Promising approaches include the creation of atom-photon entanglement [108, 109] and entangled photon pair sources based on quantum dots [110, 111], which could be combined with quantum memories.

In this chapter, we quantitatively compare the scalability of all the quantum repeater protocols using only atomic ensembles and linear optics. This comparison showed that protocols based on the local generation of high-fidelity entangled pairs of atomic excita-

tions make it possible to combine robustness with respect to phase fluctuations and good entanglement distribution rates. We show that a new approach for local entanglement generation based on partial memory readout, together with the use of two-photon detections for long-distance entanglement generation and for entanglement swapping, will lead to a repeater protocol that, as far as we know, achieves the highest entanglement distribution rate with the given ingredients. First demonstration experiments should be possible with atomic gases. The protocol could reach its full potential combining fast photon pair sources such as parametric down-conversion and solid-state quantum memories.

Chapter 6

Deterministic single-photon source based on a quantum memory

In this chapter, we propose and experimentally demonstrate a deterministic single-photon source by the aid of feedback circuit. A single collective excitation, imprinted in an atomic ensemble via spontaneous Raman scattering, is retrieved out on demand as a single photon at a predetermined time. It is shown that the production rate of single photons can be enhanced significantly by a feedback circuit. Such a deterministic single-photon source is well suited for future large-scale linear optical quantum computation and quantum cryptography.

6.1 Introduction

Although weak coherent beams can be used as a pseudo single-photon source, a genuine single-photon source is crucial in secure quantum key distribution and scalable quantum computation [112]. The single-photon nature guarantees unconditional security and high efficiency in quantum cryptography [6]. The Knill-Lamme-Milburn scheme and other improved linear optical quantum computation protocols also rely on the availability of such on demand single-photon sources [18, 20, 21, 113]. In recent years, different quantum systems have been exploited to realize an on-demand single-photon source, such as quantum dots [114, 115, 116], single atoms and ions [117, 118, 119], and color centers [120]. However, all of them are confronted with different challenges. For instance, the single-atom implementation provides spectrally narrow single photons with a well defined spatial mode, but it needs strong coupling between atoms and photons, and thus requires sophisticated techniques and expensive setups. Quantum dots are a potential source with high single-photon rate, but the requirement of spectral filtering entails inevitable losses, which make the single-photon source probabilistic. Besides, it is very difficult to prepare truly identical sources due to inhomogeneities in both the environment of the emitters and the emitters itself [116]. Color centers are excellent sources, even at room temperature, however, the

high peak intensities of a pulsed excitation can lead to complex and uncontrollable dark states. So it has been taken as a formidable task to develop a promising deterministic single-photon source.

Moreover, a challenging task in quantum information processing is the controllable transfer of quantum state between a flying qubit and a quantum memory. Starting from a recent proposal for long-distance quantum communication with atomic ensembles and linear optics [42], it is possible to implement both a single-photon source on demand and controllable transfer of quantum state between a photonic qubit and a collective excited state of an atomic ensemble. As we introduced in chapter 2, a single spin excitation can be generated probabilistically in an atomic ensemble by applying a classical write pulses via spontaneous Raman scattering. The successful generation of a spin excitation is indicated by the detection of a corresponding Raman photon. With the help of a feedback circuit, a series of subsequent clean and write pulses is applied until an excitation is imprinted in the atomic ensemble. In this way, a collective excitation is deterministically stored in the atomic ensemble if sufficient trials are applied. The spin excitation can then be converted into a photon for further application when necessary. Such a sequence can be taken as having a feed-forward ability for the deterministically converted single photon.

Recent years witnessed the significant experimental progresses in demonstration of quantum storage, single-photon sources, and entanglement generation between two atomic ensembles [121]. However, these experiments all rely on the coincidence-based post-selection. No feedback was applied and consequently the requirement of resources would increase exponentially with each new step of operation. This significantly limits the scalability of the schemes.

In this chapter, we propose and experimentally demonstrate a deterministic and storable single-photon source. Single collective excitations in an atomic ensemble are created by detecting anti-Stokes photons generated due to spontaneous Raman scattering. This detection allows to implement a feed-forward circuit and convert the spin excitations into single photons at a predetermined time. It is shown that the single-photon quality is conserved while the production rate of single photons can be enhanced considerably by the aid of the feedback circuit. The spatial mode, bandwidth, and frequency of single-photon pulses are determined by the mode match condition, intensity and frequency of the retrieval light. Our controllable deterministic single-photon source potentially paves the way for the construction of scalable quantum communication networks and linear optical quantum computation.

6.2 Basic protocol

The nonclassical correlation between anti-Stokes and Stokes photon pair allows us to prepare a heralded single-photon source. The basic idea is that a single photon can be generated on demand if we know there is a collective excitation in the atomic ensemble. The presence of the latter is heralded by the detection of a scattered photon in the write process. After that one simply waits and converts the excitation into a photon at a predetermined time. The performance of heralding measurements represents a conditional

process. Assume we have generated the two-mode squeezed state

$$|\psi\rangle = |0_a\rangle|0_{AS}\rangle + \sqrt{\chi}|1_a\rangle|1_{AS}\rangle + \chi|2_a\rangle|2_{AS}\rangle \quad (6.1)$$

between the atomic collective state and the anti-Stokes field. Note that in our experiments, we can use either the anti-Stokes photon or the Stokes photon as the idler. The collective state will be projected into a mixed state

$$\rho_a = |1\rangle_a\langle 1| + 2\chi|2\rangle_a\langle 2|, \quad (6.2)$$

conditioned on a click in the anti-Stokes channel, where the noise term that the atomic ensemble has two excitations is proportional to the excitation probability. To get a single photon of high quality, we have to work with small excitation probability $\chi \ll 1$. The experimental setup to create the heralded single photon source is depicted in Fig 6.1a. The anti-Stokes photon is registered by single photon detector D1, and the retrieved Stokes photon is registered by detectors D2 and D3. The quality of the single-photon source is determined by the anti-correlation function [122]

$$\alpha = \frac{p_{23|1}}{p_{2|1}p_{3|1}} = \frac{p_1 p_{123}}{p_{12} p_{13}}, \quad (6.3)$$

with $p_{m|1}$ ($m = 2, 3, 23$) the probability to detect photons in channel m conditional on a click in channel 1. The probabilities can be estimated by

$$p_1 = \chi\eta_{AS}, \quad (6.4)$$

$$p_{12} = p_{13} = \chi\gamma\eta_S\eta_{AS}/2, \quad (6.5)$$

$$p_{123} = \chi^2\gamma^2\eta_S^2\eta_{AS}, \quad (6.6)$$

with the retrieval efficiency γ , and η_S , η_{AS} the detection efficiency in Stokes channel and anti-Stokes channel respectively. Plugging these equations into Eq. (6.3), we obtain the anti-correlation function

$$\alpha = 4\chi \ll 1. \quad (6.7)$$

For coherent light we have $\alpha_c = 1$.

To improve the production rate, we can apply more write pulses in each experimental trial, and a feedback protocol. In this way, we can greatly increase the generation probability of the single photons while the single-photon quality is conserved. To do so, as shown in Fig. 6.1(b), in the time interval ΔT , N independent write sequences with a period of δt_w are applied to the atomic ensemble. Each write sequence contains a cleaning pulse (the optical pumping to the initial state) and a write pulse. Once an anti-Stokes photon is detected by D1, the feedback circuit stops the further write sequences and enables the read pulse to retrieve the single Stokes photon after a time delay Δt . The maximum number of trials (N) is determined by the life time of the excitation. The feedback protocol enhances the production rate of Stokes photons according to the new excitation probability

$$P_{tot} = \sum_{j=0}^{N-1} p_1(1-p_1)^j. \quad (6.8)$$

The conditional probability is

$$P_{23|1} = \sum_{j=0}^{N-1} \frac{p_1(1-p_1)^j}{p_{tot}} p_{23|1}(\Delta T - j\delta t_w), \quad (6.9)$$

$$P_{2|1} = \sum_{j=0}^{N-1} \frac{p_1(1-p_1)^j}{p_{tot}} p_{2|1}(\Delta T - j\delta t_w), \quad (6.10)$$

$$P_{3|1} = \sum_{j=0}^{N-1} \frac{p_1(1-p_1)^j}{p_{tot}} p_{3|1}(\Delta T - j\delta t_w), \quad (6.11)$$

where the time dependent probability is

$$p_{23|1}(\Delta T - j\delta t_w) = \chi \eta_s^2 \gamma^2 (\Delta T - j\delta t_w), \quad (6.12)$$

$$p_{2|1}(\Delta T - j\delta t_w) = \frac{1}{2} \eta_s \gamma (\Delta T - j\delta t_w), \quad (6.13)$$

$$p_{3|1}(\Delta T - j\delta t_w) = \frac{1}{2} \eta_s \gamma (\Delta T - j\delta t_w), \quad (6.14)$$

with the retrieval efficiency a time dependent function. In this case, the anti-correlation function is given by

$$\alpha = \frac{P_{23|1}}{P_{2|1}P_{3|1}}. \quad (6.15)$$

One can see if the retrieval efficiency is constant, the single photon quality is always conserved. Our protocol can be executed in different modes. In a first mode, one can fix the retrieve time ΔT . Therefore, the delay Δt varies because the spin excitation is created randomly by one of the write sequences. Single photons are produced at a given time with a high probability, ideally approaching unity if $N \gg 1$. Furthermore, the retrieve efficiency could be improved significantly by an increased optical depth of the atomic ensemble and an optimal retrieval protocol [82]. This mode serves as a deterministic single-photon source. In a second mode, we retrieve the single photon with a fixed delay Δt after a successful write. More general, the imprinted single excitation can be converted into a single photon at any given time with the life time τ_c . This is well suited for a quantum repeater where one needs to synchronize the nodes.

6.3 Experiment

The basic concept of our experiments is shown in Fig. 6.1. Cold atoms with Λ -type level configuration (two ground state $|a\rangle$, $|b\rangle$ and an excited state $|e\rangle$) collected by a magneto-optical trap (MOT) are used as the media for quantum memory. The atoms are initially optically pumped to state $|a\rangle$ by a pump laser. Then a weak classical write pulse, with the Rabi frequency Ω_w , close to the resonance of transition $|a\rangle$ to $|e\rangle$ is introduced in the atomic cloud. Due to the spontaneous Raman process, a photon of anti-Stokes field \hat{a}_{AS} is emitted into the forward scattering mode. Simultaneously, a collective spin excitation corresponding to the mode of the anti-Stokes field \hat{a}_{AS} is generated in the atomic ensemble. The state of the field \hat{a}_{AS} and the collective spin state of the atoms can be expressed by

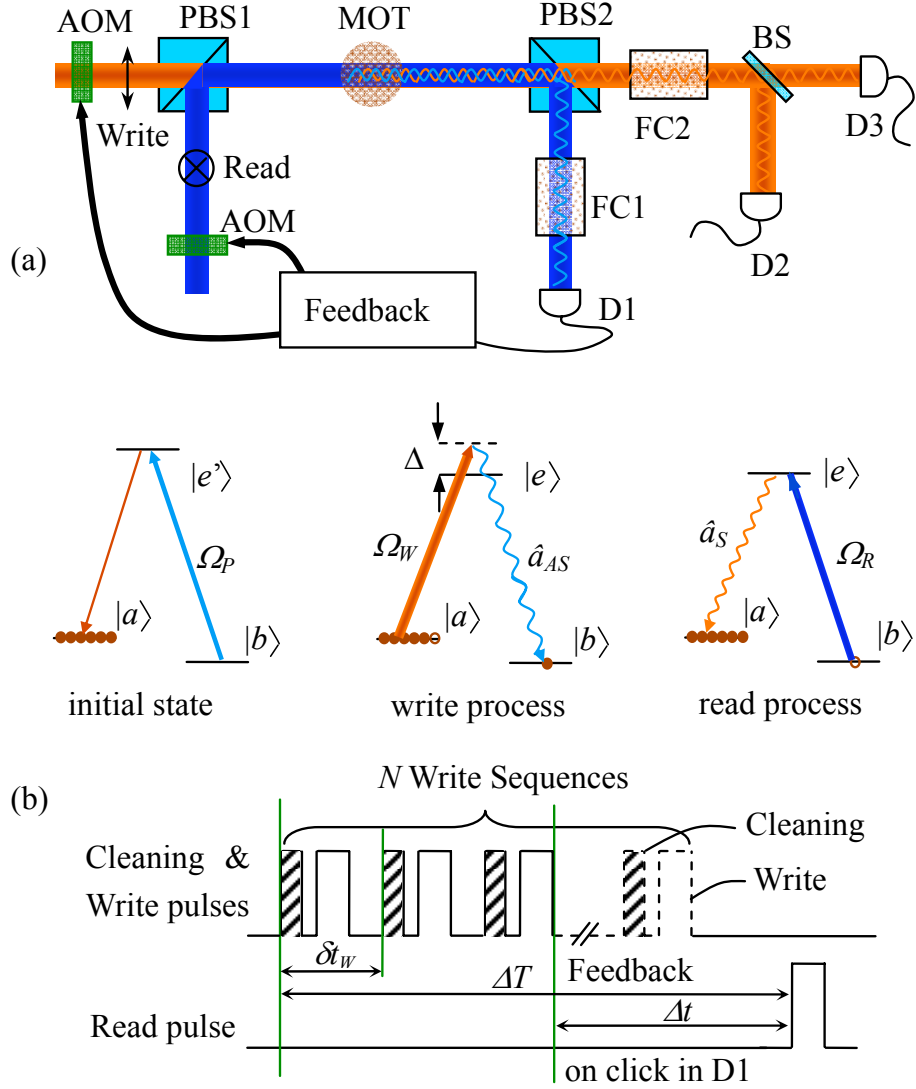


Figure 6.1: (a) Illustration of the experimental setup and (b) the time sequence with the feedback circuit for the write and read process. The atomic ensemble is firstly prepared in the initial state $|a\rangle$ by applying a pump beam resonant with the transition $|b\rangle$ to $|e'\rangle$. A write pulse with the Rabi frequency Ω_w is applied to generate the spin excitation and an accompanying photon of the mode \hat{a}_{AS} . Waiting for a duration Δt , a read pulse is applied with orthogonal polarization and spatially overlap with the write beam in PBS1. The photons, whose polarization is orthogonal to that of the write beam, in the mode \hat{a}_{AS} are spatially extracted from the write beam by PBS2 and detected by detector D1. Similarly, the field \hat{a}_S is spatially extracted from the Read beam and detected by detector D2 (or D3). Here, FC1 and FC2 are two filter cells, BS is a 50/50 beamsplitter, and AOM1 and AOM2 are two acousto-optic modulators.

the superposed state

$$|\Psi\rangle \sim |0_{AS}0_a\rangle + \sqrt{\chi}|1_{AS}1_a\rangle + \chi|2_{AS}2_a\rangle + O(\chi^{3/2}), \quad (6.16)$$

where χ is the excitation probability of one spin flip, $|i_{AS}i_a\rangle$ denotes the i -fold excitation of the anti-Stokes field and the collective spin. Ideally, conditioned on detecting one and only one anti-Stokes photon in detector D1, a single spin excitation is generated in the atomic ensemble with certainty. After a controllable time delay δt (in the order of the lifetime τ_c of the spin excitation), another classical read pulse with the Rabi frequency Ω_r , which is on-resonance with the transition from $|b\rangle$ to $|e\rangle$, is applied to convert the spin excitation into a photon of Stokes field \hat{a}_S .

In our present experiment, more than 10^8 ^{87}Rb atoms are collected by the MOT with an optical depth of about 5 and the temperature of about 100 μK . The earth magnetic field is compensated by three pairs of Helmholtz coils. The two ground states $|a\rangle$ and $|b\rangle$ and the excited state $|e\rangle$ in the Λ -type system are $|5S_{1/2}, F=2\rangle$, $|5S_{1/2}, F=1\rangle$, and $|5P_{1/2}, F=2\rangle$ [123], respectively. The write laser is tuned to the transition from $|5S_{1/2}, F=2\rangle$ to $|5P_{1/2}, F=2\rangle$ with detuning of 10 MHz and the read laser is locked on resonance to the transition from $|5S_{1/2}, F=1\rangle$ to $|5P_{1/2}, F=2\rangle$. By using orthogonal polarizations, write and read beams are spatially overlapped on a polarized beam splitter (PBS1), and then focused into the cold atoms with the beam waist of 35 μm . After passing the atomic cloud, the two beams are split by PBS2 which serves as the first stage of filtering the write (read) beam out from the anti-Stokes (Stokes) field. The leakage of write (read) field from PBS2 propagating with the anti-Stokes (Stokes) field will be further filtered by a thermal cell filled with ^{87}Rb atoms, in which the rubidium atoms are prepared in state $|5S_{1/2}, F=2\rangle$ ($|5S_{1/2}, F=1\rangle$) initially. Coincident measurements among D1, D2 and D3 are performed with a time resolution of 2 ns.

After switching off the MOT, the atoms are optically pumped to the initial state $|a\rangle$. The write pulse containing about 10^4 photons with a duration of 100 ns is applied onto the atomic ensemble, to induce the spontaneous Raman scattering via $|a\rangle \rightarrow |e\rangle \rightarrow |b\rangle$. The superposition state of the induced anti-Stokes field and the collective spin is generated with a probability $\chi \ll 1$. After a controllable delay of δt , the read pulse with the duration of 75 ns is applied for converting the collective excitation into the Stokes field. In comparison, the intensity of the read pulse is about 100 times stronger than that of the write one.

Assume the probability to have an anti-Stokes (Stokes) photon is p_{AS} (p_S), and the coincident probability between the Stokes and anti-Stokes channels is $p_{AS,S}$, then the intensity correlation function $g_{AS,S}^{(2)} = p_{AS,S}/(p_{AS}p_S)$ [124]. We measured the variation of $g_{AS,S}^{(2)}$ as a function of p_{AS} shown in Fig. 6.2(a) with a time delay of $\delta t = 500$ ns. Considering the background in each channel, we obtain

$$p_{AS} = \chi\eta_{AS} + B\eta_{AS}, \quad (6.17a)$$

$$p_S = \chi\gamma\eta_S + C\eta_S, \quad (6.17b)$$

$$p_{AS,S} = \chi\gamma\eta_{AS}\eta_S + p_{AS}p_S. \quad (6.17c)$$

Here, η_{AS} and η_S are the overall detection efficiencies in the anti-Stokes and Stokes channels

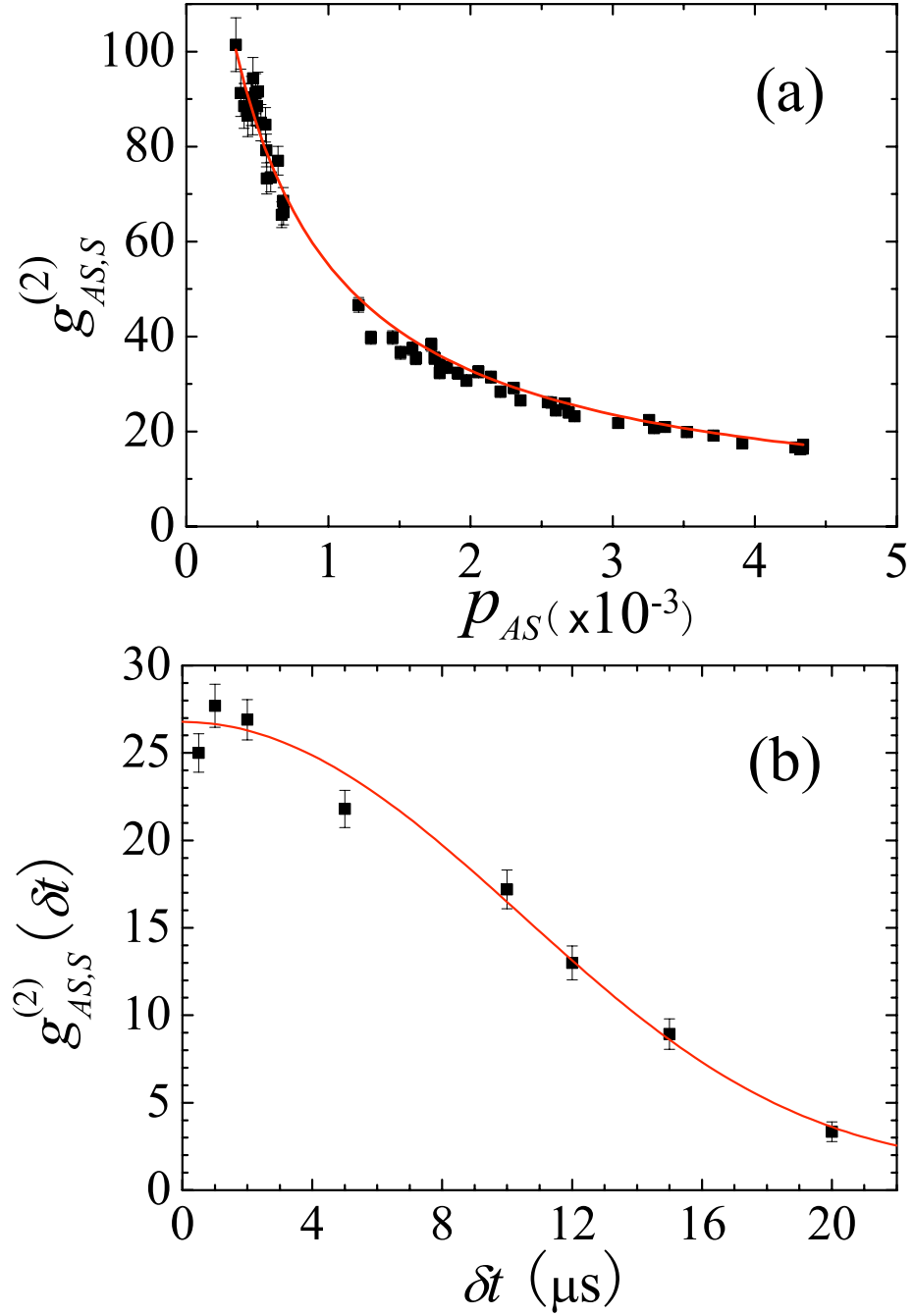


Figure 6.2: Intensity correlation function $g_{AS,S}^{(2)}$ along the excitation probability p_{AS} with $\delta t = 500$ ns (a) and along the time delay δt between read and write pulses with $p_{AS} = 3 \times 10^{-3}$ (b). The black dots are obtained from current experiment and the curves correspond to a least-square fit procedure according to Eq. (6.18). The observed lifetime is $\tau_c = 12.5 \pm 2.6 \mu s$.

respectively, including the transmission efficiency η_t of filters and optical components, the coupling efficiency η_c of the fiber couplers, and the quantum efficiency η_q of single photon detectors (η_{AS} includes an additional spatial mode-match efficiency), γ is the retrieve efficiency which is a time-dependent factor, and B (C) is determined by the background in the anti-Stokes (Stokes) channel. The red curve in Fig. 6.2(a) is the least-square fit result according to Eq. (6.17), assuming $B = 0$ for simplicity. The efficiency in the anti-Stokes channel is observed as $\eta_{AS} \sim 0.07$ and the retrieve efficiency $\gamma \sim 0.3$. The largest correlation $g_{AS,S}^{(2)}$ (101 ± 6) appears at the lowest excitation probability p_{AS} of 3.5×10^{-4} . Note that the background noise in the Stokes channel is proportional to the excitation probability, while here for simplicity we assume it is a constant.

The finite lifetime of the collective spin excitation results from the dephasing of the collective state due to the Larmor precession of the spins in the residual magnetic field. It can be characterized by the decay of the retrieve efficiency $\gamma(\delta t) = \gamma_0 \exp(-\delta t^2/\tau_c^2)$, where τ_c is the lifetime of the collective state. In experiment, it is determined from the decay of the measured intensity correlation function $g_{AS,S}^{(2)}(\delta t)$ as shown in Fig. 6.2(b), taken at $p_{AS} = 0.003$. Using Eq. (6.17), the intensity correlation function reads

$$g_{AS,S}^{(2)}(\delta t) = 1 + \frac{\gamma(\delta t)}{(B + \chi)\gamma(\delta t) + D}, \quad (6.18)$$

where C is absorbed by the new constant D . Our results give a lifetime of $\tau_c = 12.5 \pm 2.6$ μs . The cross correlation of the first point is slightly lower which might be caused by noise arising from the elastic scattering of the write beam.

In the first experiment, we fixed $\Delta T = 12.5$ μs and $\delta t_w = 1$ μs , and $N = 12$ subsequent write sequences were applied. The quality of the single-photon source can be characterized by the anti-correlation parameter α as we discussed in last section, which is equivalent to the second-order auto-correlation function $g_{S,S}^{(2)}$ of the Stokes photon on the condition of an anti-Stokes photon is detected. When we use N write pulses and the feedback protocol, the detection probabilities in D2, D3 and the coincidence detection probability D23 conditioned on a registration of an anti-Stokes photon in D1 are

$$P_{m|AS} = \frac{\sum_{i=0}^{N-1} p_{AS}(1-p_{AS})^i p_{m|AS}(\Delta T - i \cdot \delta t_w)}{\sum_{i=0}^{N-1} p_{AS}(1-p_{AS})^i}, \quad (6.19)$$

where $m = 2, 3, 23$ and $p_{m|AS}(\Delta T - i \cdot \delta t_w)$ is a time-dependent probability conditioned on a click in the anti-Stokes channel. The anti-correlation parameter α is given by $P_{23|AS}/(P_{2|AS}P_{3|AS})$.

Fig. 6.3(a) shows the measured α as a function of the excitation probability p_{AS} . For $N = 1$ (black) the variation of α is nearly linear in the region of $p_{AS} = 0 \sim 0.006$. The black curve is the fit according to Eq. (6.17). When using 12 successive write sequences, we plot α versus $12p_{AS}$ as red dots. The red line is a no free parameter calculation from the above equations, taking the fitted parameters from $N = 1$ setting $N = 12$. We note that, for $p_{AS} \rightarrow 0$ the value of α is 0.057 ± 0.028 , which in principle should be 0. This offset comes from noise including residual leakage of the write and read beams, stray light, and dark counts of the detectors. However, the advantage of the feedback protocol is not

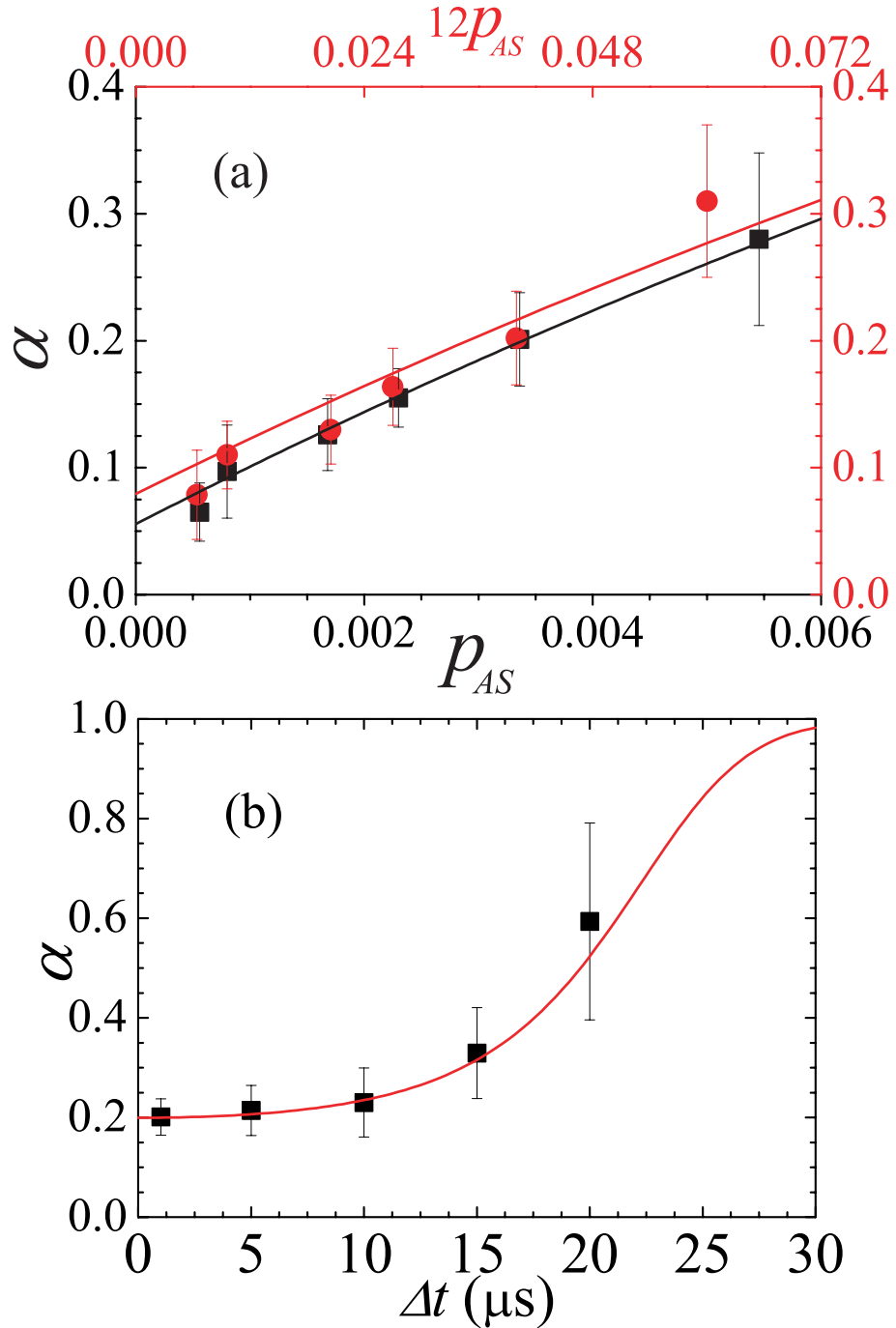


Figure 6.3: The anti-correlation parameter as a function of p_{AS} (a) and Δt (b). In panel (a), the data in black correspond to the experiment without feedback circuit, in which each write sequence is followed by one read pulse. The data in red corresponds to the experiment with feedback circuit, in which 12 successive write sequences are followed by one read pulse. The red curve is the theoretical evaluation taking into account the fitted background of the black dots. In panel (b), 12 write sequences were applied in each trial while measuring.

degraded by such noise. It is verified that α is conserved even with enhanced excitation probability. If the lifetime of the spin excitation is sufficiently long to allow many write sequences, the excitation probability can reach unity while the single-photon nature is still conserved. Then the generation efficiency only depends on the retrieve efficiency itself.

In the second experiment, we use $\delta t_w = 1 \mu\text{s}$ and $N = 12$. Fig. 6.3(b) shows the measured α as a function of Δt . For every Δt , ΔT varies due to the random creation of the spin excitation by the N write sequences. The behavior of $\alpha(\Delta t)$ is related to a reversed profile of $g_{AS,S}^{(2)}(\delta)$ in Fig. 6.3(b). For the delay $\Delta t < \tau_c$, the value of α stays at a low level and varies slowly. For $\Delta t > \tau_c$, $\alpha(\Delta t)$ increases towards 1. But even for a delay of $20 \mu\text{s}$ ($\sim 2\tau_c$) we find $\alpha \sim 0.6$. A satisfying agreement is observed between the theoretical curve and the experimental data.

6.4 Discussion

Typically, the single spin excitation can be produced at a rate of 600 per second, while the detection success probability per trial is 2.5%, the overall detection rate of single-photon production is $\sim 15 \text{ s}^{-1}$. As demonstrated in the present work, the lifetime of collective states is important for the quality and production rate of single photons. In the atomic ensemble, the coherence time of the collective state suffers from the residual magnetic field around the MOT and the collisions of the atoms. The latter effect is on the order of 1 ms, and thus is negligible in our experiment. Using a better compensation of residual magnetic field or using field insensitive clock states we can significantly increase the lifetime of the collective state [125]. Moreover, by further improving the control circuit, i.e. reducing the period of write pulses due to electronic delays, we can apply more write pulses within the lifetime. In particular, in the case with $p_{AS} = 0.003$ and a write period of 300 ns, we can obtain a single-photon source with a probability as high as 95% within a lifetime of 300 μs .

In conclusion, we have proposed and demonstrated an experimental realization of a controllable deterministic single-photon source with atomic storage. The lifetime of the collective spin excitation is 12.5 μs . A feedback circuit was constructed to control the generation of the spin excitation and the storage time δt . Being a key device in the scalable quantum communication network or in large scale linear optical computation, this circuit also shows a promising performance in the enhancement of the excitation probability while the single-photon quality is conserved. This single-photon source is able to work at either a deterministic mode or a time controllable mode heralded by the feedback circuit. The atomic-ensemble-based single-photon source has the advantages of narrow band [75], high quality and controllable character [74], which is helpful for the construction of scalable quantum information processing system in the future.

Chapter 7

Synchronized independent narrow-band single photons

In this chapter, synchronized generation of two indistinguishable photons from independent atomic ensembles is realized with the help of quantum memory and feedback circuit. The synchronized single photons are used to demonstrate efficient generation of entanglement. The resulting entangled photon pairs violate the Bell inequality by 5 standard deviations. Our synchronized single photons with their long coherence time of 25 ns and the efficient creation of entanglement serve as an ideal building block for scalable linear optical quantum information processing.

7.1 Introduction

Quantum key distribution and scalable linear optical quantum computation requires the ability of synchronized generation of indistinguishable single photons or entangled photon pairs from independent sources [6, 21]. With the help of quantum memory and feedback, fault-tolerant quantum repeater and probabilistic linear optical quantum computation can be implemented [18, 48, 126]. In recent years, interfering synchronized independent single photons and entangled photon pairs generated from two spontaneous parametric down-conversion sources have been reported where the two independent pumping lasers are synchronized [127, 128]. However, the spontaneous parametric source is probabilistic with a small probability p and the single photons are broad band (corresponding to a coherence length of a few nm determined by the bandwidth of the filters) [129]. Because there is no quantum memory for such broad-band single photons, no feedback circuit can be applied to improve the probability. Therefore, in an experiment concerning manipulation of N synchronized single-photon sources, the experimental efficiency will decrease exponentially with the number of photons (proportional to p^N). Moreover, the short coherence length of down-converted photons also makes the overlap of photon wave packets coming from two different sources difficult. These two drawbacks together make the above experiments impractical for long-distance quantum communication and linear optical quantum computation.

As we discussed in previous chapters, one can create narrow-band single photons or

entangled photon pairs in a deterministic and storable fashion with the help of atomic ensembles and a feedback circuit. In the past years, significant experimental progresses have been accomplished in demonstration of quantum storage of single photons [75, 92], and even entanglement in number basis for two atomic ensembles at a distance of 3 m has been reported [47]. Moreover, deterministic atomic ensembles based single-photon sources have been demonstrated by the aid of electronic feedback circuits [45, 46].

In this chapter, we develop further the techniques used in chapter 6 to implement synchronized generation of two independent single photons from two independent atomic ensembles at a distance of about 0.6 m. The two indistinguishable single photons are used to test the Bell inequality. Since our atomic-ensemble-based single-photon sources function in a deterministic and storable fashion with the help of a feedback circuit, the methods developed can be further used for scalable generation of multi-photon entanglement. Moreover, the coherence time of the single photons generated in atomic ensembles is controllable, and can be much longer than the short coherence time of down-converted photons. In current experiment, the coherence time of our narrow band single photons is about 25 ns, which makes it much easier for the two photons to overlap with each other. Finally, it is worth noting that the read and write lasers used for different single-photon sources are fully independent to each other.

7.2 Experiment

The experimental setup is depicted in Fig. 7.1. Atomic ensembles collected by two MOT's 0.6 m apart serve as the media for quantum memories and deterministic single-photon sources. Each ensemble consists of about 10^8 ^{87}Rb atoms. The two hyperfine ground states $|5S_{1/2}, F = 2\rangle = |a\rangle$ and $|5S_{1/2}, F = 1\rangle = |b\rangle$ and the excited state $|5P_{1/2}, F = 2\rangle = |e\rangle$ form a Λ -type system $|a\rangle - |e\rangle - |b\rangle$ [123]. At the beginning, the atoms are optically pumped to state $|a\rangle$. A write pulse Ω_w with the detuning of $\Delta = 10$ MHz and a beam diameter about $400 \mu\text{m}$ is applied to generate the spin excitation and an accompanying photon of the anti-Stokes field \hat{a}_{AS} with a beam diameter about $100 \mu\text{m}$. The mode \hat{a}_{AS} , tilted 3° from the direction of the write beam [130], is coupled in a single-mode fiber (SMF) and guided to a single-photon detector. The superposed state of the anti-Stokes field \hat{a}_{AS} and a collective spin state of the atoms can be described as,

$$|\Psi\rangle \sim |0_{AS}0_a\rangle + \sqrt{\chi}|1_{AS}1_a\rangle + \chi|2_{AS}2_a\rangle + O(\chi^{3/2}), \quad (7.1)$$

where $\chi \ll 1$ is the excitation probability of one spin flip, and $|i_{AS}i_a\rangle$ denotes the i -fold excitation of the anti-Stokes field and the collective spin. Ideally, conditioned on detecting one and only one anti-Stokes photon, a single spin excitation is generated in the atomic ensemble with certainty. In practice, considering photon loss in the detection, this condition can be fulfilled by keeping $\chi \ll 1$ so as to make the multi excitations negligibly small. After a controllable time delay δt_R (in the order of the lifetime τ_c of the spin excitation), another classical read pulse with the Rabi frequency Ω_R is applied with orthogonal polarization and spatially mode-matched with the write beam from the opposite direction. The spin excitation in the atomic ensemble will be converted into a

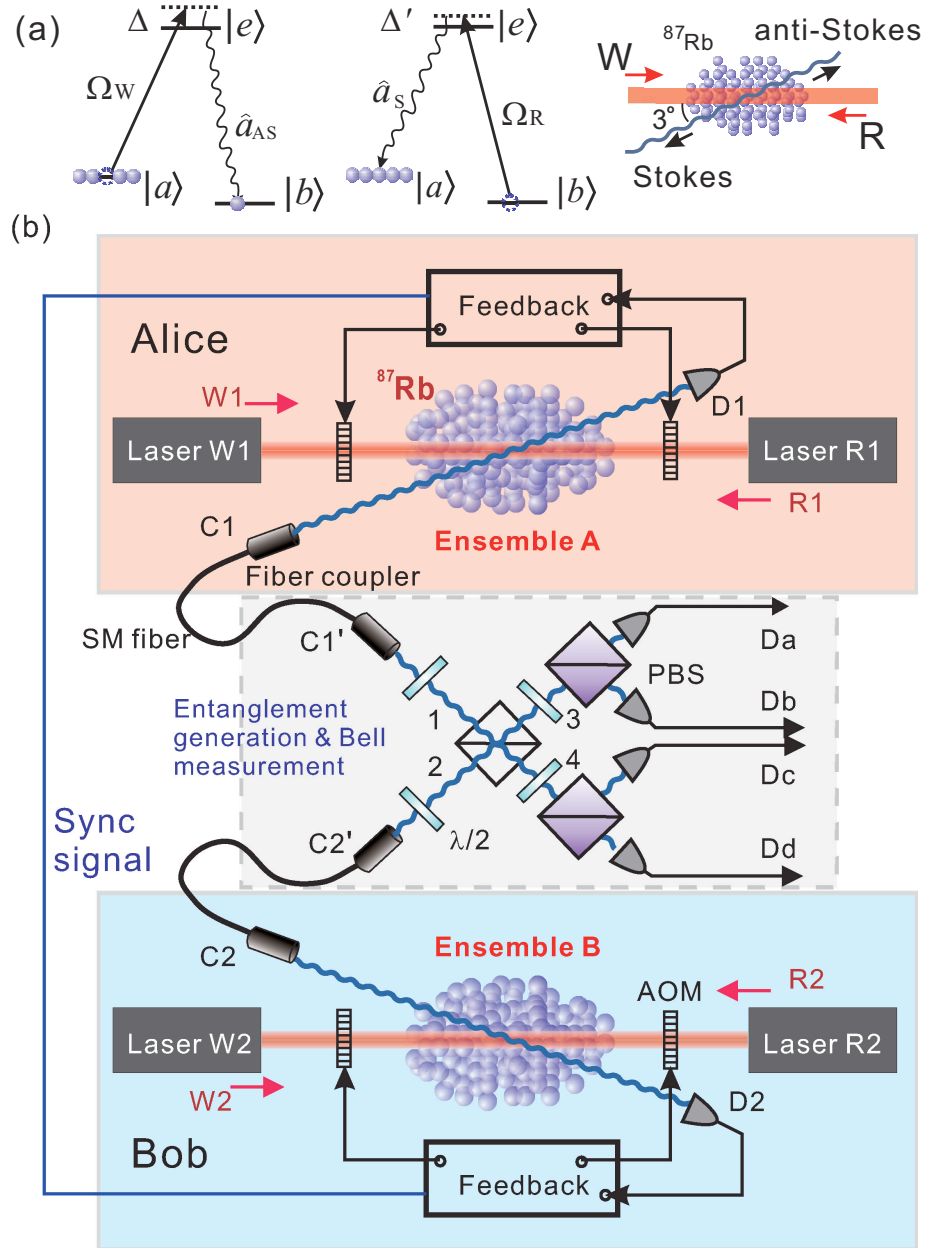


Figure 7.1: Illustration of the relevant energy levels of the atoms and arrangement of laser beams (a) and the experimental setup (b). Alice and Bob each keeps a single-photon source at two remote locations. As elucidated in chapter 6, Alice applies write pulses continuously until an anti-Stokes photon is registered by detector D1. Then she stops the write pulse, holds the spin excitations and meanwhile sends a synchronization signal to Bob and waits for his response (This is realized by the feedback circuit and the acousto-optic modulators, AOM). In parallel Bob prepares a single excitation in the same way as Alice. After they both agree that each has a spin excitation, each of them will apply a read pulse simultaneously to retrieve the spin excitation into a light field \hat{a}_S . The two Stokes photons propagate to the place for entanglement generation and Bell measurement. They overlap at a 50:50 beam splitter (BS) and then will be analyzed by latter half-wave plates ($\lambda/2$), polarized beam splitters (PBS) and single photon detectors Da, Db, Dc, and Dd.

single photon of the Stokes field \hat{a}_s , which propagates to the opposite direction of the field \hat{a}_{AS} and is also coupled in SMF. If the retrieve efficiency reaches unity, the Stokes photon is no longer probabilistic because of the quantum memory and feedback control, which now can serve as a deterministic single-photon source. As shown in Fig. 7.1b, Alice and Bob both have such a source. They prepare collective spin excitations independently and the one who finishes the preparation first will wait for the other while keeping the collective spin excitation in her/his quantum memory. After both of them have finished the preparation, they retrieve the excitations simultaneously at anytime they want within the lifetime of the collective state. Therefore the retrieved photons arrive at the beam splitter with the required timing.

Compared to a probabilistic photon source, the present implementation with atomic ensembles contributes a considerable enhancement to the coincidence rate of single photons coming from Alice and Bob. For instance, we consider a similar setup but without feedback circuit, where Alice and Bob apply write and read in every experimental trial and thereafter measure the four-fold coincidence of anti-Stokes and Stokes photons in the four channels D1, D2, C1 and C2. Assume the probability to have an anti-Stokes photon in channel D1 (D2) is p_{AS1} (p_{AS2}) and the corresponding retrieve efficiency for conversion of the spin excitation to a Stokes photon coupled into channel C1 (C2) is $\gamma_1(\delta t_R)$ [$\gamma_2(\delta t_R)$], then the probability of four-fold coincidence is $p_{4c} = p_{AS1}\gamma_1(\delta t_R)p_{AS2}\gamma_2(\delta t_R)$. This has to be compared with using the feedback circuits shown in Fig. 7.1b, where we can apply at most N (limited by the lifetime of the quantum memory and the speed of the feedback circuit) write pulses in each trial. Assume $p_{AS1} \ll 1$ and $p_{AS2} \ll 1$ and a long lifetime τ_c , the probability of four-fold coincidence is approximated as

$$P_{4c} \sim N^2 p_{AS1} \gamma_1(\delta t_R) p_{AS2} \gamma_2(\delta t_R) \quad (7.2)$$

for a definite number N . So the probability of four-fold coincidence is enhanced by N^2 for each trial. For our case $p_{AS1} \approx p_{AS2} = 2.0 \times 10^{-3}$ (the relevant cross correlation $g_{AS,S}^{(2)} = 30$), $N = 12$, $\tau_c \sim 12 \mu\text{s}$, $\delta t_W = 800 \text{ ns}$, $\delta t_R = 400 \text{ ns}$, and $\gamma_1(0) \approx \gamma_2(0) = 8\%$, the enhancement is 136.

The four lasers in Fig. 7.1b are independently frequency stabilized. The linewidths of W1 and R1 are about 1 MHz while those of W2 and R2 are about 5 MHz of the full width at half maximum (FWHM). However, they will be broadened to more than 20 MHz because the laser pulse modulated by the AOM is a Gaussian-like profile with width about 40 ns FWHM. The linewidth of the retrieved single photons is determined mainly by the linewidth and intensity of the read lasers. So we try to make the profile of the two independent read pulses identical to each other.

In order to verify that the two Stokes photons coming from Alice and Bob are indistinguishable, we let them overlap at a BS with the same polarization (horizontal in our case) and measure the quantum interference indicated by the the Hong-Ou-Mandel (HOM) dip. Having observed the high visibility of HOM dip in both time domain and frequency domain, we are confirmed that the two independent photons are indistinguishable. Then we put one of the two photons to vertical polarized before they enter the BS. By coincidence

measurement at the two outputs of the BS, we generate the Bell state

$$|\Psi^-\rangle_{12} = \frac{1}{\sqrt{2}}(|H\rangle_1|V\rangle_2 - |V\rangle_1|H\rangle_2), \quad (7.3)$$

which is verified by the measurement of violation of Bell inequality.

7.2.1 Theoretical description of HOM dip

The two-photon Hong-Ou-Mandel type interference can be described as follows [131]. The BS partially transmits and reflects the photons in mode 1 or 2 (see Fig. 7.1b), resulting in

$$|1\rangle_1 \longrightarrow \frac{1}{\sqrt{2}}(|1\rangle_3 + |1\rangle_4) \quad (7.4)$$

$$|1\rangle_2 \longrightarrow \frac{1}{\sqrt{2}}(|1\rangle_3 - |1\rangle_4) \quad (7.5)$$

with $|1\rangle_i$ the single photon state in mode i . Thus for the input state $|1\rangle_1|1\rangle_2$, we have

$$\begin{aligned} |1\rangle_1|1\rangle_2 &= \frac{1}{\sqrt{2}}(|1\rangle_3 + |1\rangle_4) \cdot \frac{1}{\sqrt{2}}(|1\rangle_3 - |1\rangle_4) \\ &= \frac{1}{\sqrt{2}}(|0\rangle_3|2\rangle_4 - |0\rangle_4|2\rangle_3), \end{aligned} \quad (7.6)$$

where $|0\rangle_i$ and $|2\rangle_i$ are the vacuum state and two photon state in mode i respectively. It can be easily seen that, if there are two indistinguishable photons impinging on the BS simultaneously, the probability to obtain a coincidence count in the output port 3 and 4 is zero.

To compare with the experiment results, we calculate the HOM dip in time and frequency domain by take into account the single-photon wave packets. The wave function of the free-running photons in mode i is defined by $\zeta_i(z, t)$. Thus the field operator in input ports 1 and 2 can be written as $E_1^+(t) = \zeta_1(t)a_1$ and $E_2^+(t) = \zeta_2(t)a_2$. Using these operators, the effect of the beam splitter is now described as a linear transformation between input and output modes

$$E_3^+(t) = \frac{E_1^+(t) + E_2^+(t)}{\sqrt{2}} = \frac{\zeta_1(t)a_1 + \zeta_2(t)a_2}{\sqrt{2}}, \quad (7.7)$$

$$E_4^+(t) = \frac{E_1^+(t) - E_2^+(t)}{\sqrt{2}} = \frac{\zeta_1(t)a_1 - \zeta_2(t)a_2}{\sqrt{2}}. \quad (7.8)$$

For the input state $|\psi_{in}\rangle = a_1^\dagger a_2^\dagger |0\rangle$, the joint probability for photon detections in the output modes 3 and 4 at times t_0 and $t_0 + \tau$, is given by

$$\begin{aligned} P_{joint}(t_0, \tau) &= \langle 0|a_1 a_2 E_3^-(t_0) E_4^-(t_0 + \tau) E_4^+(t_0 + \tau) E_3^+(t_0) a_1^\dagger a_2^\dagger |0\rangle \\ &= \frac{1}{4} |\zeta_1(t_0 + \tau)\zeta_2(t_0) - \zeta_2(t_0 + \tau)\zeta_1(t_0)|^2. \end{aligned} \quad (7.9)$$

Assume the photons in input port 1 and 2 are described by gaussian wave packets

$$\zeta_1(t) = \sqrt[4]{2/\pi} \exp(-(t - \delta\tau/2)^2 + i\Delta t/2), \quad (7.10)$$

$$\zeta_2(t) = \sqrt[4]{2/\pi} \exp(-(t + \delta\tau/2)^2 - i\Delta t/2), \quad (7.11)$$

where the delay between the photons $\delta\tau$ and the frequency difference Δ are expressed in units of the pulse duration. A straight forward evaluation leads to the joint photon-detection probability

$$P_{joint}(t_0, \tau, \delta\tau, \Delta) = \frac{\cosh(2\tau\delta\tau) - \cos(\tau\Delta)}{\pi} \exp(-4t_0(t_0 + \tau) - \delta\tau^2 - 2\tau^2). \quad (7.12)$$

Integrating out t_0 , we will obtain the probability of detecting two photons in the ports 3 and 4 with a time difference of τ ,

$$P_{joint}(\tau, \delta\tau, \Delta) = \frac{\cosh(2\tau\delta\tau) - \cos(\tau\Delta)}{2\sqrt{\pi}} \exp(-\delta\tau^2 - \tau^2). \quad (7.13)$$

Integrating out the detection delay and choose $\Delta = 0$ or $\delta\tau = 0$, we obtain the HOM dips in the time domain and frequency domain respectively

$$P_{joint}(\delta\tau) = \frac{1}{2}[1 - \exp(-\delta\tau^2)], \quad (7.14)$$

$$P_{joint}(\Delta) = \frac{1}{2}[1 - \exp(-\Delta^2/4)]. \quad (7.15)$$

7.2.2 The measurement of HOM dip

We did two measurements to obtain the HOM dip in time domain and frequency domain respectively. To make the photons indistinguishable, the polarizations of the anti-Stokes photons were set to horizontal with two half-wave plates before they enter the BS as shown in Fig. 7.1b. The other two half-wave plates after the BS were set to 0° .

In the first measurement, we measured the four-fold coincidence among detectors D1, D2, Da and Dd while changing the time delay between the two read pulses (Fig. 7.2, upper panel), which corresponds to zero frequency difference and non-zero photon delay. The excitation probabilities $p_{AS1} \approx p_{AS2} = 2.0 \times 10^{-3}$. The coincidence rate varies with the delay. Ideally, there should be complete destructive interference if the wave packets of the two photons overlap perfectly. However, it is hard to make the two wave packets absolutely identical or exactly overlapped in practice. We obtained the visibility of the dip $V = (C_{\text{plat}} - C_{\text{dip}})/C_{\text{plat}} = (80 \pm 1)\%$, where C_{plat} is the non-correlated coincidence rate at the plateau and C_{dip} is the interfering coincidence rate at the dip. The asymmetry of the profile at negative delay and positive delay shows that the two wave packets are (a) not perfectly identical, (b) not symmetric themselves. Assume the HOM dip is a Gaussian-type profile, we estimate the coherence time is 25 ± 1 ns FWHM.

In the second measurement, we measured the four-fold coincidence among detectors D1, D2, Da and Dd while changing the frequency detuning between the two read pulses (Fig. 7.2, lower panel), which corresponds to zero photon delay and non-zero frequency difference. It is the first time to measure HOM dip in the frequency domain at single-

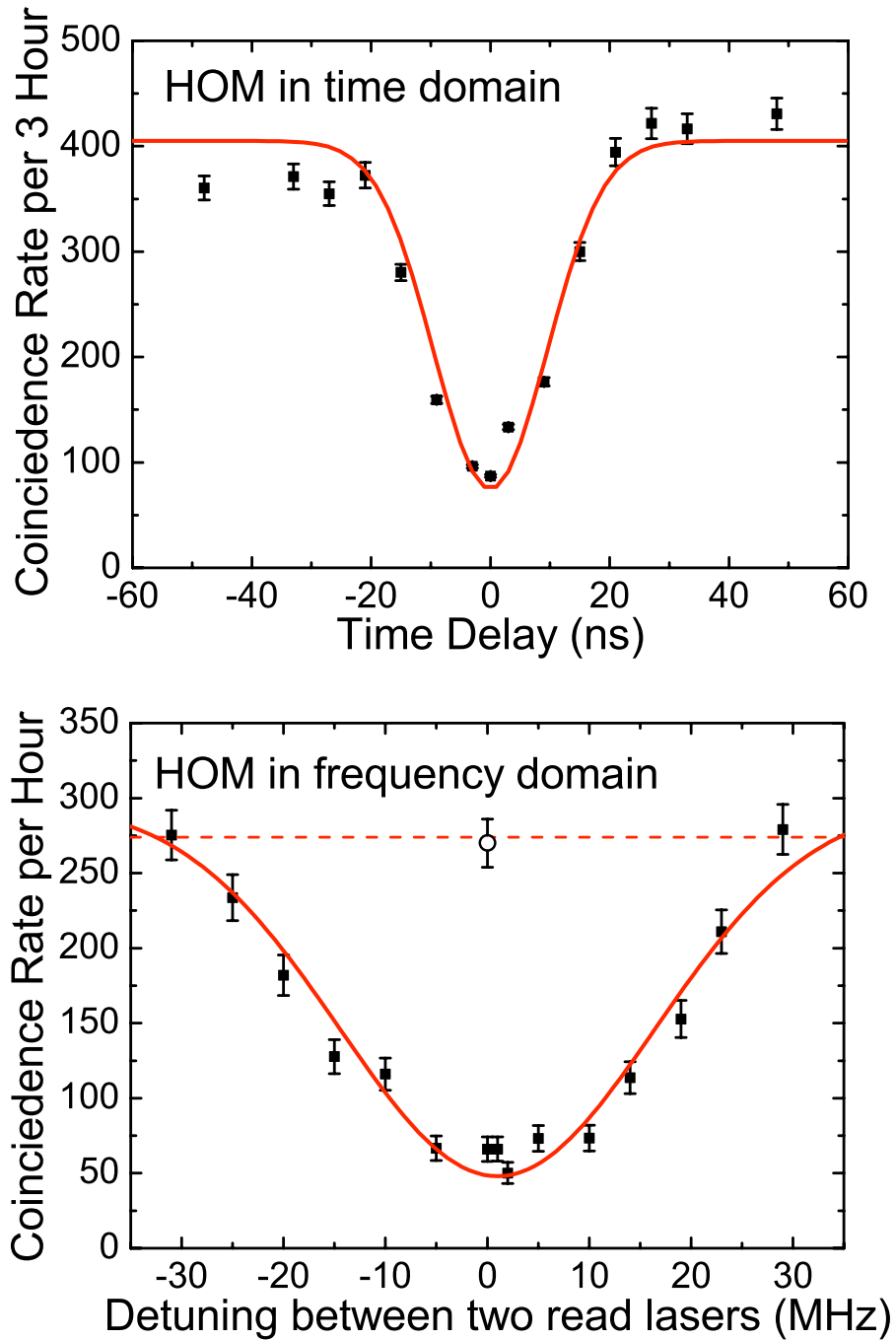


Figure 7.2: Hong-Ou-Mandel dips in time domain (upper panel) and frequency domain (lower panel). The circle in the lower panel was obtained by setting the polarization of the two photons perpendicular to each other and zero detuning between two read lasers. The Gaussian curves that roughly connect the data points are only shown to guide the eye. The dashed line shows the plateau of the dip. Error bars represent statistical errors, which are ± 1 standard deviation.

photon level. The excitation probabilities are $p_{AS1} \approx p_{AS2} = 3.0 \times 10^{-3}$, higher than those in the time domain. Because of the limit of the current setup, the detuning can be varied from -30 MHz to 30 MHz. In order to verify the coincidence rate at the largest detuning reached the plateau of HOM dip, we measured the coincidence by setting the polarization of the two photons perpendicular to each other and zero detuning between the two read lasers (shown as a circle in Fig. 7.2). The consistence of this data with those two at the largest detunings shows that we have achieved the plateau of HOM dip. The visibility is $(82 \pm 3)\%$ which agrees well with that obtained in time domain. The width of the HOM dip is 35 ± 3 MHz FWHM, in accordance with the coherence time 25 ns. Therefore, the narrow-band characteristic of the present source is verified directly by the HOM dip in the frequency domain.

Besides the overlap of the two photon wave packets, the imperfection of the single photon sources affects the visibility as well. As discussed in chapter 6, the quality of single-photon source is characterized by the anti-correlation parameter $\alpha = 2P_{II}/P_I^2$, where P_I (P_{II}) is the probability of generating one (two) photon(s) for each source (the higher orders are negligible small). If the two wave packets do not overlap at all, there is no interference between them. Then we obtain the non-correlated coincidence rate $C_{\text{plat}} = P_I^2/2 + P_{II}$ between Da and Dd. If they overlap perfectly, there is destructive interference leading to a coincidence rate $C_{\text{dip}} = P_{II}$. So the visibility of the HOM dip is $V = 1/(1 + \alpha)$. In our experiment, $\alpha = 0.12$ for the source prepared later (the spin excitation is retrieved immediately) and $\alpha = 0.17$ for the source prepared earlier (it has to wait for the other one). This leads to an average visibility of 87% . In the frequency domain, the average visibility is around 83% because of higher excitation probabilities.

7.2.3 Time resolved two-photon interference

Note that, in Fig. 7.2 HOM dip is measured by setting the coincidence window (here ~ 50 ns) larger than the wave-package length of the single photons (~ 25 ns). In Fig. 7.3, we measure the time-resolved two-photon quantum interference by setting the wave-packet at perfectly temporal overlap and setting the coincidence window (2 ns in the experiment) much shorter than the wave-packet length. The red spots are measured under perpendicular polarization and the black ones are measured under parallel cases. From Eq. (7.13), it can be easily seen that in this case the photon delay $\delta\tau$ and frequency difference Δ are both zero, and thus the joint probability should be zero in ideal case. Our experimental results show a dip at 0 delay. The nonzero value at $\tau \neq 0$ is mainly because the two photons are not fully indistinguishable [132].

7.2.4 Test Bell inequality

We also test the Bell inequality by using post-selection [133]. As shown in Fig. 7.1b, we set orthogonal polarizations (horizontal and vertical) of the Stokes photons with the two half-wave plates before the BS. Then the state of the two photons will be projected to $|\Psi^-\rangle_{12}$ if there is coincidence between the two output port 3 and 4. With another two half-wave plates and two PBSs after the BS, the entanglement of the two photons can be

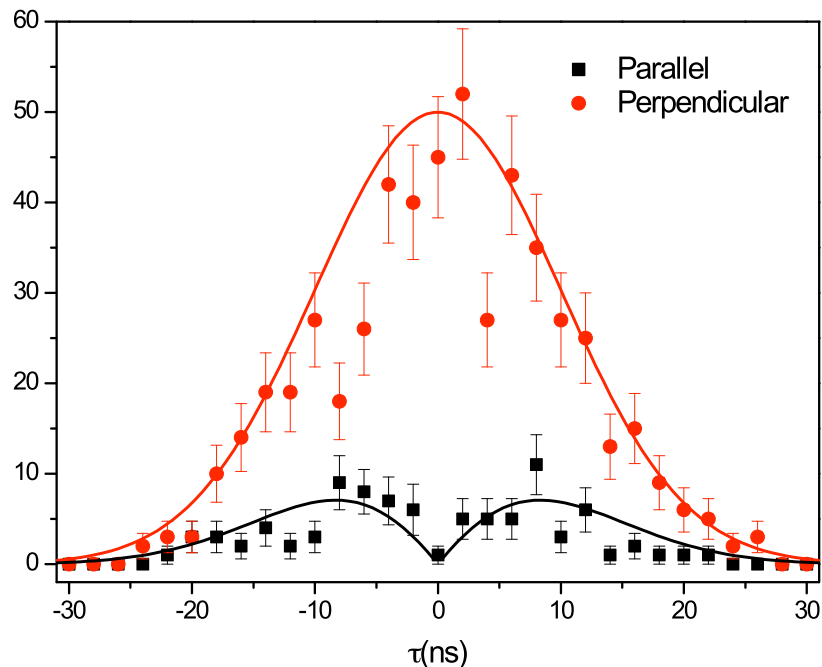


Figure 7.3: Hong-Ou-Mandel dips in time domain with coincidence window (2 ns) much shorter than the wave-packet length. The red spots are measured under perpendicular polarization and the black ones are measured under parallel cases.

Table 7.1: Correlation functions E and the resulting S .

E	$\theta_1 = 0^\circ$	$\theta'_1 = 45^\circ$	S
$\theta_2 = 22.5^\circ$	-0.613 ± 0.037	0.575 ± 0.039	
$\theta'_2 = -22.5^\circ$	0.606 ± 0.038	0.579 ± 0.039	2.37 ± 0.07

verified by a Clauser-Horne-Shimony-Holt (CHSH) type inequality, where $S \leq 2$ for any local realistic theory with

$$S = |E(\theta_1, \theta_2) - E(\theta_1, \theta'_2) - E(\theta'_1, \theta_2) + E(\theta'_1, \theta'_2)|. \quad (7.16)$$

Here $E(\theta_1, \theta_2)$ is the correlation function where θ_1 and θ'_1 (θ_2 and θ'_2) are the measured polarization angles of the Stokes photon at port 3 (4). The observed values of the correlation functions are listed in Table 7.1 resulting in $S = 2.37 \pm 0.07$, which violates the CHSH inequality by 5 standard deviations. Taking into account the two photon component in the single-photon sources, a straightforward calculation shows the violation of the CHSH inequality is about 2.3, which is in good agreement with the experimental results.

7.3 Discussion

In conclusion, we realized synchronized generation of narrow-band single photons from two independent atomic ensembles. The Hong-Ou-Mandel dip was observed in both time domain and frequency domain with a high visibility for independent photons coming from

two distant sites, which shows the indistinguishability of these photons. A time resolved two-photon interference is observed as well, which is consistent with theoretical prediction. By virtue of quantum memories and feedback circuits, the efficiency of generating entangled photon pairs was enhanced by a factor of 136, which claims our single-photon source as a promising candidate for the future implementation of scalable quantum computation based on linear optics. The present spatially-distributed independent single-photon sources with fully independent write and read lasers and narrow-band property of the single photons profit the present sources to serve as an ideal candidate for long distance quantum communication with atomic ensembles and linear optics. Further improvement of our single-photon source can be realized by increasing the optical density of the atomic ensemble and using clock state to store the quantum state [125, 134]. If we want a long lifetime, a good solution is to confine the atoms in an optical trap, which also benefits to a much higher optical density.

Chapter 8

Quantum teleportation between photonic and atomic qubits

In this chapter, we report the first demonstration of quantum teleportation between a photonic qubit and a memory qubit. The polarization state of a single photon is teleported to the collective state of a pair of atomic ensembles serving as a memory qubit. The quantum state is stored for a while and then retrieved out to measure the teleportation fidelity. Our results show that up to 8 μs , the teleportation fidelity is still above the classical threshold.

8.1 Introduction

Quantum teleportation is a remarkable protocol to transfer an unknown quantum state from one place to another by means of entanglement [1, 135]. It is one of the most intriguing examples of how quantum entanglement can assist in realizing practical quantum key distribution and quantum computation. Quantum teleportation was first realized between two photonic qubits generated from parametric down-converted source [2, 24, 25, 136, 137] and between two ions trapped in a linear Paul trap [14, 15]. Most recently, quantum teleportation from coherent light to atomic ensemble is also reported [138, 139].

However, the above demonstrations of teleportation have severe drawbacks and can't be used in long-distance quantum communication. For the quantum teleportation between photonic qubits, there is no quantum memory for the photonic qubit and thus is not scalable [2, 24, 25, 136, 137]. For the teleportation in ion traps [14, 15], the distance between two ions is a few micrometers, and is impossible to extend to longer distances since the entangled pair has to be prepared locally. For the continuous variable teleportation between light and matter [139], the fidelity is extremely sensitive to the transmission loss - even in the ideal case only a maximal attenuation of 10^{-1} is tolerable [140], and it is difficult to convert the state stored in the atomic ensemble back to a coherent light. Remarkably, the combination of quantum teleportation and quantum storage of photonic

qubits could provide a novel way to overcome these drawbacks. Even though either of them has been demonstrated separately in many proof-of-principle experiments, the demonstration of such a memory-built-in teleportation of photonic qubits, remains an experimental challenge.

In this chapter, we report an experimentally implementation of quantum teleportation between discrete flying photonic and atomic stationary qubits. In our experiment, we use the polarized photonic qubits as the source qubits and the collective atomic qubits as the target qubits serving as the quantum memory. In memory-built-in teleportation, the unknown polarization state of single photons is teleported onto and stored in a remote memory qubit by means of a Bell-state measurement (BSM) between the source photon and the photon entangled with the atomic qubit. The unknown state stored in the atomic ensemble is retrieved out after a controllable delay. The teleportation fidelity is above the classical threshold up to 8 μ s.

8.2 Experimental scheme

A schematic setup of our experiment is shown in Fig. 8.1. The two ground states $|a\rangle$ ($5S_{1/2}, F = 2$) and $|b\rangle$ ($5S_{1/2}, F = 1$) form together with the excited level $|e\rangle$ ($5P_{1/2}, F' = 2$) a Λ -type system. At Bob's site, the two ensembles located in two magneto-optical traps (MOTs) of ^{87}Rb 0.6 m apart are prepared in the ground state $|a\rangle$. A weak classical write pulse coupling the transition $|a\rangle \rightarrow |e\rangle$ with a red detuning Δ (10 MHz) and the Rabi frequency Ω_w into ensembles m ($m = U$ or D) is applied to the two atomic ensembles and creates a superposition between the anti-Stokes field \hat{a}_{AS} and a collective spin state of the atoms,

$$|\Psi\rangle_a = |0_{AS}0_a\rangle_m + \sqrt{\chi_m}|1_{AS}1_a\rangle_m + O(\chi_m), \quad (8.1)$$

where $\chi_m \ll 1$ is the excitation probability of one spin flip in ensemble m , and $\sqrt{\chi_m}|i_{AS}i_a\rangle_m$ denotes the i -fold excitation of the anti-Stokes field and the collective spin. We adjust $\chi_U = \chi_D$, select orthogonal polarization of the two anti-stokes fields and combine them on a polarized beam splitter (PBS₁), as illustrated in Fig. 8.1. The total entangled state between photonic and atomic qubits generated in the write process is equivalent to the maximally polarization entangled state generated by spontaneous parametric down-conversion, which can be described as an effectively entangled state

$$|\Psi\rangle = \frac{1}{\sqrt{2}} \left(|H\rangle|\tilde{V}\rangle + |V\rangle|\tilde{H}\rangle \right), \quad (8.2)$$

where $|\tilde{H}\rangle = |0_a\rangle_U|1_a\rangle_D$ ($|\tilde{V}\rangle = |1_a\rangle_U|0_a\rangle_D$) denotes one spin excitation in ensemble $D(U)$. Note that, the coherence time of the photonic qubit in the atom-photon entangled state is about 25 ns, which makes the two photons easily overlap on the BS.

After the write process, the anti-Stokes photon is sent to Alice over a 7 m long fiber. Suppose that at Alice's site, the source photonic qubit is in an unknown polarization state $|\phi\rangle = \alpha|H\rangle + \beta|V\rangle$. The total state of the three qubits can be expanded in terms of four

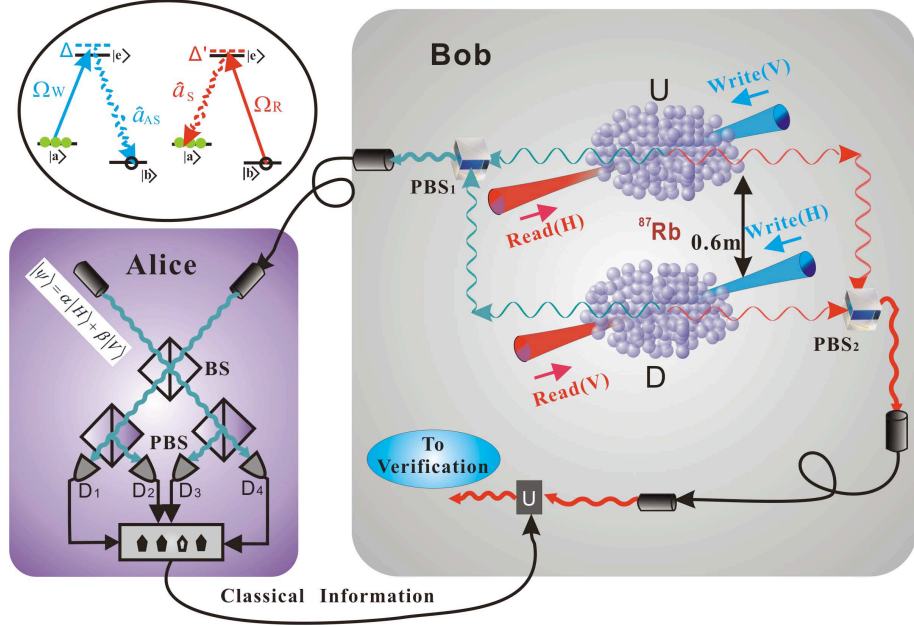


Figure 8.1: Experimental setup for teleportation between photonic and atomic qubits. The inset shows the structure and the initial populations of atomic levels for the two ensembles. At Bob's site the anti-Stokes fields emitted from U and D are collected and combined at PBS_1 , selecting perpendicular polarizations. Then the photon travels 7 m through fibers to Alice's side to overlap with the initial unknown photon on a beam-splitter (BS) to perform the BSM. The results of the BSM are sent back to Bob via a classical channel. Bob can then perform the verification of the teleported state in the U and D ensembles by converting the atomic excitation to a photonic state. A unitary operation on the converted photon is performed according to the classical information from the results of BSM.

Bell states,

$$|\phi\rangle|\Psi\rangle = \frac{1}{2}(|\Phi^+\rangle\hat{\sigma}_x|\tilde{\phi}\rangle + |\Phi^-\rangle(-i\hat{\sigma}_y|\tilde{\phi}\rangle) + |\Psi^+\rangle|\tilde{\phi}\rangle + |\Psi^-\rangle\hat{\sigma}_z|\tilde{\phi}\rangle) \quad (8.3)$$

where $|\Psi^\pm\rangle = (|HV\rangle \pm |VH\rangle)/\sqrt{2}$, and $|\Phi^\pm\rangle = (|HH\rangle \pm |VV\rangle)/\sqrt{2}$ are the four Bell states, $\hat{\sigma}_x$, $\hat{\sigma}_y$ and $\hat{\sigma}_z$ are the Pauli matrices, and $|\tilde{\phi}\rangle = \alpha|\tilde{H}\rangle + \beta|\tilde{V}\rangle$ is the desired atomic state. It can thus be seen that a joint BSM on the two photons at Alice's side projects the state of atomic qubit at Bob's side into the unknown state up to a local unitary transformation. After the BSM, the initial state of photonic qubit is thus transferred to and stored in the atomic qubit. Depending on the results of the BSM, Bob can then perform a unitary transformation on the atomic qubit to convert its state into the initial state of the photonic qubit.

The BSM on the two photons at Alice's hand is implemented by supposing them on a 50:50 BS (see Fig. 8.1), and then registering the coincidence counts in the output ports. The BSM is capable of identifying two of the four Bell-states, i.e., $|\Psi^+\rangle$ and $|\Psi^-\rangle$ in our experiment. Note that, to demonstrate the principle of teleportation it is sufficient to identify only one of the four Bell-states, e.g., via identification of $|\Psi^+\rangle$ and verification of $|\tilde{\phi}\rangle$.

To verify the success of teleportation, the atomic excitation is converted back to a Stokes photon in a controllable way by applying two simultaneous read pulses, coupling

the transition $|b\rangle \rightarrow |e\rangle$ with a blue detuning Δ' (6 MHz) and the Rabi frequency Ω_R . The polarizations of the two read pulses are selected to be perpendicular with respect to the corresponding write pulses. The retrieved Stokes fields are then combined at PBS_2 . Hence, the atomic qubit is converted back to a single-photon polarization state. We can then measure the quantum state of the Stokes photon to obtain the teleportation fidelity.

Conditioned on detecting the Bell state $|\Psi^+\rangle$ state at Alice's side, the state of the atomic qubit at Bob's side will be projected into the state $|\tilde{\phi}\rangle$. The collective atomic state $|\tilde{\phi}\rangle$ will be converted into exactly the initial polarization state $|\phi\rangle$ after the read process. On the other hand, if a $|\Psi^-\rangle$ state is detected, we will have the atomic qubit in the state $\hat{\sigma}_z|\tilde{\phi}\rangle$, which is equivalent to the initial state except for a unitary transformation $\hat{\sigma}_z$. Consequently, applying $\hat{\sigma}_z$ on the converted single-photon polarization state we will again obtain the same initial state $|\phi\rangle$. It is worth noting that, the ease of both transferring atomic excitation to optical excitation and exploiting linear optical elements to perform precise unitary transformation on single-photon states is a distinct advantage of our method.

In our experiment for simplicity we use a weak coherent pulse to prepare the source photonic qubit. Without loss of generality, we select three polarization states, i.e., horizontal ($|H\rangle$), 45-degree ($|+\rangle = \frac{1}{\sqrt{2}}|H + V\rangle$) and right-hand circular ($|R\rangle = \frac{1}{\sqrt{2}}|H + iV\rangle$) as our initial states. As shown in Fig. 8.1, after knowing the BSM results at Alice's site, the atomic excitation at Bob's site is then converted back to a photonic state in a controllable time to analyze the teleportation fidelity. Note that, the two-photon events from the weak coherent pulses would also contribute a significant amount of unfavorable two-fold BSM coincidences, and thus a two-fold BSM click could only herald the success of teleportation with an average probability of about 40% in our experiment. Therefore, as in previous teleportation experiments, our teleportation only occurs posteriorly when a three-fold coincidence count is registered.

8.3 Experimental realization

8.3.1 Preparation of the entanglement

In the experiment, the MOT is loaded for 20 ms at a repetition rate of 40 Hz. The magnetic field and the cooling beams are then quickly switched off while the repumping beams stay on for 0.5 ms before being switched off in order to prepare the atoms in the initial $F = 2$ ground state $|a\rangle$. Then, within another 4.5 ms experimental trials (each consisting of successive write, read and repumping pulses) are repeated with a controllable period depending on the desired retrieve time of the teleported state. In each experimental trial, two write pulses Ω_w with the red detuning of $\Delta = 10$ MHz, beam diameter about 400 μm and orthogonal polarization are simultaneously applied to the two atomic ensembles to generate the spin excitation and two accompanying anti-Stokes fields \hat{a}_{AS} with beam diameter about 100 μm . The anti-Stokes modes are tilted 3° from the direction of the corresponding write beam, and guided to PBS_1 and then sent to Alice's side by a single-mode fiber.

To verify the atom-photon entanglement, we map the atomic excitations back into a single photon by sending two classical read pulses through the two ensembles. The

retrieved Stokes fields with perpendicular polarizations are combined on PBS₂ (see Fig. 8.1). The superposition state of anti-Stokes and Stokes fields is effectively equivalent to the following maximally polarization entangled state

$$|\Psi\rangle_{AS,S} \sim |H\rangle_{AS}|V\rangle_S + e^{i(\phi_1+\phi_2)}|V\rangle_{AS}|H\rangle_S. \quad (8.4)$$

Here $\phi_{1(2)} = \Delta\theta_{W(R)} + \Delta\theta_{AS(S)}$ represents the phase difference between the two anti-Stokes (Stokes) fields at the PBS₁ (PBS₂). As shown in Fig. 8.2, $\Delta\theta_{W(R)}$ arises from the path difference of the two write (read) beams from BS₂ (BS₁) to the U and D ensembles, and $\Delta\theta_{AS(S)}$ arises from the path difference between the two anti-Stokes (Stokes) fields from the U and D ensembles to the PBS₁ (PBS₂). In the experiment $\Delta\theta_W + \Delta\theta_{AS}$ and $\Delta\theta_R + \Delta\theta_S$ are actively stabilized by two Mach-Zehnder interferometers, respectively. Note that, even though the phase $\phi_{1(2)}$ might vary from trial to trial, the total phase $\phi_1 + \phi_2$ is actively stabilized and fixed to zero.

After the effective entanglement between the photonic and atomic qubits is generated, the photon travels 7 m through an optical fiber to Alice's site, where it is overlapped with the initial unknown photon on a BS performing the BSM. Knowing the BSM results through classical communication, Bob can then perform the verification of the teleported state in the U and D ensembles by converting the atomic excitation to a photonic state. If a $|\Psi^+\rangle$ is registered, Bob directly performs a polarization analysis on the converted photon to measure the teleportation fidelity. On the other hand, if a $|\Psi^-\rangle$ is registered, the converted photon is sent through a HWP via the first order diffraction of an AOM. The HWP is set at 0 degree serving as the unitary transformation of $\hat{\sigma}_z$. Then the photon is further sent through the polarization analyzer to obtain the teleportation fidelity.

8.3.2 Phase locking

In order to stabilize the phase $\phi_1 + \phi_2$ in expression (8.4) actively, two Mach-Zehnder interferometers are used as shown in Fig. 8.1. Because the spatial modes of anti-Stokes (Stokes) field and write (read) beam have 3° angle, we can not lock the phase $\phi_1 (= \Delta\theta_W + \Delta\theta_{AS})$ and $\phi_2 (= \Delta\theta_R + \Delta\theta_S)$ directly. However, we can lock the phase of $\Delta\theta_W + \Delta\theta_R$ and $\Delta\theta_{AS} + \Delta\theta_S$ separately.

To stabilize the phase of $\Delta\theta_W + \Delta\theta_R$, the read beam is switched on during the 20 ms MOT loading stage, used as the locking beam (Fig. 8.2a). During the 5 ms experimental stage, the shutter is switched off. The interference signal can be used as the error signal of a standard proportional-integrate (PI) locking circuit. The error signal is normalized by the duty cycle and then sent to the homebuilt PI circuit. By controlling the voltage of the piezo (P1) we can lock the phase $\Delta\theta_W + \Delta\theta_R$ to a set value.

To stabilize the phase of $\Delta\theta_{AS} + \Delta\theta_S$, an additional locking beam polarized at 45 degree with the frequency of read beam is sent in at the angle of the first order diffraction of the AOM (Fig. 8.2b) during the MOT loading stage. Passing through the AOM, the locking beam is overlapped with the Stokes and anti-Stokes beams. Since the anti-Stokes and Stokes light are perpendicularly polarized, the output of the locking beam is from another port of PBS₁. After the locking beam goes through a polarizer at 45 degree, the

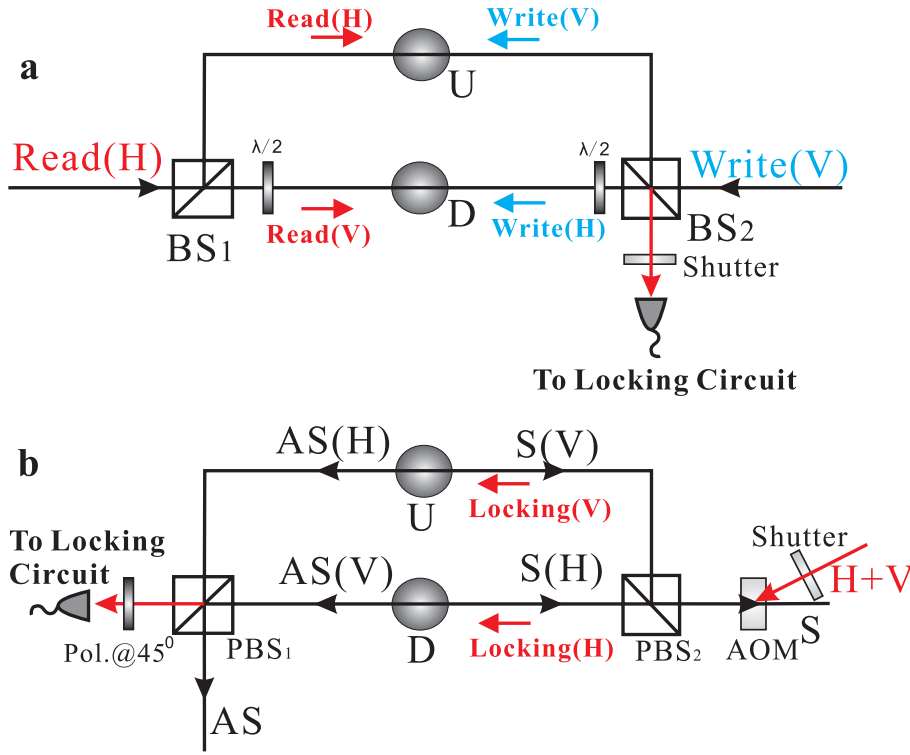


Figure 8.2: Schematic drawing of the phase locking setup. Two Mach-Zehnder interferometers are used to actively stabilize the phases between the arms of write and read paths (a) and between the arms of anti-Stokes and Stokes paths (b), respectively. H/V denotes the horizontal/vertical polarization, and AOM denotes an acousto-optic modulator. A polarizer (Pol.) is set at 45° to erase the polarization information. The HWP's ($\lambda/2$) are set at 45° as well to rotate the horizontal polarization to vertical. AS (S) denotes the anti-Stokes (Stokes) photon.

interference signal can be detected by a photodiode and used to lock the phase $\Delta\theta_{AS} + \Delta\theta_S$. During the experimental stage, the shutter and the RF power of AOM are all switched off to prevent the leakage of the locking beam from entering the anti-Stokes – Stokes channels. In this way, the overall phase of $\phi_1 + \phi_2$ is actively locked.

8.3.3 Experimental results

With an anti-Stokes photon generation probability of 0.003, the signal-to-noise ratio between the desired ($|H\rangle_{AS}|V\rangle_S$ and $|V\rangle_{AS}|H\rangle_S$) and unwanted ($|H\rangle_{AS}|H\rangle_S$ and $|V\rangle_{AS}|V\rangle_S$) components is observed to be 15:1, corresponding to a visibility of 87.5% with a statistical error 0.4%. This confirms that the $|H\rangle_{AS}|V\rangle_S$ and $|V\rangle_{AS}|H\rangle_S$ terms are the dominant components. Furthermore, in order to prove the two terms are indeed in a coherent superposition, we also measure the signal-to-noise ratio in the 45-degree polarization basis. The experimental results of the polarization correlation exhibit an interference fringe with a visibility of $(82.2 \pm 0.4)\%$, confirming the high quality of our atom-photon entanglement.

Table 8.1 shows the experimental result of the teleportation fidelities at a retrieval time of $0.5 \mu s$. The results show the fidelities for different initial states are all well beyond the classical limit of 0.67, confirming the success of teleportation between photonic and atomic qubits.

Table 8.1: Fidelities of teleporting a photonic qubit at a storage time of $0.5 \mu s$. Data for teleporting each state are collected two hours. The error bars represent the statistical error, i.e., ± 1 standard deviation.

Original state	fidelities
$ H\rangle$	0.865 ± 0.017
$ +\rangle$	0.737 ± 0.009
$ R\rangle$	0.750 ± 0.009

To show the ability to store the teleported state in our quantum memory, we further measure the fidelity of teleportation of right-hand circular polarization for different retrieval time. The result is shown in Fig. 8.3. Up to $8 \mu s$ the fidelity is still above the classical limit. The fidelity drops down mainly because of the decoherence in the collective atomic state.

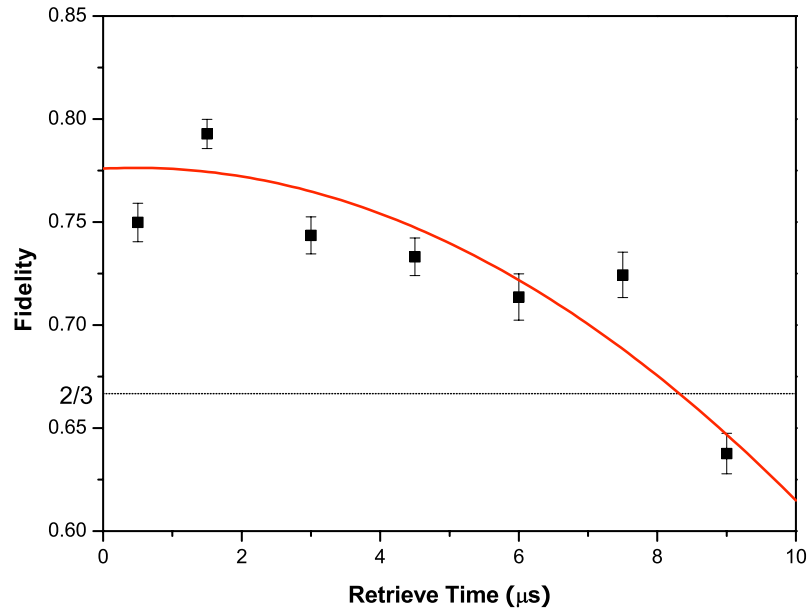


Figure 8.3: Fidelity of the teleported state in atomic ensembles along storage time. The initial state to be teleported is $(|H\rangle + i|V\rangle)/\sqrt{2}$. Until $8 \mu s$ the fidelity is still well beyond the classical limit of $2/3$. Each experimental point is measured for about four hours (averagely). The curve is a Gaussian fit, due to the Gaussian decay of the retrieve efficiency. The error bars represent the statistical error, i.e., ± 1 standard deviation.

8.4 Noise estimation

8.4.1 Bell-state measurement

As we discussed in section 8.2, using the weak coherent light as the single photons leads to many unfavorable coincidence counts in BSM. Thus, a BSM result, i.e., a two-fold

coincidence, would mainly have three components:

(1) Coincidence between an anti-Stokes photon and the single photon component in the weak coherent beam, which is the desired BSM result and has a probability of $\sim \frac{1}{2}p_{AS}p_0\eta^2$. Here $p_0 = 0.03$ is the probability of containing a single photon for each weak coherent pulse, and η is the average overall detection efficiency of our single-photon detectors, including the collection efficiency ($\sim 75\%$) and the detection efficiency of the detectors ($\sim 50\%$).

(2) Spurious coincidence contributed by the two photon component from the weak coherent beam. In teleportation of $|+\rangle$ and $|R\rangle$ states, the probability of registering such two-fold coincidence is given by $\sim \frac{1}{4}p_0^2\eta^2$. However, since only $|\Psi^\pm\rangle$ is analyzed in our BSM, in teleportation of $|H\rangle$ state, the two photon component from the weak coherent beam has no effect.

(3) Spurious coincidence contributed by the double emission from the atomic ensembles, which has a probability of $\sim \frac{1}{4}p_{AS}^2\eta^2$.

In our experiment, the intensity of the write pulses is adjusted such that the excitation probability of creating an anti-Stokes photon is $p_{AS} \sim 0.003$. The retrieval efficiency is about $\gamma \sim 30\%$, which is mainly limited by the optical depth of the atomic ensembles. After each write and read process, the probability of emitting a single photon in Stokes mode (denoted by p_S) is measured to be ~ 0.004 . In each weak coherent pulses, the probability of containing a single photon is $p_0 \sim 0.03$. Substituting the experiment parameters, we find that, for $|H\rangle$ teleportation, a BSM click will herald the success of teleportation with a probability of 95%. While for $|+\rangle$ and $|R\rangle$ teleportation, a BSM click will only with a probability of 17% herald the success of teleportation. Thus given an arbitrary input state the average probability to herald the success of teleportation is around $(95\% + 2 \times 17\%) / 3 = 40\%$.

8.4.2 Teleportation fidelity

In our experiment, the three-photon coincidence counts imply the success of the quantum teleportation. Our three-fold coincidence would mainly have three components as well:

(1) Coincidence among a single photon of the initial state from the weak coherent beam, an anti-Stokes photon, and a successfully retrieved Stokes photon, which is the desired event and has a probability of $\sim \frac{1}{2}p_{AS}p_0\gamma\eta^3$. Thus, the overall success probability of the teleportation in each experimental run is around 10^{-6} .

(2) Spurious coincidence contributed by a two-photon event (the double emission) from the weak coherent pulse and a single-photon event in Stokes mode. For $|+\rangle$ and $|R\rangle$ teleportation the probability of registering such three-fold coincidence is given by $\sim \frac{1}{4}p_0^2p_S\eta^3$ and no such spurious three-fold coincidence in $|H\rangle$ teleportation.

(3) Spurious coincidence contributed by double emission from the atomic ensembles and one retrieved Stokes photon, which has a probability of $\sim \frac{1}{2}p_{AS}^2\gamma\eta^3$.

Thus the probability of the desired three-fold coincidence is

$$S = \frac{1}{2}p_{AS}p_0\gamma\eta^3, \quad (8.5)$$

and the probability of the spurious one is

$$N = \frac{1}{4}p_0^2p_s\eta^3\kappa_\phi + \frac{1}{2}p_{AS}^2\gamma\eta^3, \quad (8.6)$$

where ϕ is the initial state, $\kappa_H = 0$ and $\kappa_+ = \kappa_R = 1$. Taking into account the imperfection of entanglement source, one can thus estimate the final fidelity for $|H\rangle$ teleportation by

$$f = \frac{S(1+V)/2 + N/2}{S+N},$$

where $V \sim 0.88$ is the entanglement visibility in the H/V basis. A simple calculation shows that the fidelity is about 0.90, which is in good agreement with our experimental fidelity 0.865 ± 0.017 .

In teleportation of $|+\rangle$ and $|R\rangle$ states, the experimental fidelity are much lower. This is because, on the one hand we have more spurious three-fold coincidence contribution, i.e., $\frac{1}{4}p_0^2p_s\eta^3$. More importantly, the imperfect overlap of the wave packets on the BS, typically around 90% in our experiment, will further reduce the fidelities significantly. However, note that such imperfection has no effect on the $|H\rangle$ teleportation. Taking these into account, a similar calculation shows that the final fidelity for $|+\rangle$ and $|R\rangle$ teleportation is around 0.79, which is well consistent with the experimental results.

8.5 Conclusion

In summary, we have demonstrated quantum teleportation between photonic and atomic qubits. Our experiment has several distinct features: First, different from ionic system, the information carrier (flying photonic qubit) is robust against decoherence and can be easily transmitted over large distances. Second, different from continuous variable system its teleportation fidelity is insensitive to photon losses. In practice, an overall transmission attenuation of 10^{-4} is tolerable with current technology, as demonstrated in recent experiments. Moreover, since the collective state of atomic ensembles is used to encode an atomic qubit, the teleported state can be easily read out in a controllable time for further quantum information applications. Besides being of fundamental interest, most importantly, our memory-built-in teleportation protocol with the direct inclusion of a readable quantum memory enables efficient and scalable connection of quantum networks. However, we would like to mention that, due to the low success probability of teleportation and short lifetime of quantum memory, significant improvements are still needed in order for our method to be really useful for practical applications. The retrieval efficiency can be improved by using high density large atomic ensembles. The long lifetime can be achieved by confining the atoms in an optical trap and exploiting the clock state [125] to store the collective spin excitation .

Chapter 9

Demonstration of a stable atom-photon entanglement source

In this chapter, we propose and demonstrate a novel way to efficiently create a robust entanglement between a memory qubit and a photonic qubit. A single laser beam is used to excite one atomic ensemble, where two different spatial modes of Raman fields are extracted to generate the atom-photon entanglement. With the help of built-in quantum memory, the entanglement still exists after a storage time of $20.5 \mu\text{s}$, which is further proved by the violation of Clauser-Horne-Shimony-Holt type Bell inequality. The atom-photon entanglement can serve as a building block for the robust quantum repeater architecture introduced in chapter 4, and can also be extended to generate high-dimensional atom-photon entanglements.

9.1 Introduction

Quantum communication holds the promise to implement absolutely secure long distance communication by means of quantum cryptography or faithful teleportation of unknown quantum states [6, 141, 142]. However, direct transmission the photons over a long distance suffers from the exponential growing transmission loss and the decoherence. A quantum repeater protocol combining the entanglement swapping, purification and quantum memory provides a possible way to establish high-quality long-distance quantum networks [36, 37]. The resources needed and the time overhead increase polynomially with the communication distance thanks to the nesting purification scheme and the quantum memory.

In a seminar paper, Duan *et al.* proposed a scheme [42] for long distance quantum communication with relatively simple ingredients, i.e., atomic ensembles and linear optics. Recently, significant experimental advances have been achieved along this direction. However, as we analyzed in chapter 3, the DLCZ protocol has two inherent drawbacks, i.e., phase stabilization problem and low entanglement distribution rate, which are severe enough to make a long distance quantum communication impossible. In chapter 4, we

have proposed a robust quantum repeater architecture to overcome the phase stabilization problem by exploiting the two-photon Hong-Ou-Mandel (HOM) interference, which relaxes the long-distance stability requirements by about 7 orders of magnitude. Recently, several experiments have demonstrated the advantage of two-photon HOM interference that the path length instability only need to be kept on the scale of the photon's coherent length [77, 76, 78]. In the robust quantum repeater protocol, two laser beams with fixed relative phase are used to excite two atomic ensembles in order to generate the effective atom-photon entanglement for the local communication node. Only the path length between two ensembles in the local node has to be stabilized to sub-wavelength scale. Some recent works close to the requirements of our protocol have provided the techniques to generate atom-photon entanglement with spin excitation of magnetic sublevels or dual-species atomic ensemble [143, 144]. However, these experiments still have some problems like balancing the excitation between the ensembles or the complexity and efficiency of frequency mixing, which make them impractical for long distance quantum communication.

In this chapter, we present a new approach to generate the effective entanglement between an atomic qubit and a photonic qubit. In contrast to the previous experiments, the atomic ensemble is excited by only one write beam with single frequency, while two anti-Stokes fields in different spatial modes are combined on a polarizing beam splitter and serve as the photonic qubit. The corresponding collective spin excitations in the atomic ensemble represent the atomic qubit. The new approach makes the local phase stabilization simple. The relative phase difference between the two selected modes can be actively stabilized by the local built-in Mach-Zehnder interferometer. Besides, by extending the approach to select more spatial modes of collective excitation, high-dimensional entanglement and hyper-entangled state could be easily generated.

9.2 Experimental scheme

The basic setup of our experiment is shown in Fig. 9.1. A cold ^{87}Rb atomic cloud with temperature about $100 \mu\text{K}$ in the MOT is used as the medium to generate and store the quantum excitation. The two hyperfine ground states $|5S_{1/2}, F = 2\rangle = |a\rangle$ and $|5S_{1/2}, F = 1\rangle = |b\rangle$ and the excited state $|5P_{1/2}, F = 2\rangle = |e\rangle$ form a Λ -type system. After loading the MOT, the atoms are first pumped to initial state $|a\rangle$. A single weak 75 ns write beam illuminates the atomic cloud with a beam waist of $240 \mu\text{m}$ and 10 MHz red-detuned to $|a\rangle \rightarrow |e\rangle$ transition and induces the spontaneous Raman scattering. Two spatial anti-Stokes modes AS_L and AS_R are collected at $\pm 3^\circ$ relative to the propagating direction of the write beam, where L and R denote the different spatial mode. The atom-light system can be described by

$$|\Psi\rangle_m \sim |0_{AS}0_a\rangle_m + \sqrt{\chi_m}|1_{AS}1_a\rangle_m + O(\chi_m), \quad (9.1)$$

where $\chi_m \ll 1$ is the small excitation probability of one collective spin in ensemble m ($m = L, R$), and $\sqrt{\chi_m}|i_{AS}i_a\rangle_m$ denote the i -fold excitation of the anti-Stokes light field and the collective spin in atomic ensemble.

As we discussed in chapter 2, after an anti-Stokes photon is detected in the write

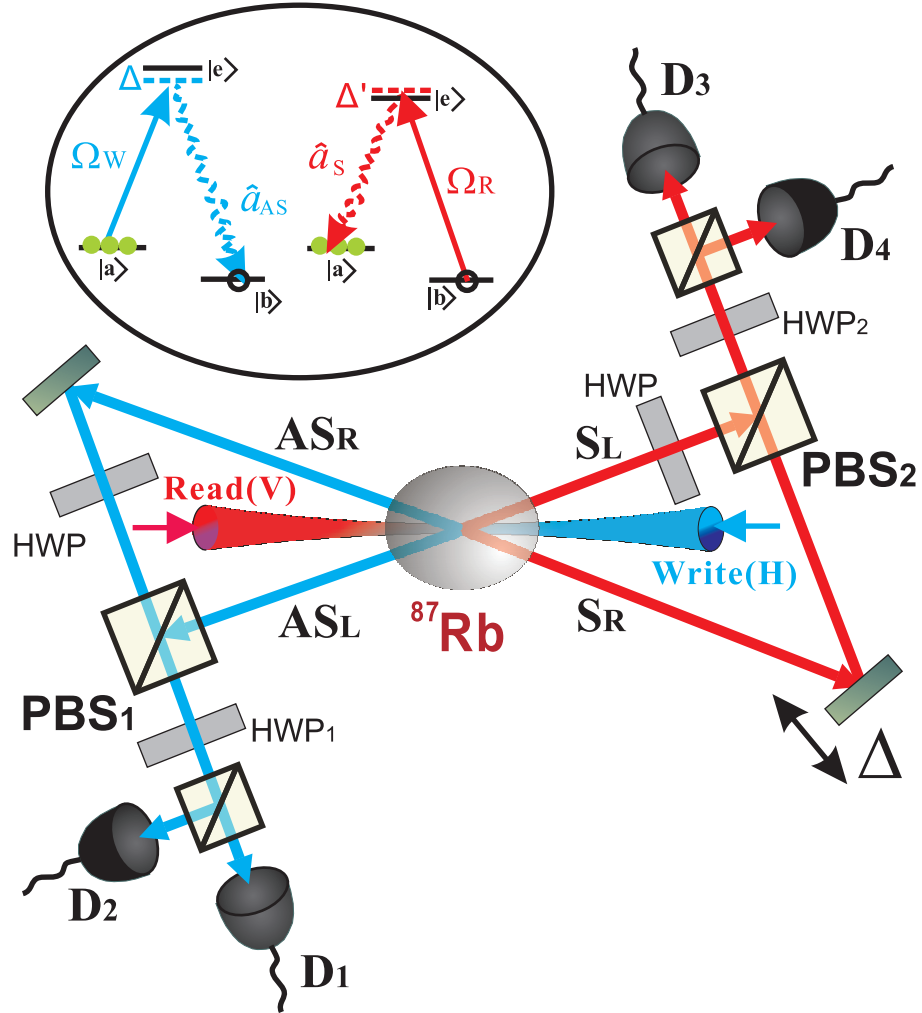


Figure 9.1: Illustration of the experimental scheme and the relevant energy levels of the ^{87}Rb atoms. Cold ^{87}Rb atoms captured by MOT are initially prepared in state $|a\rangle$. A weak write pulse Ω_w with a beam waist of $240\ \mu\text{m}$ illuminates the atom cloud to generate the spin excitation. The spontaneous Raman scattered anti-Stokes field AS_L and AS_R are detected at $\pm 3^\circ$ to the propagating direction of the write beam, with the beam waist of $70\ \mu\text{m}$, defining the spatial mode of the atomic ensembles L and R , respectively. The two anti-Stokes field are combined on a polarizing beam splitter PBS_1 and sent to the polarization analyzer. This creates the entanglement between the polarization of the anti-Stokes field and the spatial modes of spin excitation of atoms in atomic ensemble. To verify the entanglement after a storage time τ , a vertical polarized read pulse counter-propagating with write pulse is applied to retrieve the spin excitation to the Stokes fields S_L and S_R . The polarization of S_L is rotated by 90° , combined with S_R on PBS_2 and sent to the polarization analyzer.

process, a spin wave with wave vector $\vec{k}_{atom} = \vec{k}_W - \vec{k}_{AS}$ will be imprinted in the atomic ensemble, where \vec{k}_{AS} and \vec{k}_W are the wave vector of the anti-Stokes field and write beam, respectively. If there is no decoherence mechanism disturbing the atomic collective state during the storage time τ , the momentum of the collective excitation is kept. When the read pulse is applied to the atomic ensemble, the spin wave will be converted back into a correlated Stokes field satisfying the mode match condition $\vec{k}_S = \vec{k}_R + \vec{k}_W - \vec{k}_{AS}$, where \vec{k}_S and \vec{k}_R are the wave vector of the Stokes field and read light. Under the counter-propagating condition of read and write beams (shown in Fig. 9.1), we have

$$\vec{k}_S \simeq -\vec{k}_{AS}.$$

To characterize the light field, we measure the cross correlation $g_{AS,S}^{(2)}$, which marks the degree of quantum correlation [124], between the anti-Stokes and the Stokes fields. As two anti-Stokes fields AS_L and AS_R are detected at two different spatial modes, two corresponding Stokes fields S_L and S_R can be detected during the retrieve process. Our experimental results show that for the mode-matched fields S_L and AS_L (S_R and AS_R), the cross correlation $g_{AS,S}^{(2)} \gg 1$ when $\chi \ll 1$, which means good quantum correlation between those fields. But for the unmatched fields S_L and AS_R (S_R and AS_L), $g_{AS,S}^{(2)} \sim 1$ and no quantum correlation is observed, which means there is no cross talk between these two different spatial modes. The validity of our new approach is guaranteed by this condition.

We adjust the excitation probabilities to be equal $\chi_L = \chi_R = \chi$. The two anti-Stokes field are then combined on PBS₁ and sent into a polarization analyzer, as illustrated in Fig. 9.1. Neglecting the vacuum state and high order excitations, the effectively entangled states between the photonic and the atomic qubit can be described as

$$|\Psi\rangle = \frac{1}{\sqrt{2}}(|H\rangle|R\rangle + e^{i\phi_1}|V\rangle|L\rangle), \quad (9.2)$$

where $|H\rangle/|V\rangle$ denotes horizontal/vertical polarizations of the single anti-Stokes photon and $|L\rangle/|R\rangle$ denotes single collective spin excitation in ensemble L/R , ϕ_1 is the phase difference between the two anti-Stokes fields.

9.3 Characterization of atom-photon entanglement

9.3.1 Entanglement visibility

To verify the entanglement between the anti-Stokes field and the atomic spin excitation, a strong read pulse with 75 ns close to resonance of $|e\rangle \rightarrow |b\rangle$ transition counter-propagating with the write beam is applied after a controllable time τ to convert the atomic collective excitation back into Stokes fields.

After combining the two Stokes fields on PBS₂ (see Fig. 9.1), the superposition state of anti-Stokes and Stokes fields can be described by

$$|\Psi\rangle_{AS,S} = \frac{1}{\sqrt{2}}|H\rangle_{AS}|H\rangle_S + e^{i(\phi_1+\phi_2)}|V\rangle_{AS}|V\rangle_S, \quad (9.3)$$

where ϕ_2 represent the propagating phase difference between two Stokes fields. In our

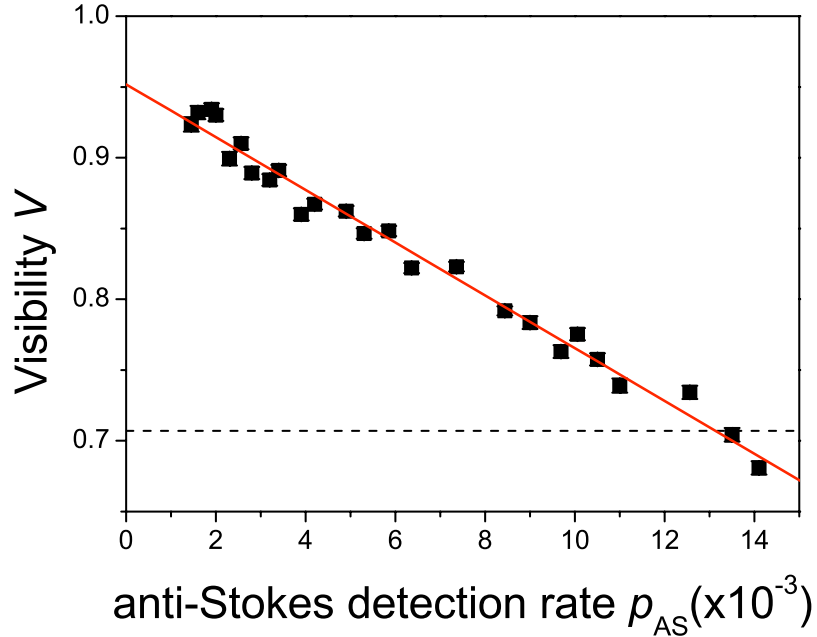


Figure 9.2: Visibility of the interference fringes V between anti-Stokes fields and Stokes fields versus the changing of the detected rate of anti-Stokes field p_{AS} . The solid line is the fit corresponding to Eq. (9.5). The dashed line shows the bound of $1/\sqrt{2}$ which marks the limit to violate the CHSH-type Bell inequality.

experiment, the total phase $\phi_1 + \phi_2$ is actively stabilized via the built-in Mach-Zehnder interferometer and fixed to zero by using the technique introduced in chapter 7. After the active phase stabilization, the short term phase fluctuation is measured to be smaller than $\pi/30$, which guarantees the stability of our experiment.

To characterize the quality of generated atom-photon entanglement, the scaling of entanglement with the excitation probability χ is investigated. To do so, we measure the visibility V of the interference fringes of the coincidence rate between anti-Stokes and Stokes photons for various value of χ with fixed memory time $\tau = 500$ ns. The half wave plate HWP_1 (see Fig. 9.1) is set to $+22.5^\circ$ to measure the anti-Stokes fields under $(|H\rangle + |V\rangle)/\sqrt{2}$ basis and rotate HWP_2 to measure the Stokes fields under different bases. As χ increases, the high order term in Eq. (9.1) can not be neglected. The visibility V can be expressed as the function of cross correlation between the anti-Stokes and Stokes fields

$$V = \frac{g_{AS,S}^{(2)} - 1}{g_{AS,S}^{(2)} + 1}. \quad (9.4)$$

Ideally, the cross correlation can be expressed in terms of the excitation probability as $g_{AS,S}^{(2)} = 1 + 1/\chi$ ($\chi \ll 1$). Considering the overall detection efficiency of the anti-Stokes field η_{AS} , we have the detection rate of the anti-Stokes photon $p_{AS} = \eta_{AS}\chi$. Thus, at the

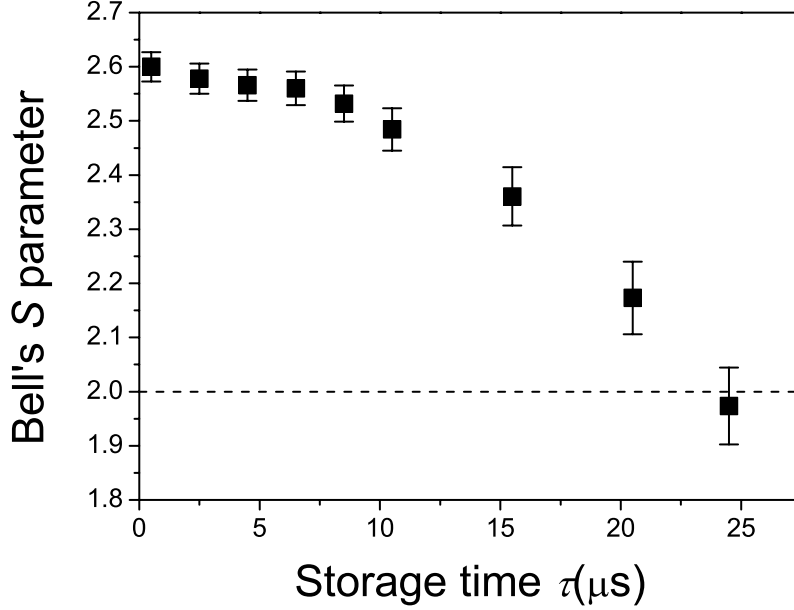


Figure 9.3: The decay of retrieve efficiency and cross correlation $g_{12}^{(2)}$ with the storage time τ . The anti-Stokes detection rate is fixed at $p_{AS} = 2 \times 10^{-3}$. The square dots show the decay process of the retrieve efficiency of the Stokes fields, round dots show the decay of the cross correlation $g_{AS,S}^{(2)}$ between anti-Stokes field and Stokes field.

small excitation rate limit ($\chi \ll 1$), the visibility can be expressed as

$$V = 1 - 2p_{AS}/\eta_{AS}, \quad (9.5)$$

with $\eta_{AS} \sim 8\%$ in our experiment. Figure 9.2 shows the measured visibility V as a function of p_{AS} . As the excitation probability χ decreases, corresponding to decrease of p_{AS} , the visibility V increases as does the degree of entanglement. The solid line is the linear fit for the experiment data. At $p_{AS} \rightarrow 0$, V is near 0.95. This imperfection is mainly caused by the imperfect overlap of the two anti-Stokes fields AS_L and AS_R , the noise of the single photon detectors and the phase fluctuation in the interferometer. As the detection rate p_{AS} increases, the probability of high order excitations increases faster than that of the single excitation. Then the correlation $g_{AS}^{(2)}$ decreases, as well as the visibility. At $p_{AS} < 1.3 \times 10^{-2}$, V is larger than $1/\sqrt{2}$ which is the lower bound of violation of the Clauser-Horne-Shimony-Holt (CHSH) type Bell inequality. Moreover, the cross correlation between different spatial modes, e.g., between AS_L and S_R , is measured to be 1.1 ± 0.5 , which means the crosstalk between the two modes can be neglected.

9.3.2 Storage of entanglement

To further study the storage ability of the atomic ensemble, we characterize the temporal decay of entanglement with storage time τ . Here we measure the decay of S parameter, sum of the correlation function in CHSH inequality, where $S \leq 2$ for any local realistic

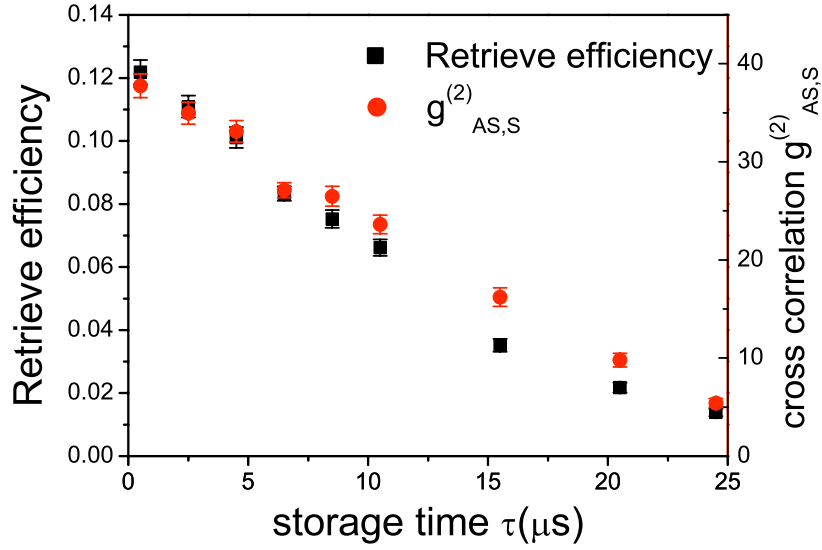


Figure 9.4: Decay of the S parameter in the Bell inequality measurement with the storage time τ . The dashed line shows the classical bound of $S = 2$.

theory with

$$S = |E(\theta_1, \theta_2) - E(\theta_1, \theta'_2) - E(\theta'_1, \theta_2) - E(\theta'_1, \theta'_2)|. \quad (9.6)$$

Here $E(\theta_1, \theta_2)$ is the correlation function, where θ_1 and θ_2 (θ'_1 and θ'_2) are the measured polarization bases of the anti-Stokes field and Stokes field. During the measurement, the HWP₁ and HWP₂ are set to different angles to make the bases settings at $(0^\circ, 22.5^\circ)$, $(0^\circ, -22.5^\circ)$, $(45^\circ, 22.5^\circ)$ and $(45^\circ, -22.5^\circ)$, respectively. The excitation rate χ was fixed to be $p_{AS} = 2 \times 10^{-3}$, and the result of measurement is shown in Fig. 9.3. At the storage time of 500 ns, $S = 2.60 \pm 0.03$, which violates Bell inequality by 20 standard deviations. The violation of the CHSH inequality decreases with the storage time, indicating the decoherence of the entanglement. At storage time $\tau = 20.5 \mu\text{s}$, we still get $S = 2.17 \pm 0.07$, which means the character of quantum entanglement is still well preserved. The decay of S parameter with increasing storage time τ is caused by the residual magnetic field which inhomogeneously broadens the ground state magnetic sublevels. This process can be observed from the decay of the retrieve efficiency and the cross correlation between anti-Stokes and Stokes fields.

As shown in Fig. 9.4, the retrieve efficiency and the cross correlation between anti-Stokes and Stokes field both decrease with increasing the storage time τ . At $\tau = 500$ ns, the overall retrieve efficiency including the transmission loss and the detector efficiency is $12.2 \pm 0.4\%$ and the cross correlation $g_{AS,S}^{(2)} = 38 \pm 1$. At $\tau = 20.5 \mu\text{s}$, the retrieve efficiency and cross correlation decrease to $2.2 \pm 0.1\%$ and $g_{AS,S}^{(2)} = 9.8 \pm 0.7$, respectively. These values are still sufficient to violate the CHSH-type Bell inequality. When τ is longer than $24 \mu\text{s}$, $g_{AS,S}^{(2)} < 6$ makes it insufficient to violate the Bell inequality.

9.4 Discussion

In conclusion, we have proposed and demonstrated a stable atom-photon entanglement with a novel approach. A single write beam and a single atomic ensemble are used to generate the effective entanglement, where two spatial modes of collective excitations defined by the collection modes of anti-Stokes fields serve as a memory qubit. The conservation of momentum during the atom-photon interaction prevent the cross talk between different excited spatial modes. The visibility of the entanglement and violation of the CHSH type Bell inequality are measured to prove the atom-photon entanglement between anti-Stokes photon and collective excitation in atomic ensemble. Also with the help of the built-in quantum memory, the violation of the Bell inequality still exists after $20.5 \mu\text{s}$, corresponding to the time of light propagating 4 km in an optical fiber. That means we have successfully achieved a memory built-in atom-photon entanglement source which can work as a node of the long-distance quantum communication networks. Moreover, if more anti-Stokes modes are selected at different angles, this approach can be easily extended to generate higher dimensional entanglement [145, 29], which is useful in the complex quantum cryptography and quantum computation.

Chapter 10

Entanglement swapping between Light and matter

In this chapter, we report on the realization of entanglement swapping between photonic and atomic qubits. In the experiment, two remote atomic ensembles, each originally entangled with a single photon they emit, are projected into an entangled state by performing a joint Bell-state measurement on the two single photons after passing through a fiber-based optical channel. The entanglement between the atomic ensembles can be stored and later mapped back into an entangled photon pair for further entanglement distribution. The entanglement of the retrieved photon pair is verified by the violation of Bell inequality or by an entanglement witness. Our method is intrinsically phase insensitive and establishes the essential element to realize quantum repeaters with stationary atomic qubits as quantum memories and flying photonic qubits as quantum messengers.

10.1 Introduction

Quantum communication, a method that offers more efficient and more secure ways for the exchange of information in a network, has recently received much experimental attention. Remarkably, large scale quantum communication (on the order of 100 km) has been achieved most recently both in fiber and free space [32, 33, 34]. However, a serious problem occurs beyond 100 km distance scale, mainly due to photon loss in the transmission channel [6]. In quantum communication, the dark counts of single photon detectors can produce errors. Hence, when the probability of a dark count becomes comparable to the probability that a photon is correctly detected, the quantum communication schemes would eventually fail.

To solve the photon loss problem, in a seminal paper Briegel, Dür, Cirac and Zoller [36] introduced the concept of quantum repeaters, where the combination of entanglement swapping and quantum memory could offer efficient ways to extend the achievable distances, provided that the strict precision requirements ($\sim 95\%$) for local operations can be fulfilled. Although entanglement swapping has been experimentally demonstrated, due to the difficulty to integrate a quantum memory, the implementation of quantum repeaters has remained an experimental challenge. In 2001, Duan, Lukin, Cirac and Zoller (DLCZ)

proposed a physical implementation of a quantum repeater by using linear optics and atomic ensembles to incorporate entanglement connection and quantum memory into a single unit [42].

In recent years, following the DLCZ scheme, significant progress has been achieved in the laboratory. Most notably, number-state entanglement between two atomic ensembles has been observed [47], and very recently, asynchronous preparation of number-state entanglement for two pairs of atomic ensembles at two nodes – the basic element of the DLCZ protocol – has also been demonstrated [65]. However, two serious drawbacks make the original DLCZ scheme unlikely to be a realistic solution for long-distance quantum communication. First, the required long term (typically a few hours) sub-wavelength stability of path difference between two arms of a large scale single-photon interferometer spanning the whole communication distance (each arm typically with a length of a few tens km) is very difficult to achieve even with the latest and most sophisticated technology for coherent optical phase transfer. Second, the swapping of number-state entanglement using single-photon interferometer leads to the growth of a vacuum component in the generated state, and to the rapid growth of errors due to multiple emissions from individual ensembles.

As we discussed in chapters 4 and 5, these drawbacks can be overcome by a robust and efficient quantum repeater protocol which is based on two-photon interference and local generation of high quality entangled pair. Since the new architecture uses two-photon interference to generate long-distance entanglement, the stability requirement of path differences is on the order of coherence length of the photons, which is 7 orders of magnitude looser than the DLCZ scheme. Very recently, a first attempt has been made in the entanglement generation of two remote single ions. However, the quantum state of ionic qubits can not be efficiently transferred to a photon for further entanglement connections and the achieved quality of atomic entanglement makes it not directly applicable to quantum communication.

In this chapter, following the robust protocol presented in chapter 4, we report the experimental realization of a fundamental building block of a quantum repeater, with the functions of entanglement generation, entanglement connection and storage. In our experiment, two remote atomic ensembles, each originally entangled with a single photon they emit, are projected into an entangled state by performing a joint Bell-state measurement (BSM) on the two single photons after each passing through a 3 m (or 150 m) fiber. This entanglement between the atomic ensembles can be stored and later mapped back into an entangled photon pair for further information transfer. The entanglement of the retrieved photon pair is verified by the violation of Bell inequality (or an entanglement witness [146]). Our method using two-photon interference is intrinsically phase insensitive to fluctuations of the transmission length. Moreover, vacuum component can be suppressed and no longer a dominant term after a few entanglement connections. Our high precision experimental demonstration surpasses the theoretical limit required for the implementation of quantum repeaters and establishes an essential element to realize robust quantum repeaters with stationary atomic qubits as quantum memories and flying photonic qubits as quantum messengers.

To demonstrate entanglement swapping between light and matter, we follow three steps: implementing two atom-photon entanglement sources, sending the flying qubits – the photons to an intermediate station for a BSM, and verifying the entanglement between the stationary qubits – the two remote atomic ensembles.

Different from previous atom-photon entanglement sources realized with trapped ions [147], single atoms in a cavity [148], or two spatially separated atomic ensembles, we use two collective excitations in different spatial modes of a single atomic ensemble to implement the atom-photon entanglement. The two excitation modes share the same write and read beams, which offers high-quality entanglement and long-term stability.

10.2 Experiment

10.2.1 Atom-photon entanglement source

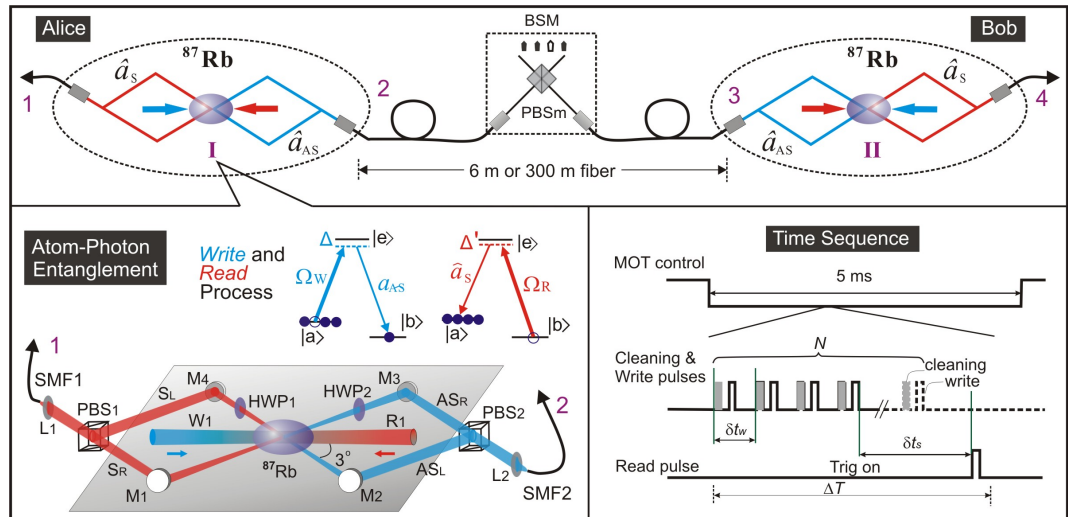


Figure 10.1: The experimental scheme for entanglement swapping. Upper Panel: photons 2 and 3 overlap at BSM through which the entanglement is generated between the two atomic ensembles I and II. Lower-left Panel: energy levels $\{|a\rangle, |b\rangle, |e\rangle\} = \{|5S_{1/2}, F=2\rangle, |5S_{1/2}, F=1\rangle, |5P_{1/2}, F=2\rangle\}$ and the configuration of light beams. Lower-right Panel: the time sequence of the experimental procedure at each site. For 6 m (300 m) fiber connection, there are 250 (200) experiment cycles in 5 ms and ΔT is 16 μs (20 μs) for one cycle which contains $N=10$ ($N=8$) write sequences. The interval between two neighboring write pulses is $\delta t_w = 1 \mu\text{s}$ (1.5 μs) and δt_s is the storage time. Whenever there is a desired coincidence event between photons 2 and 3, the following write sequence is stopped by a feedback circuit and the retrieve process can be started. Abbreviations: PBS–Polarizing beam splitter, HWP–Half-wave plate, M–Mirror, SMF–single mode fiber.

The basic principle is shown in Fig. 10.1. Alice and Bob each have a cold atomic ensemble consisting of about 10^8 ^{87}Rb atoms with temperature $\sim 100 \mu\text{K}$. After 20 ms of loading atoms into their magneto-optical traps (MOT), they switch off the MOTs and start a 5 ms long experiment cycle. At each site atoms are first prepared in the initial state $|a\rangle$, followed by a (50 ns long, $\sim 1 \mu\text{W}$) weak write pulse, which has a beam waist of 240 μm and is 10 MHz red-detuned to $|a\rangle \rightarrow |e\rangle$ transition. Two anti-Stokes fields AS_L and AS_R induced by the write beam via spontaneous Raman scattering are collected at $\pm 3^\circ$ relative

to the propagating direction of the write beam ($70 \mu\text{m}$ waist, $|e\rangle \rightarrow |b\rangle$). This defines two spatial modes of the excitation in the atomic ensemble (L and R), which constitute our memory qubit [149]. The excitation probability (χ_m) of the collective modes m ($m=L; R$) is low ($\chi_m \ll 1$), the state of the atom-photon field can be expressed as,

$$|\Psi\rangle_m \sim |0_{AS}0_a\rangle_m + \sqrt{\chi_m}|1_{AS}1_a\rangle_m + O(\chi_m), \quad (10.1)$$

and $|i_{AS}i_a\rangle_m$ denote the i -fold excitation of the anti-Stokes field and the collective spin in the atomic ensemble.

The two anti-Stokes fields in modes L and R are adjusted to have equal excitation probability and orthogonal polarizations. The two fields are then overlapped at a polarizing beam splitter PBS2 and coupled into single mode fiber with the same collection efficiency. Neglecting the vacuum state and higher order excitations, the entangled state between the atomic and photonic qubits can be described as,

$$|\Psi\rangle_{\text{at-ph}} = \frac{1}{\sqrt{2}} \left(|H\rangle|R\rangle + e^{i\phi_1}|V\rangle|L\rangle \right) \quad (10.2)$$

where $|H\rangle/|V\rangle$ denotes horizontal/vertical polarization of the single anti-Stokes photon and $|L\rangle/|R\rangle$ denotes single collective excitation in ensemble L/R , ϕ_1 is the propagating phase difference between the two anti-Stokes fields before they overlap at PBS2. Physically, the atom-photon entangled state is equivalent to the maximally polarization-entangled state generated by spontaneous parametric down-conversion.

In this way, one can implement two separate and remote atom-photon entanglement sources at Alice (I) and Bob's (II) sites respectively. To make the higher order excitations negligible, a low excitation probability ($\chi \sim 0.01$) is chosen. Due to the imperfect coupling of light modes, the transmission loss, and the inefficiency of single photon detectors, the overall detection efficiency of an emerging anti-Stokes photon (η_{AS}) is around 25%. To check the quality of atom-photon entanglement, a read pulse (50 ns long, $\sim 60 \mu\text{W}$) close to resonance of the $|e\rangle \rightarrow |b\rangle$ transition and counter-propagating with the write beam is applied after a controllable time-delay δt_s to convert the atomic collective excitation back into a Stokes field. Ideally, the retrieve efficiency of the Stokes fields should reach unity. However, various imperfections such as low optical depth of the atomic ensembles and mode mismatching between the write and read pulses lead to a 35% retrieve efficiency. Together with the non-ideal collection and detection efficiency ($\sim 40\%$) of single photon detectors, the overall detection efficiency of the Stokes photon is around 15%. After combining the two retrieved Stokes fields on PBS1 (see Fig. 10.1), the anti-Stokes and Stokes fields are in the following maximally polarization-entangled state

$$|\Psi\rangle_{AS,S} = \frac{1}{\sqrt{2}} \left(|H\rangle_{AS}|H\rangle_S + e^{i(\phi_1+\phi_2)}|V\rangle_{AS}|V\rangle_S \right), \quad (10.3)$$

where ϕ_2 represent the propagating phase difference between two Stokes fields before they overlap at PBS1. In our experiment, the total phase $\phi_1 + \phi_2$ is actively stabilized via the built-in Mach-Zehnder interferometer and fixed to zero.

The quality of the atomic-ensemble-based quantum memory and of the atom-photon

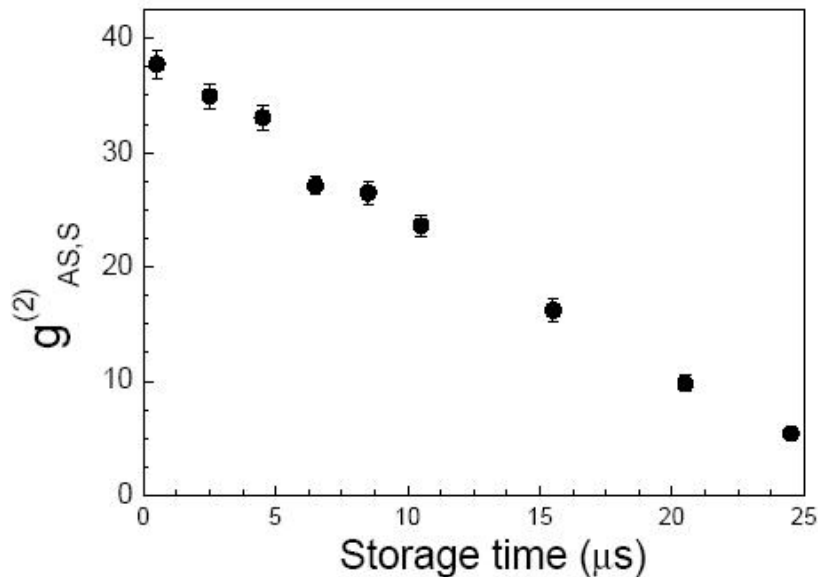


Figure 10.2: The decay of cross correlation $g_{AS,S}^{(2)}$ with the storage time. The detection probability of anti-Stokes photons is fixed at 2×10^{-3} .

entanglement source is investigated by measuring the cross correlation and the violation of CHSH inequality. As shown in Fig. 10.1, the collective excitations in either of the two spatial modes (labeled L for the left one and R for the right) are used as stationary qubits that entangled with photonic qubits. That is, the entangling components are the polarization of the photon and the excitation of the spatial mode. We can investigate the two modes individually addressed by a specific polarization of the emitted single photons from either of the two spatial modes. For example, if vertical/horizontal (V/H) polarized light are chosen at the outputs of PBS1 and PBS2, the property of the L/R mode is being analyzed and can be operated separately.

The intensity correlation function $g_{AS,S}^{(2)}$ can be used to characterize the property of a quantum memory [56]. Theoretically, $g_{AS,S}^{(2)} = 1 + 1/\chi$, where χ is the excitation probability of an atomic ensemble. The interference visibility V between anti-Stokes and Stokes photons can be obtained directly from the correlation function as,

$$V = \frac{g_{AS,S}^{(2)} - 1}{g_{AS,S}^{(2)} + 1}. \quad (10.4)$$

The correlation $g_{AS,S}^{(2)}$ decays along the storage time, which also causes decay of the visibility and therefore the atom-photon entanglement. Shown in Fig. 10.2, $g_{AS,S}^{(2)}$ for one spatial mode becomes lower than 6 when the storage time reaches 24 μs , indicating the visibility is lower than 71%.

The atom-photon entanglement be converted to the entanglement between the Stokes

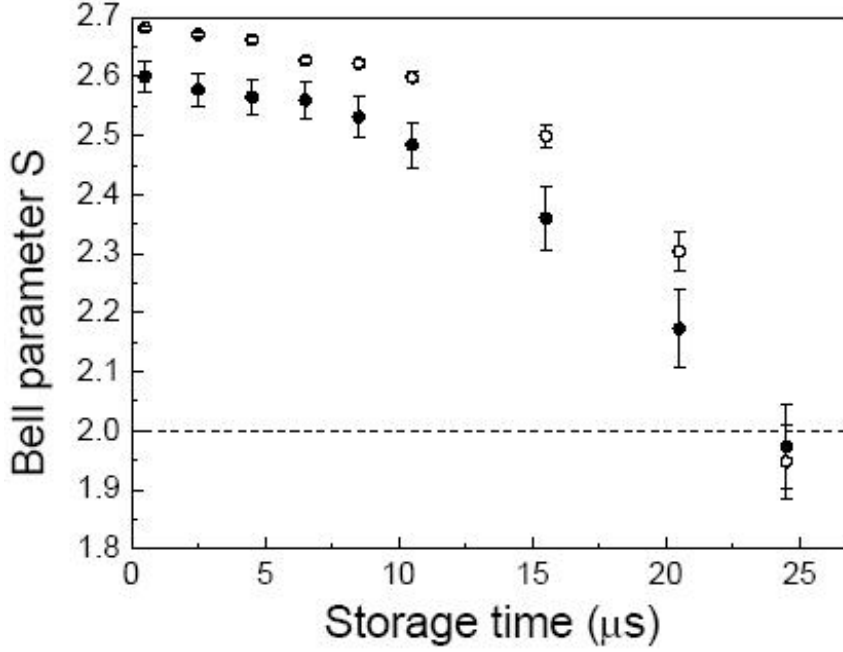


Figure 10.3: Decay of the S parameter in the Bell inequality with the storage time at excitation rate of 2×10^{-3} . The solid squares are the measured data and the circles are calculated from the correlation function $g_{AS,S}^{(2)}$. The dashed line shows the classical bound of $S = 2$.

and anti-Stokes photons. It is verified by the measurement of the Bell inequality,

$$S_{AS,S} = |E(\theta_{AS}, \theta_S) - E(\theta_{AS}, \theta'_S) - E(\theta'_{AS}, \theta_S) - E(\theta'_{AS}, \theta'_S)| \leq 2, \quad (10.5)$$

where $E(\theta_{AS}, \theta_S)$ is the correlation function, in which θ_{AS} and θ'_S (θ_S and θ'_S) are the measured polarization bases of the anti-Stokes (Stokes) photon. During the measurement, the polarization settings are $(0^\circ, 22.5^\circ)$, $(0^\circ, -22.5^\circ)$, $(45^\circ, 22.5^\circ)$ and $(45^\circ, -22.5^\circ)$, respectively. The parameter S can be approximately estimated by $S = 2\sqrt{2}V$. The violation of $S \leq 2$ shows quantum entanglement between the two photons.

Shown in Fig. 10.3, the S parameter is 2.60 ± 0.03 at storage time of 500 ns and goes to lower than 2 at 24 μs . With a time-delay $\delta t_s = 1 \mu s$, the measured polarization correlations of the Stokes and anti-Stokes photons show a strong violation of a CHSH-type Bell inequality, with a visibility of 92%, confirming the high quality of our atom-photon entanglement sources. One can also see that the atom-photon entanglement still survives up to a storage time of $\delta t_s = 20 \mu s$. The small difference between the measured S and the estimated one should arise from the imperfections of the optics.

10.2.2 Entanglement swapping

We now demonstrate the entanglement generation between atomic ensembles I and II via entanglement swapping. As shown in Fig. 10.1, photon 2 from Alice and photon 3 from Bob are both sent through a 3 m optical fiber to an intermediate station for a joint BSM. In the experiment, we chose to analyze the projection onto the Bell state

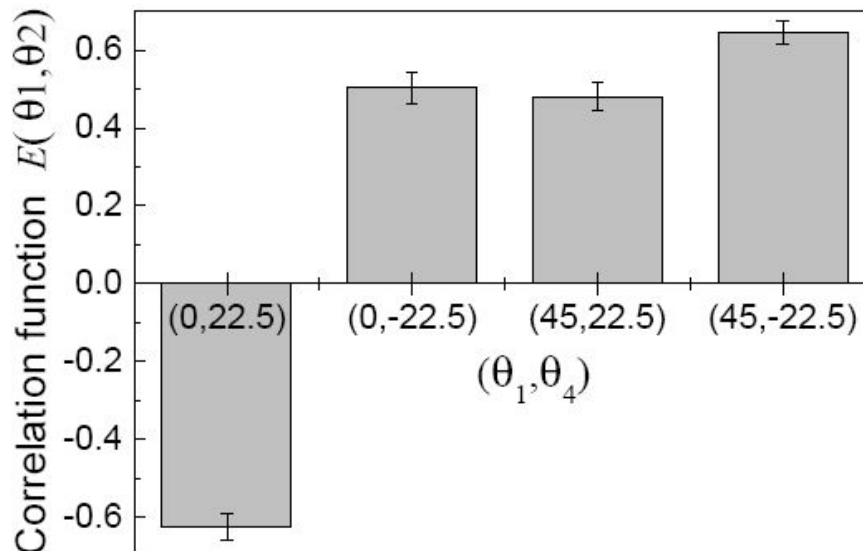


Figure 10.4: Correlation functions of a CHSH-type Bell inequality with the storage time $\delta t_s = 500$ ns. Error bars represent statistical errors, which are ± 1 standard deviation.

$|\Phi^+\rangle_{2,3} = \frac{1}{\sqrt{2}}(|H\rangle_2|H\rangle_3 + |V\rangle_2|V\rangle_3)$, which is achieved by overlapping photons 2 and 3 onto a polarizing beam splitter (PBS) and performing a proper polarization decomposition in the output modes and a subsequent coincidence detection. Conditioned on detecting a $|\Phi^+\rangle_{2,3}$ state at the intermediate station, the two remote atomic ensembles is projected onto an identical entangled state $|\phi^+\rangle_{I,II} = \frac{1}{\sqrt{2}}(|R\rangle_I|R\rangle_{II} + |L\rangle_I|L\rangle_{II})$.

It is worth to note that double excitations in either atomic ensemble I or II will cause false events in the BSM, which reduce the success probability of entanglement swapping by a factor of 2. Experimentally, the false events can be eliminated at the stage of entanglement verification by the four-fold coincidence measurement of photons 1, 2, 3 and 4. Note that, the detection time of photons 1 and 4 is later than that of photons 2 and 3 by an interval δt_s , the storage time in quantum memories. More importantly, as shown in chapter 4 such false events do not affect the applications of our experimental method in quantum repeaters, since the generation of entanglement will be deterministic after a second step of connecting two blocks, where double excitations are washed out automatically.

The established entanglement between atomic ensembles I and II can be verified by converting the atomic spins into an entangled photon pairs 1 and 4, which is in the state $|\Phi^+\rangle_{1,4}$. Here we measure the S parameter in a CHSH-type Bell inequality,

$$S = |E(\theta_1, \theta_4) - E(\theta_1, \theta'_4) - E(\theta'_1, \theta_4) - E(\theta'_1, \theta'_4)|, \quad (10.6)$$

where $E(\theta_1, \theta_4)$ is the correlation function and, θ_1 and θ'_1 (θ_4 and θ'_4) are the measured polarization bases of photon 1 (4). In the measurement, the polarization settings are $(0^\circ, 22.5^\circ)$, $(0^\circ, -22.5^\circ)$, $(45^\circ, 22.5^\circ)$ and $(45^\circ, -22.5^\circ)$, respectively.

The measured correlation functions at a storage time $\delta t_s = 500$ ns are shown in Fig. 10.4, where one can find $S = 2.26 \pm 0.07$, which violates Bell inequality by 3 standard

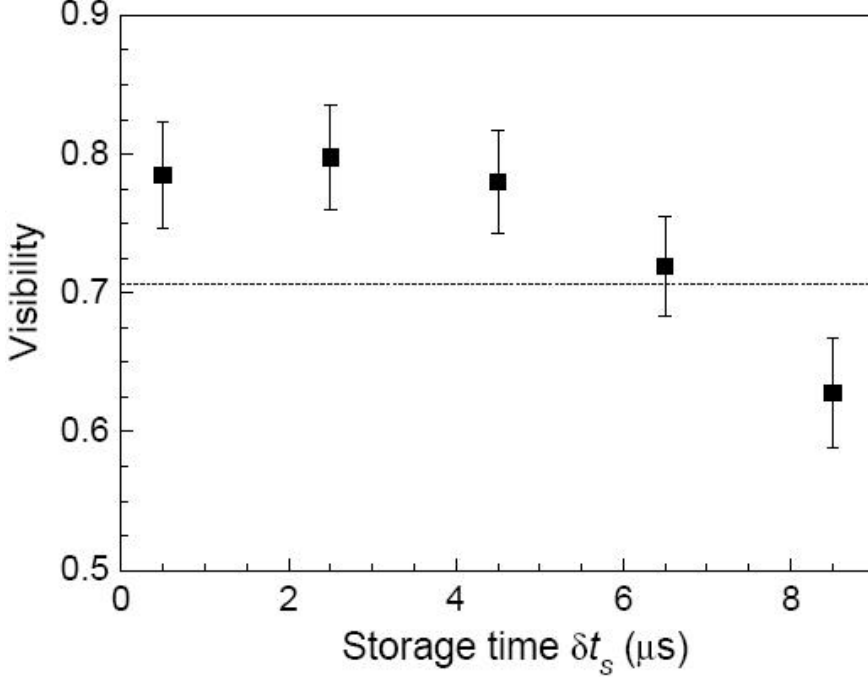


Figure 10.5: Visibility as a function of the storage time with 6 m fiber connection. Black dots are for the visibility and the dashed line shows the threshold for the violation of the CHSH-type Bell inequality. Error bars represent statistical errors, which are ± 1 standard deviation.

deviations. To observe the lifetime of the entanglement between two remote memory qubits, we measure the interference visibility of photons 1 and 4 as a function of the storage time (shown in Fig. 10.5). Up to a storage time of 6 μs , the visibility is still well above the threshold $1/\sqrt{2}$, sufficient for a violation of Bell inequality.

To demonstrate the robustness of our protocol in generation of quantum entanglement between two atomic ensembles over large distances, we change the length of the two connecting fibers from 3 m to 150 m. The anti-Stokes photon is delayed 730 ns and the connection length between Alice and Bob is 300 m. To prove the entanglement between the two atomic ensembles (by converting the collective excitations to photons 1 and 4 respectively), we use an entanglement witnesses, which has a positive expectation value on all separable states. A negative expectation value proves the presence of entanglement. In our case, we use the witness

$$\begin{aligned}
 W = \frac{1}{2} (&|HV\rangle\langle HV| + |VH\rangle\langle VH| + |+-\rangle\langle +-| \\
 &+ |-+\rangle\langle -+| - |\circ\circ\rangle\langle \circ\circ| - |\ominus\ominus\rangle\langle \ominus\ominus|). \quad (10.7)
 \end{aligned}$$

Here $|+\rangle = (1/\sqrt{2})(|H\rangle + |V\rangle)$ and $|-\rangle = (1/\sqrt{2})(|H\rangle - |V\rangle)$ denote two diagonal polarization states, while $|\circ\rangle = (1/\sqrt{2})(|H\rangle + i|V\rangle)$ and $|\ominus\rangle = (1/\sqrt{2})(|H\rangle - i|V\rangle)$ denote the left and right circular polarization states. The above operator can be locally measured by choosing correlated measurement settings that allow detection of the linear, diagonal, and circular polarization for both photons.

After a storage time of 1230 ns (with a 730 ns delay being taken into account), the

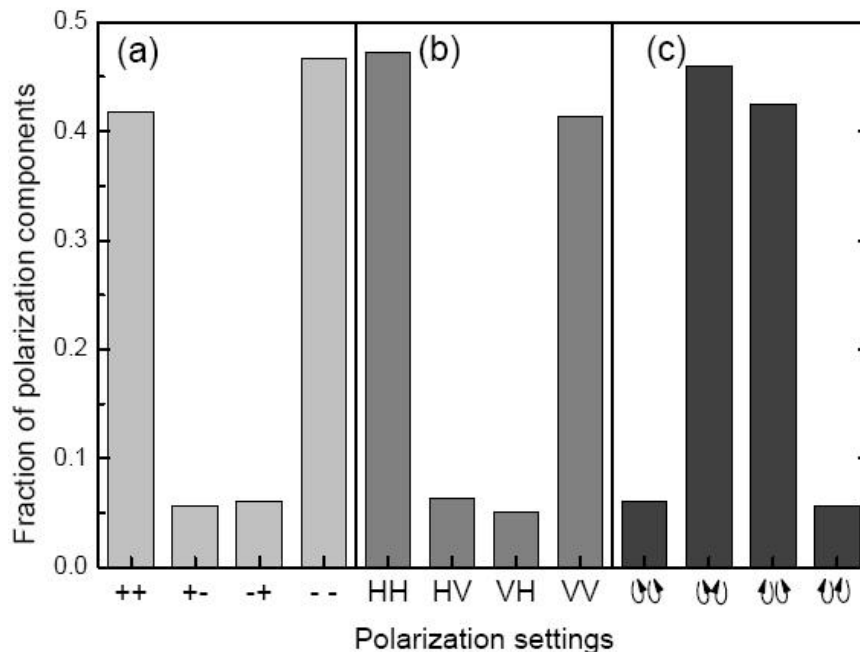


Figure 10.6: Experimental outcomes of the fractions at different polarization settings with 300 m fiber connection. The polarization bases are chosen as (a) $|+\rangle$ and $|-\rangle$, (b) $|H\rangle$ and $|V\rangle$, and (c) $|O\rangle$ and $|C\rangle$ respectively.

two retrieved photons 1 and 4 are sent to their own polarization analyzer. Three series of polarization settings are used and the measured local observables are shown in Fig. 10.6. The resulting $\langle W \rangle = \text{Tr}(W\rho_{\text{exp}}) = -0.33 \pm 0.02$, which is negative by 16 standard deviations and therefore proves the presence of entanglement between the two atomic ensembles. The entanglement swapping can be quantified by the fidelity of the measured state of the atomic ensembles. To determine the fidelity, we write the density matrix of $|\phi^+\rangle_{\text{I,II}}$ in terms of the Pauli matrices:

$$|\phi^+\rangle\langle\phi^+|_{\text{I,II}} = \frac{1}{4} (I + \hat{\sigma}_x\hat{\sigma}_x - \hat{\sigma}_y\hat{\sigma}_y + \hat{\sigma}_z\hat{\sigma}_z). \quad (10.8)$$

The fidelity of final state ρ_{exp} on $|\phi^+\rangle_{\text{I,II}}$ is given by $F = \text{Tr}(\rho_{\text{exp}}|\phi^+\rangle\langle\phi^+|_{\text{I,II}}) = 0.83 \pm 0.02$, well beyond the threshold of 0.78 to violate the CHSH-type Bell inequality for Werner states, demonstrating the success of entanglement swapping between light and matter over a 300 m optical fiber.

10.2.3 Phase stabilization method

Different from the technique in chapter 8, the current method for phase stabilization is simpler and more stable. Generally, the phase in Eq. (10.3) consists of four terms arising from the write beam, the read beam, the anti-Stokes and the Stokes modes. However, since the two spatial modes share the same write and read beams, they always observe a same phase of the write and of the read. So, only the anti-Stokes and Stokes modes contribute to the phase $\phi_1 + \phi_2$, with ϕ_1 (ϕ_2) arising from the path difference between AS_L

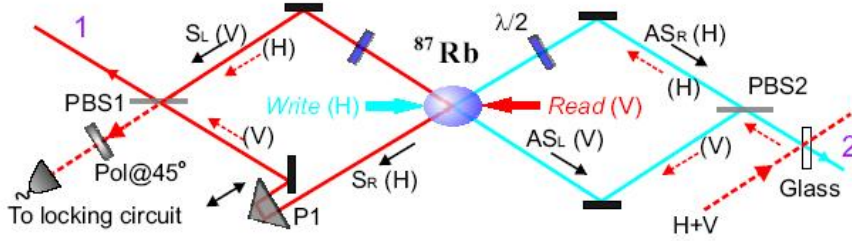


Figure 10.7: Phase stabilization method. The prism P1 is mounted on a piezo and the phase difference between the two arms L and R can be controlled by driving this piezo.

(S_L) and AS_R (S_R). The present setup provides high-quality entanglement and long-term stability by simply locking the phase of $\phi_1 + \phi_2$. This is an obvious advantage compared with the atom-photon entanglement implemented with two atomic ensembles.

To stabilize the phase $\phi_1 + \phi_2$ in Eq. (10.3) actively, a Mach-Zehnder interferometer are used as shown in Fig. 10.7. A locking beam with the frequency of read and polarized at 45° is switched on during the 20 ms MOT loading stage and sent into the interferometer at PBS2 by the weak reflection of a glass slice. This locking beam is overlapped with the two spatial modes L and R . As the anti-Stokes and Stokes light are perpendicularly polarized, the output of the locking beam is from another port of PBS1. After the locking beam goes through a polarizer at 45° , the interference signal can be detected by a photodiode and used to lock the phase $\phi_1 + \phi_2$. During the experimental stage, this locking beam is switched off by an acousto-optical modulator to prevent the collective excitation being destroyed.

Each arm of the Mach-Zehnder interferometer is about 1 meter long in the present setup. With this active locking method, the visibility of the atom-photon entanglement was kept at $\sim 92\%$ during the experiment. In contrast, the visibility became nearly random within a few minutes without the locking.

10.3 Conclusion

In summary, we have successfully demonstrated high precision entanglement swapping between photonic and atomic qubits, a building block for quantum repeaters. Our work using two-photon detection has two distinct advantages over the original DLCZ protocol. First, in our protocol the errors of vacuum component caused by multiple emission are significantly suppressed and remain constant in multi-stage entanglement connection. Second, as opposed to previous DLCZ experiments where wavelength stability over large distances is required, our protocol has the coherence length setting the scale, hence providing a 7 orders of magnitude improvement in stability. Moreover, from the observed high visibilities in our atom-photon and atom-atom entanglement generation, the accuracy of local operations at the BSM station is estimated to be better than 97%, or equivalently an error probability of at most 3%. We emphasize that such a high accuracy achieved in the present experiment fulfills the strict precision requirements of 95% for local operations

of independent photons necessary for quantum repeaters in long-distance quantum communication. The extension of our work to longer chains involves many segments becomes more complicated and is still out of reach for any current system.

For long-distance quantum communication, two quantities need to be improved. One is the lifetime of the quantum memory, the other is the retrieve efficiency. Better compensation of the residual magnetic field and trapping the atoms in “clock states” in optical lattices should improve the lifetime to ~ 1 s. A properly high optical density of the atomic cloud, achieved by the help of traps or by coupling the atoms into an optical cavity, should increase the retrieve efficiency substantially to close to unity [88]. Not only does our work allow immediate experimental investigations of various quantum information protocols, with the aforementioned future improvements entanglement swapping between light and matter would also open the way to long-distance quantum communication.

Chapter 11

Quantum memory with optically trapped atoms

In this chapter, we report the observation of non-classical photon pair generated from a quantum memory with optically trapped atoms. The quantum memory is composed of atoms in the “clock states,” coexisting with other Zeeman components. Normalized cross-correlation function of the photon pair, originating from the collective emission of the atomic assemble, was found to violate the Cauchy-Schwarz inequality for storage times up to $70 \mu\text{s}$. Our observation provides the first evidence for the realization of a quantum memory with optically trapped atoms in the clock states.

11.1 Introduction

A quantum memory is requisite to a quantum repeater for the realization of long-distance quantum communication. In the quantum repeater protocol [36], the transmission channel is divided into several segments with a length comparable to the channel attenuation length. Entanglement is then generated and purified for each segment before being extended to a longer distance by swapping. Once the entanglement is distributed over the transmission channel, it can be employed to teleport any quantum information. The probabilistic nature of the purification [39, 83] thereby necessities storing the already successful segment state in a quantum memory while waiting for the others. Thus, it is clear that a quantum memory with long storage time is essential to achieve scalable quantum communication networks with a realistic (non-exponential) amount of time overhead.

Among various proposed schemes for implementing quantum repeaters, the protocol of Duan-Lukin-Cirac-Zoller (DLCZ) has attracted much attention for experimentalists [42]. The DLCZ protocol is based upon the entanglement between single photons and collective excitations in atomic ensembles, and is thereby within reach of current experimental technology. Following this seminal work, significant progress has been made in recent years. Non-classical correlation between the light generated in the collective emission from an atomic ensemble and the retrieved collective excitation has been observed [43, 44]. Measurement-induced entanglement has also been generated between two atomic ensembles. Most recently, entanglement-based quantum teleportation and entanglement

swapping with a built-in quantum memory has been demonstrated between a photonic and atomic qubits [87, 150].

However, in experiments based upon DLCZ protocol reported thus far, the storage time in a quantum memory is limited presumably due to the inhomogeneous broadening of the ground state from the residual magnetic field, of which the underlying decoherence process has been studied thoroughly in Ref. [60]. One could attempt to compensate the fields by employing pairs of Helmholtz coils. Nevertheless, the diffusion of atoms out of the interaction region eventually imposes restrictions on the storage time to a few hundred microseconds and the distance of quantum communication thereby to only a few tens of kilometers.

In this Letter, we experimentally demonstrate a different sort of quantum memory with optically trapped atoms. Our quantum memory is composed of ^{87}Rb atoms trapped in optical dipole trap in the “clock states,” $|F, m_F\rangle = |1, -1\rangle$ and $|2, 1\rangle$, coexisting with other Zeeman components. Hyperfine coherence time of seconds has been observed for optically trapped atoms [151]. In addition, atoms can be confined in an optical trap for hundreds of seconds [152] without undergoing ballistic expansion out of the interaction region. Furthermore, the differential Zeeman shift of the atoms in the “clock states” has a minimum at a magnetic field of 3.23 G as predicted by the Breit-Rabi formula, and thereby is first-order insensitive to the spatial inhomogeneity and temporal fluctuation of the magnetic field [153]. Coherence time of hundreds of milliseconds between atoms in the clock states has been demonstrated in a magnetically trapped ultracold gas [154]. Thus, with a potential storage time of seconds, our quantum memory is suitable for the realization of a scalable quantum communication network with atomic ensemble.

11.2 Experiment

In our experiment, ^{87}Rb atoms are loaded into an optical trap and optically pumped to the $F = 1$ manifold. A weak write pulse with right circularly polarization (σ^+) then induces spontaneous Raman transition, resulting in a single collective excitation distributed across the atoms conditioned upon the detection of a Stokes field. After a programmable time delay, a read pulse with left circularly polarization (σ^-) illuminates the atomic ensemble and converts the collective excitation into an anti-Stokes field. The normalized cross-correlation function of the two light fields generated by the write and read pulses is measured for various delays and its quantum nature is verified by the violation of Cauchy-Schwarz inequality for storage times up to 70 μs . Our observation provides the first evidence for the realization of a quantum memory with optically trapped atoms in the clock states.

A schematic of our apparatus is shown in Fig. 11.1(a). The experiment begins with a standard MOT. During 2 seconds of loading, 5×10^6 ^{87}Rb atoms are collected from the background vapor with a temperature of about 100 μK . The density and the temperature of the atoms are further optimized to obtain a high transfer efficiency into the optical trap as follows. The density of the MOT is increased by ramping down the repump intensity by a factor of 200 and shifting the cooling light to the red by 35 MHz for a duration of

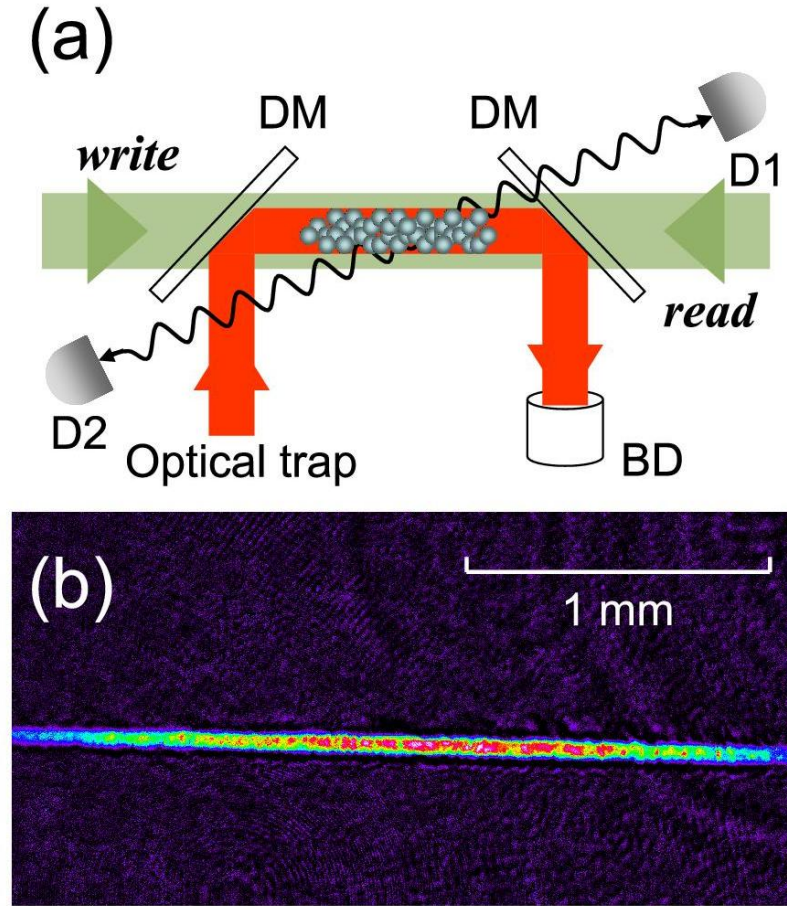


Figure 11.1: A schematic of the experiment. (a) The atoms are confined in an optical trap formed by a red-detuned, focused beam. The optical-trapping beam is overlapped with write and read beams, counter-propagating to each other, on the dichroic mirror (DM) and is blocked by a beam dump (BD) on the other side of the atoms. Single-photon detectors, D1 and D2, are placed at an angle of 3° with respect to the optical trap to detect the Stokes and anti-Stokes fields, respectively. (b) An absorption image of optically trapped atoms.

145 ms. At this point the MOT coils are switched off and molasses cooling is applied for 5 ms, resulting in a peak atomic density of $3 \times 10^{10} \text{ cm}^{-3}$ and a temperature of $10 \mu\text{K}$. Subsequently, the atoms are optically pumped to $|5S_{1/2}, F = 1\rangle$ hyperfine manifold with an efficiency $> 90\%$ by shuttering off the repumping light 3 ms before the cooling light is extinguished. A beam resonant with the $|5S_{1/2}, F = 2\rangle$ to $|5P_{3/2}, F = 3\rangle$ transition blows away any residual atoms in the $|5S_{1/2}, F = 2\rangle$ manifold.

The optical trap is formed by a tightly focused laser beam at $\lambda = 1030 \text{ nm}$ with a $1/e^2$ radius of $36 \mu\text{m}$. The beam is left on during the experimental cycles at 6.5 W, corresponding to a (radial, axial) trapping frequencies of $2\pi \times (2 \text{ kHz}, 10 \text{ Hz})$ and a trap depth of $k_B \times 450 \mu\text{K}$. For typical operating conditions, 2×10^5 atoms are loaded into the optical trap with a temperature of $20 \mu\text{K}$, a (radial, axial) rms radius of ($5.5 \mu\text{m}$, 0.85 mm), a peak density of 10^{12} cm^{-3} , and a $1/e$ trap lifetime of 20 sec. An absorption image of optically trapped atoms, taken by a charge-coupled-device camera, is shown in Fig. 11.1(b).

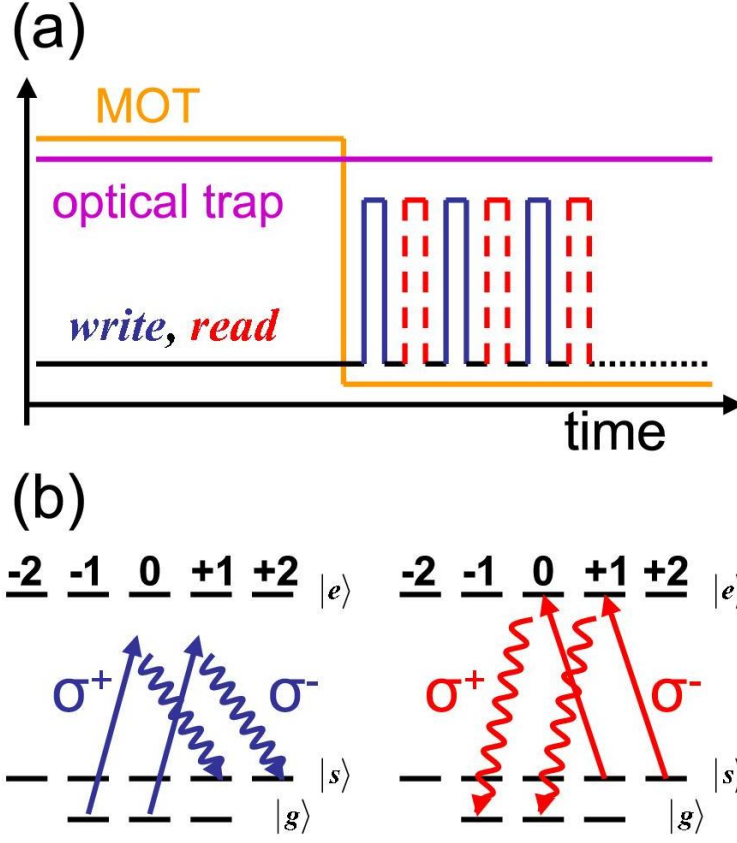


Figure 11.2: Time sequence of one experimental cycle and the relevant atomic transitions in the experiment. (a) After the MOT is switched off, the atoms are loaded into an optical trap with a transfer efficiency of $\sim 5\%$. Typically, 10000 write and read pulses are employed during a single experimental cycle, with a pulse length of 100 ns and 500 ns respectively. (b) The left and right diagrams illustrate the atomic levels involved in the write and read processes, where $|g\rangle = |5S_{1/2}, F = 1\rangle$, $|s\rangle = |5S_{1/2}, F = 1\rangle$, and $|e\rangle = |5P_{3/2}, F = 2\rangle$. The relevant Zeeman states are the $|F, m_F\rangle = |1, -1\rangle, |2, 1\rangle$ (clock states) and $|F, m_F\rangle = |1, 0\rangle, |2, 2\rangle$ (non-clock states).

The time sequence of one experimental cycle and the relevant atomic transitions are shown in Fig. 11.2, where $|g\rangle = |5S_{1/2}, F = 1\rangle$, $|s\rangle = |5S_{1/2}, F = 1\rangle$, and $|e\rangle = |5P_{3/2}, F = 2\rangle$. After the molasses cooling, untrapped atoms are allowed to free fall for 30 ms and a bias field at ~ 3.23 G is switched on in the propagating direction of the optical trap, z . The optically trapped ensemble is then illuminated by a weak, off-resonant write pulse for 100 ns, which induces Raman transition into $F=2$ manifold. The write beam, with a $1/e^2$ radius of $250 \mu\text{m}$ and a peak intensity of 50 mw/cm^3 , is detuned 50 MHz below the $|g\rangle$ to $|e\rangle$ transition in addition to a light shift of 18 MHz in the optical trap.

Conditional upon the detection of a Raman (Stokes) photon at the single-photon detector D1, a collective atomic superposition state

$$|1_a\rangle = \frac{1}{\sqrt{N}} \sum_{j=1}^N |g \cdots s_j \cdots g\rangle e^{-i(\mathbf{k}_1 - \mathbf{k}_W) \cdot \mathbf{r}_j}, \quad (11.1)$$

is generated in the ensemble, where N is the atom number, \mathbf{k}_1 (\mathbf{k}_W) is the wave vector

of the Stokes (write) photon, and \mathbf{r}_j is the position of the j -th atom. The probability of generating a Stokes photon with σ^- polarization within the solid-angle of our detection system, $d\Omega \sim 4 \times 10^{-5}$, is measured to be $p_c \sim 0.002 \ll 1$ in each write pulse which contains approximately 10^5 photons in the region of the atoms. With such a low excitation rate, the joint state of the atomic collective mode and the chosen Stokes mode can be thereby approximated by $|\phi\rangle = |0_a\rangle|0_s\rangle + \sqrt{p_c}|1_a\rangle|1_s\rangle$, where $|i_a\rangle$ and $|i_s\rangle$ denote i quantum of excitations in the atomic collective and Stokes modes. The collection mode of the detector D1 has a $1/e^2$ radius of $75 \mu\text{m}$ with an angle of 3° to the z -axis, covering the entire region of the atomic ensemble. At the front of detector D1, a Fabry-Perot etalon with a transmission efficiency $> 90\%$ at the frequency of Stokes light is employed to filter out the straight light from the write and the optical trap beams.

The collective excitation in the ensemble is subsequently converted into a specific anti-Stokes field with high probability by illuminating a read pulse resonant with the $|s\rangle$ to $|e\rangle$ transition and mode-matched to the write beam in a counter-propagating configuration. The resulting joint state of Stokes and anti-Stokes fields is thus,

$$|\varphi\rangle = |0_s\rangle|0_{AS}\rangle + \sqrt{p_c}|1_s\rangle|1_{AS}\rangle, \quad (11.2)$$

where $|i_s\rangle$ and $|i_{AS}\rangle$ correspond to the detection of i Stokes and anti-Stokes photons. The anti-Stokes photon is detected with σ^+ polarization by the detector D2, which is mode-matched to the detector D1 with a coupling efficiency of 80%.

The quantum nature of the correlation shown in Eq. 11.2 is probed by means of the measurements of the normalized cross-correlation function, $g_{1,2} = p_{1,2}/p_1p_2$, of the two fields, where $p_{1,2}$ is the joint probability of detecting one photon in both fields, and p_1 (p_2) is the probability of detecting a Stokes (anti-Stokes) photon. For classical light fields, $g_{1,2}$ is constrained by the Cauchy-Schwarz inequality, $g_{1,2}^2 \leq g_{1,1}g_{2,2}$ [56]. In our experiment, $g_{1,1} = g_{2,2} = 2$, measuring $g_{1,2} > 2$ is thereby an indication of non-classical correlation.

We investigate the promising feature of atoms in the clock states against the decoherence, due to the inhomogeneous broadening of the ground state, by measuring $g_{1,2}(t)$ for various storage times in the quantum memory as shown in Fig. 11.3(a). Non-classical correlation for storage times up to $70 \mu\text{s}$ is observed. The measured $1/e$ lifetime of $65(5) \mu\text{s}$ is two-fold longer than what has been obtained in the previous experiments. Fig. 11.3(b) shows another experiment with improved compensation of the earth magnetic field. Here, two different time scales of decay have been observed. This is because, in the write process, both $|F, m_F\rangle = |1, -1\rangle \rightarrow |2, 1\rangle$ (clock states) and $|F, m_F\rangle = |1, 0\rangle \rightarrow |2, 2\rangle$ (non-clock states) transitions contribute to the detection of a Stokes photon with σ^+ polarization; in the read process, the corresponding collective excitations of both transitions also participate in the detection of an anti-Stokes photon with σ^- polarization. Thus, the observed fast and the subsequent slow decay times are due to the atoms in the non-clock states and clock states respectively. The measured $1/e$ lifetime $\tau_f = 10(1) \mu\text{s}$ of the fast decay is found to be similar to the values measured in. Note that, in the experiment shown in Fig. 11.3 (a), the compensation of the earth magnetic field is misaligned, resulting in a rapid decoherence between the atoms not in the clock states. Thus, only the atoms in the clock states contribute to the measured intensity correlation.

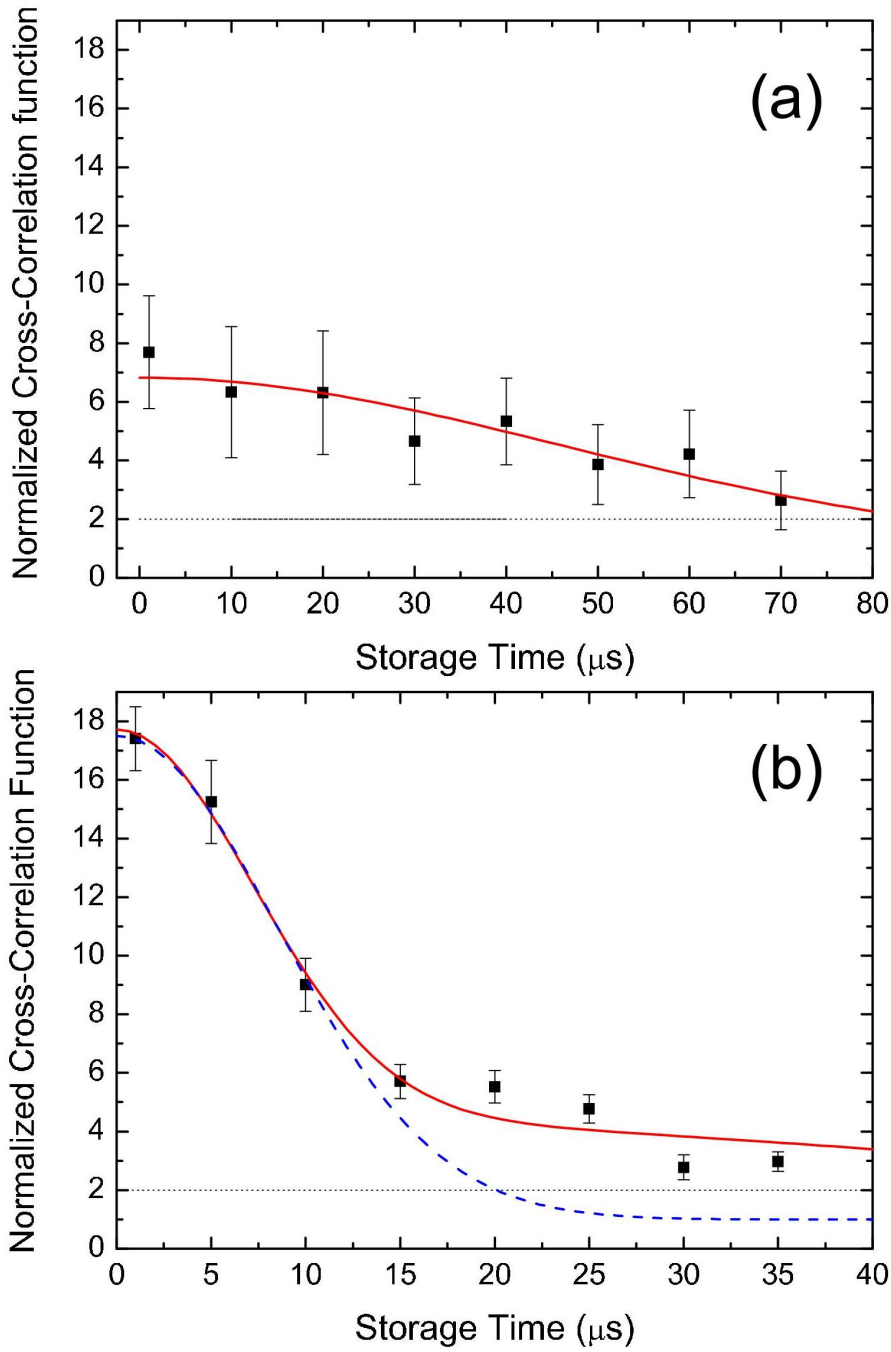


Figure 11.3: Normalized cross-correlation function $g_{1,2}$ of the Stokes and anti-Stokes fields as a function of storage times. (a) Non-classical correlation is observed for storage times up to 70 μs . The curve is a Gaussian fit with a $1/e$ lifetime of 65 μs . (b) With an improved compensation of the earth magnetic field, two different time scales of the decay have been observed. The fast decay with $\tau_f = 10 \mu\text{s}$ corresponds to the atoms in the non-clock states and the subsequent slow decay is due to the atoms in the clock states. The dashed and solid curves are the Gaussian fits with one and two time constants, respectively. The error bars represent the statistical error. The dotted line illustrates the classical limit, $g_{1,2} = 2$.

The thermal motion of the atoms after interacting with the Stokes field, but not yet with the anti-Stokes field, induces decoherence of the collective state through the velocity-dependent phase factors in Eq. 11.1, resulting in an exponential decay of the retrieve efficiency, $e^{-(t/\tau_{tm})^2}$ with $\tau_{tm} = 1/(v\Delta k)$, v the velocity of the atoms, and $\Delta k = |\mathbf{k}_1 - \mathbf{k}_W|$. As the atoms in the optical trap are weakly confined in the longitudinal direction, only the atomic motion in the radial direction is relevant. In our experiment, $\Delta k \sim 386 \text{ mm}^{-1}$ and $v \sim (k_B T/m)^{1/2} \sim 44 \text{ } \mu\text{m/s}$, where k_B is the Boltzmann's constant and $T(m)$ is the temperature (mass) of the atoms. Thus, $\tau_{tm} \sim 60 \text{ } \mu\text{s}$, which is in good agreement with the $1/e$ lifetime observed for the atoms in the clock states.

11.3 Discussion

In conclusion, we have realized a quantum memory with potential storage-time of seconds. The quantum memory comprises of optically trapped ^{87}Rb atoms in the clock states, coexisting with other Zeeman components. Non-classical cross-correlation between the photon pair generated from the quantum memory is observed to violate the Cauchy-Schwarz inequality for storage times up to $70 \text{ } \mu\text{s}$. Our observation provides the first evidence for implementing a quantum memory with optically trapped atoms in the clock states. The observed storage time is currently limited by the atomic motion in the optical trap. With an ensemble at lower temperature, a longer storage time could be achieved. For example, by employing evaporative cooling in a crossed optical trap [155], a temperature of submicro-Kelvin can be obtained, which will greatly reduce the atomic motion and thereby extend the storage time to milliseconds. Alternatively, one could confine the atoms to the Lamb-Dicke regime [156] using an optical lattice and completely “freeze” the atomic motion. Finally, we note that the inhomogeneous light shift in the red-detuned optical trap can be improved by confining the atoms in a blue-detuned optical box [157] or a “donut” trap [158].

Chapter 12

A long-lived quantum memory for scalable quantum networks

In this chapter, we demonstrate an atomic-ensemble-based quantum memory with millisecond storage time for single collective excitation. A new decoherence mechanism, dephasing of the spin wave induced by atomic random motion, is revealed when the effect of residual magnetic field is suppressed. By exploiting the “clock state”, and generating a long wavelength spin wave via changing the detection configuration, a storage time of 1 ms is achieved. The quantum memory with a long coherence time demonstrated in this work can be used to construct long-lived quantum nodes for scalable quantum networks, as well as to study spin wave at single quanta level.

12.1 Introduction

Scalable quantum information processing critically depends on the capability of storage of a quantum state or entanglement [18, 36]. In particular, a storable and retrievable quantum memory with long coherence time is of crucial importance to the atomic-ensemble-based long-distance quantum communication. Following the protocol proposed by Duan *et al.* [42] and the subsequent improved schemes [48, 66, 67], significant progresses have been accomplished, including conditional manipulation of the stored excitation in one atomic ensemble [45, 46, 88] and two atomic ensembles [75, 77, 78, 92], demonstration of memory-built-in quantum teleportation [87], and realization of a building block of the quantum repeater [65, 150]. In these experiments, the atomic ensembles serve as the storable and retrievable quantum memory, where the collective state is used to store qubits and entanglement.

Despite the advances achieved in manipulating atomic ensembles, the development of scalable quantum networks is hindered by the short coherence time of the quantum memory. For example, to directly establish entanglement between two memory qubits over 100 km, one needs a memory with a storage time of at least 300 μs , while the longest

storage time reported so far is on the order of $10 \mu\text{s}$ [45, 46, 88, 149].

It is believed that the short coherence time is mainly caused by the residual magnetic field [45, 46, 78]. Thereby, storing the collective state in the superposition of the magnetic-field-insensitive state, i.e. “clock state” [125], is suggested to inhibit this decoherence mechanism [60]. A simple calculation using the Breit-Rabi formula shows that the lifetime of the collective excitation stored in the “clock state” is on the order of seconds [61], which is enhanced by about 5 orders of magnitude.

Motivated by this idea, in this chapter, we explore the advance of the “clock state” to prolong the coherence time of the quantum memory. However, we find that, the decoherence caused by the magnetic field is not the only principal mechanism. There is another dominating mechanism, the dephasing of the spin wave (SW) induced by atomic random motion, which has not been noticed before. By exploiting the “clock state”, together with increasing the wavelength of the SW to suppress the dephasing, we succeed in extending the coherence time of the quantum memory from $10 \mu\text{s}$ to 1 ms. Our work makes substantial progress towards long-distance quantum communication, and may have potential applications in precision measurement.

12.2 Experiment

The architecture of our experiment is depicted in Fig. 12.1A and 12.1B. A cold ^{87}Rb atomic ensemble in a magneto-optical trap (MOT) at a temperature of about $100 \mu\text{K}$ serves as the quantum memory. The two ground states $|g\rangle$ and $|s\rangle$, together with the excited state $|e\rangle$ form a Λ -type system. A bias magnetic field of about 3 G is applied along the axial direction to define the quantization axis. Note that there are three pairs of “clock states” for the ground states of ^{87}Rb atom, i.e. $(|1, 1\rangle, |2, -1\rangle)$, $(|1, 0\rangle, |2, 0\rangle)$, and $(|1, -1\rangle, |2, 1\rangle)$, where we define $|i, j\rangle = |5S_{1/2}, F = i, m_F = j\rangle$. In a timescale of milliseconds, we can use any of them to store the collective excitation, because the decoherence of the “clock states” caused by magnetic field is negligible. In our experiment, we prepare the atoms in $|1, 0\rangle$ to exploit the clock state ($|g\rangle = |1, 0\rangle$, $|s\rangle = |2, 0\rangle$). An off-resonant σ^- polarized write pulse with wave vector \mathbf{k}_W is applied to the atomic ensemble along the axial direction, inducing spontaneous Raman scattering. The Stokes photon with σ^- polarization and wave vector \mathbf{k}_S is collected at an angle of $\theta = 3^\circ$ relative to the write beam, as in most of the previous experiments [45, 65, 77, 78, 92, 149]. The beam waist of the detection mode is about $100 \mu\text{m}$ in the atomic ensemble. Conditional on detecting a Stokes photon, a collective excited state or a SW is imprinted in the atomic ensemble [42], described by

$$|\psi\rangle = \frac{1}{\sqrt{N}} \sum_j e^{i\Delta\mathbf{k}\cdot\mathbf{r}_j} |g\dots s_j\dots g\rangle, \quad (12.1)$$

with $\Delta\mathbf{k} = \mathbf{k}_W - \mathbf{k}_S$ the wave vector of the SW, and \mathbf{r}_j the coordinate of the j -th atom. After a controllable delay δt , a strong σ^+ polarized read light, counter-propagating with the write light, converts the collective excitation into an anti-Stokes photon, which is spatially mode-matched with the Stokes photon from the opposite direction. The Stokes (anti-Stokes) photon and the write (read) light have the same polarization, and are spatially

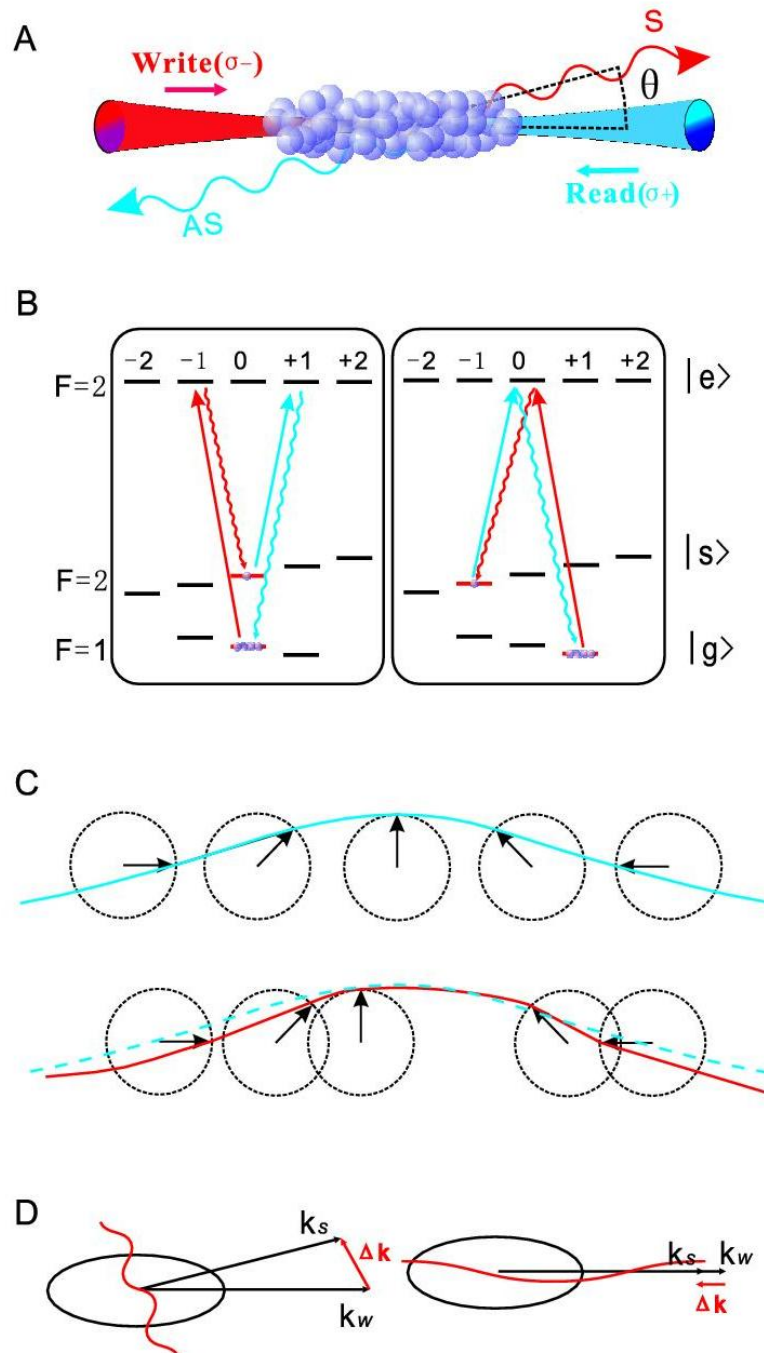


Figure 12.1: (A) Schematic view of the experiment. A weak σ^- polarized write pulse is applied to generate the SW and Stokes photon via spontaneous Raman transition. The Stokes photon are detected at an angle of θ relative to the write beam. After a controllable delay, a strong σ^+ polarized read light converts the SW into an anti-Stokes photon. (B) The structure of atomic transitions (^{87}Rb) under a weak magnetic field. The left panel corresponds to the experiment with $(|1,0\rangle, |2,0\rangle)$. The right one corresponds to the experiment with $(|1,1\rangle, |2,-1\rangle)$. (C) Illustration of the SW dephasing induced by atomic random motion. The blue curve represents the SW initially stored in the quantum memory. The perturbed SW is represented by the red curve. (D) The wavelength of the SW can be controlled by changing the detection configuration.

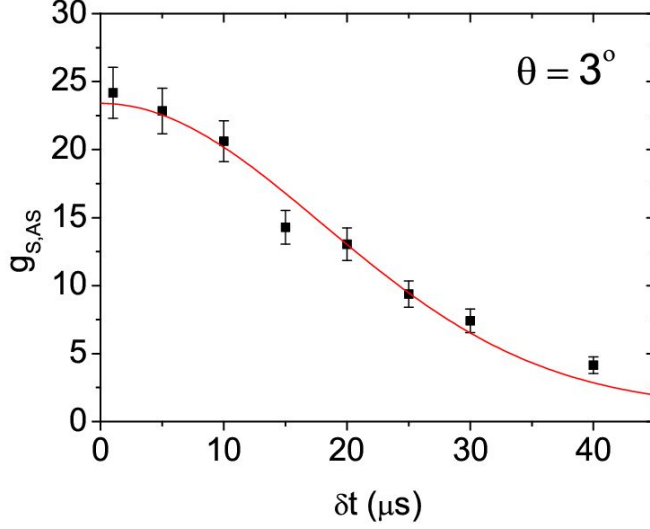


Figure 12.2: The cross correlation $g_{S,AS}$ versus the storage time δt for $(|1,0\rangle, |2,0\rangle)$ at $\theta = 3^\circ$. The data are fitted by using $g_{S,AS}(\delta t) = 1 + C \exp(-\delta t^2/\tau_D^2)$. Our data give a lifetime of $\tau_D = 25 \pm 1 \mu\text{s}$, which is much less than the theoretical estimation for the “clock state”. Error bars represent statistical errors.

separated.

In the experiment, to evaluate the coherence time of the quantum memory, we measure the cross correlation $g_{S,AS} = p_{S,AS}/(p_S \cdot p_{AS})$ as a function of the delay, with p_S (p_{AS}) the probability of detecting a Stokes (anti-Stokes) photon and $p_{S,AS}$ the coincident probability between the Stokes and anti-Stokes channels. The time dependent cross correlation can be described by [46]

$$g_{S,AS}(\delta t) = 1 + C\gamma(\delta t), \quad (12.2)$$

with C a constant determined by the excitation probability and background noise, and $\gamma(\delta t)$ the time dependent retrieval efficiency.

The experimental result is shown in Fig. 12.2, where the data are fitted by using $g_{S,AS}(\delta t) = 1 + C \exp(-\delta t^2/\tau_D^2)$, with τ_D the lifetime of the collective state. Out of expectation, our data only give a lifetime of $\tau_D = 25 \pm 1 \mu\text{s}$, which is far from the theoretical predication for the “clock state”. One might think this is caused by the atoms moving out of the interaction region. However, the decoherence due to loss of atoms gives a lifetime of a few hundred microseconds under the present condition. This can be estimated by calculating the average time for the atoms flying out of the pencil shaped interaction region, where the thermal motion in radial direction dominates. At temperature T , an atomic cloud with a cross section radius r_0 expands according to $r^2(\delta t) = r_0^2 + v_r^2 \delta t^2$, with the average speed in radial direction $v_r = \sqrt{\frac{2k_B T}{m}}$. The retrieval efficiency can be given by $\gamma(\delta t) = r_0^2/r^2(\delta t) = 1/(1 + \frac{v_r^2}{r_0^2} \delta t^2)$. Thereby, when $\gamma(\tau_L) = 1/e$, only $1/e$ of the atoms remain in the interaction region, giving a lifetime of $\tau_L \simeq \frac{1.31 r_0}{v_r}$. For $r_0 = 100 \mu\text{m}$ as the

waist of the detection mode and $T = 100 \mu\text{K}$, we have $\tau_L = 950 \mu\text{s}$, which is much longer than our result.

We carefully analyze the decoherence of the quantum memory and find that the short lifetime could be explained by the dephasing of the SW induced by atomic random motion [159]. This decoherence mechanism is in fact a dominating decoherence mechanism in this experiment and most of the previous experiments [45, 65, 77, 78, 92, 149]. However, it has not been noticed before.

As shown in Fig. 12.1C, assume a SW is stored in the atomic ensemble and will be retrieved out after a time delay δt . In this interval, each atom randomly moves from one point to another along the wave vector direction. The internal states or the spin of the atoms are conserved since collisions can be safely neglected at a low temperature and density. However, the atomic motion leads to a perturbation on the phase of the SW. Consequently, the projection of the perturbed SW on the original one gradually decreases as the delay of the retrieve becomes longer. In other words, the atomic random motion leads to a random phase fluctuation in the SW and thus causes decoherence. The timescale of the dephasing can be estimated by calculating the average time needed for the atoms to cross $\frac{1}{2\pi}$ of the wavelength of the SW, giving a lifetime of $\tau_D \sim \frac{\lambda}{2\pi v_s}$, with $v_s = \sqrt{\frac{k_B T}{m}}$ the one dimensional average speed and $\lambda = \frac{2\pi}{\Delta k}$ the wavelength of the SW.

The dephasing can also be directly calculated as follows. Assume the j -th atom moves to $\mathbf{r}_j(\delta t) = \mathbf{r}_j + \mathbf{v}_j \delta t$ after a storage time of δt . The collective state or spin wave (SW) freely evolves to

$$|\psi_D\rangle = \frac{1}{\sqrt{N}} \sum_j e^{i\Delta\mathbf{k}\cdot\mathbf{r}_j(\delta t)} |g\dots s_j\dots g\rangle, \quad (12.3)$$

where we have neglected the effect of magnetic field for simplicity. The retrieval efficiency is given by the overlap between the original SW and the perturbed one,

$$\gamma(\delta t) \sim |\langle\psi|\psi_D\rangle|^2 = \left| \frac{1}{N} \sum_j e^{i\Delta\mathbf{k}\cdot\mathbf{v}_j \delta t} \right|^2 = \left| \int f(\mathbf{v}) e^{i\Delta\mathbf{k}\cdot\mathbf{v} \delta t} d\mathbf{v} \right|^2 \quad (12.4)$$

with $f(\mathbf{v})$ the velocity distribution. Assume $f(\mathbf{v}) \sim e^{-\frac{m\mathbf{v}^2}{2k_B T}}$ is a Boltzmann distribution at temperature T . Integrating over all possible velocity, we obtain $\gamma(\delta t) \sim e^{-\delta t^2/\tau_D^2}$, with the lifetime $\tau_D = \frac{1}{\Delta k v_s}$.

In our case, there is an angle θ between \mathbf{k}_W and \mathbf{k}_S , and thus we have $\Delta k = |\mathbf{k}_W - \mathbf{k}_S| \simeq k_W \sin \theta$. For $\theta = 3^\circ$, a simple calculation gives $\lambda = 15 \mu\text{m}$ and then $\tau_D = 25 \mu\text{s}$, which is consistent with the experimental result.

The above analysis also suggests that in order to suppress this dephasing and extend the storage time, we have to increase the wavelength of the SW by decreasing the detection angle (see Fig. 12.1D). Thereby, we reduce the angle by choosing $\theta = 1.5^\circ$, 0.6° , and 0.2° . Note that, for $\theta = 0.2^\circ$, the two beams with the same polarization can not be spatially separated, and thereby we use another ‘‘clock state’’ ($|g\rangle = |1, 1\rangle$, $|s\rangle = |2, -1\rangle$) by preparing the atoms in $|1, 1\rangle$. In this case, the Stokes (anti-Stokes) photon is σ^+ (σ^-) polarized. The write (read) and Stokes (anti-Stokes) lights have orthogonal polarizations and are separated by a Glan-Laser prism.

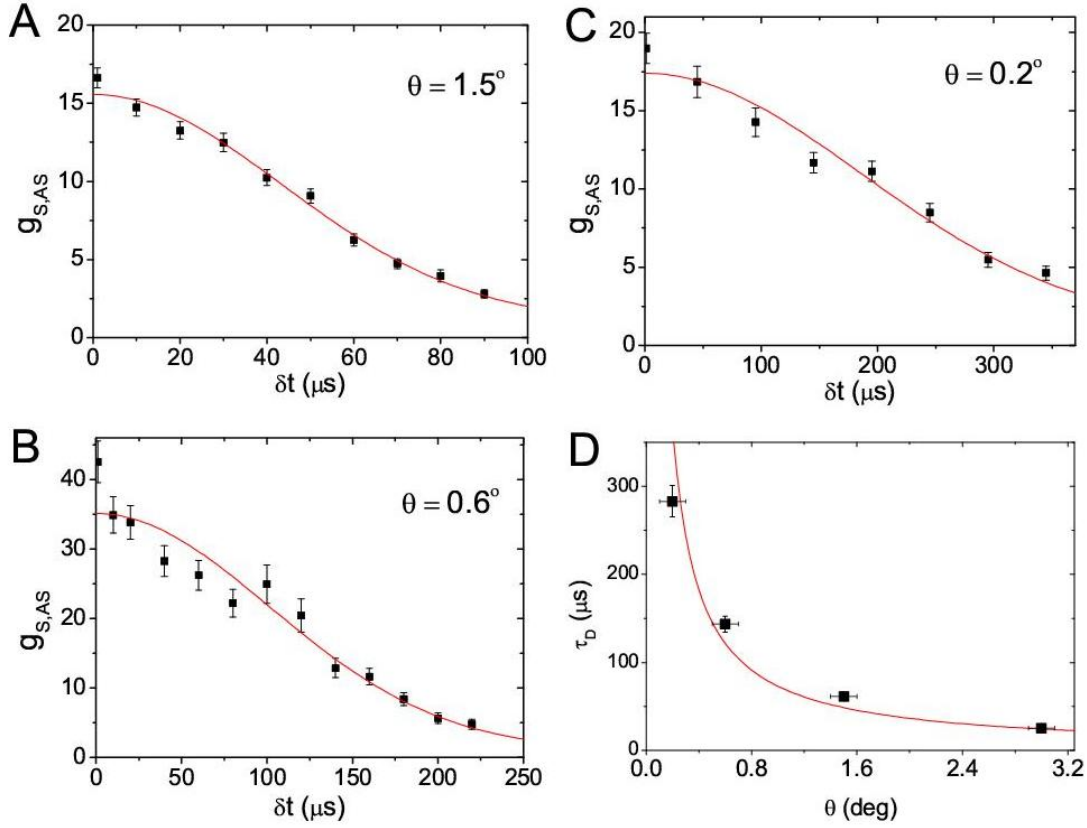


Figure 12.3: The cross correlation $g_{S,AS}$ versus the storage time δt for different angles (A)-(C) and the measured lifetime τ_D as a function of detection angle θ (D). Panels (A) and (B) are for $(|1, 0\rangle, |2, 0\rangle)$ at $\theta = 1.5^\circ$ and 0.6° , respectively. The data are fitted by using $g_{S,AS}(\delta t) = 1 + C \exp(-\delta t^2/\tau_D^2)$, where τ_D is the lifetime due to dephasing. Panel (C) is for $(|1, 1\rangle, |2, -1\rangle)$ at $\theta = 0.2^\circ$. In this case we take into account the effect of loss of atoms and fit the data by using $g_{S,AS}(\delta t) = 1 + C \exp(-\delta t^2/\tau_D^2)/(1 + A\delta t^2)$, with A the fitting parameter obtained from the collinear configuration. The fitted lifetime for each case is: (A) $\tau_D = 61 \pm 2 \mu\text{s}$, (B) $\tau_D = 144 \pm 9 \mu\text{s}$, (C) $\tau_D = 283 \pm 18 \mu\text{s}$. The first data are a little bit higher than the fitted curves, which might be caused by the imperfection in the pumping process. By reducing the angle, the lifetime is increased from $25 \mu\text{s}$ to $283 \mu\text{s}$, which implies the decoherence is mainly caused by the dephasing induced by atomic random motion. Panel (D) depicts the measured lifetime τ_D as a function of detection angle θ , where the horizontal error bars indicate measurement errors in the angles. The solid line is the theoretical curve with $T \simeq 100 \mu\text{K}$. The experimental results are in good agreement with the theoretical predications. The vertical error bars indicate statistical errors.

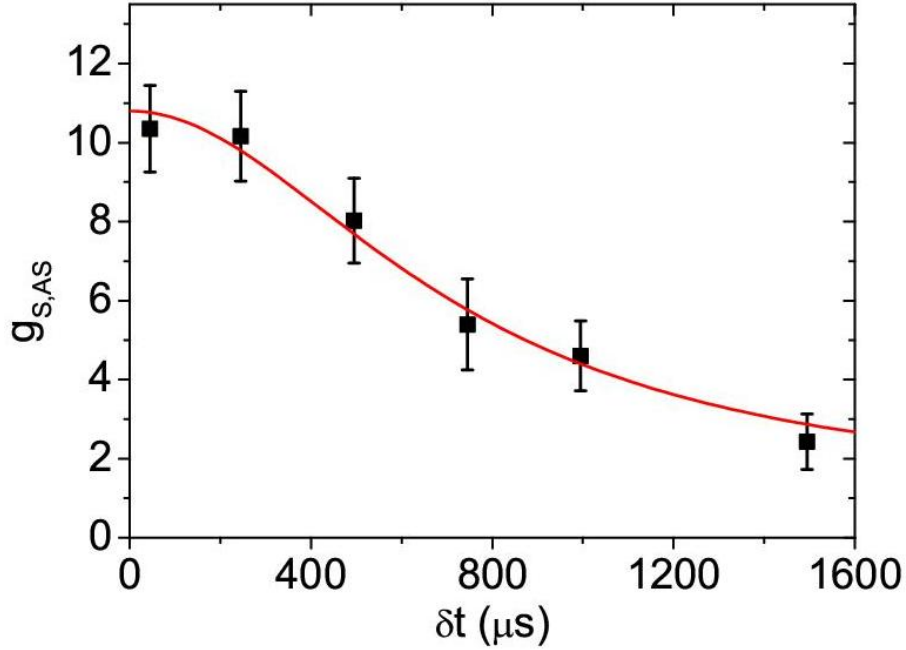


Figure 12.4: The cross correlation $g_{S,AS}$ versus the storage time δt for $\theta = 0^\circ$ and $(|1, 1\rangle, |2, -1\rangle)$. The data are fitted by using $g_{S,AS}(\delta t) = 1 + \frac{C}{1 + A\delta t^2}$, with A the fitting parameter. Our data give a lifetime of $\tau_L = 1.0 \pm 0.1$ ms, when the retrieval efficiency $\gamma(\delta t) = \frac{1}{1 + A\delta t^2}$ has dropped to $1/e$. Error bars represent statistical errors.

The experimental results are displayed in Fig. 12.3A-12.3C. As expected, the dephasing of the SW dominates in our experiment, where the effect of magnetic field is inhibited by using the “clock state”. The lifetime increases from $25 \mu\text{s}$ to $283 \mu\text{s}$ by reducing θ or, in other words, increasing the wavelength of SW. Our results clearly show that the long wavelength SW is robust against the dephasing induced by atomic random motion. Note that, for $\theta = 0.2^\circ$, the data are fitted by taking into account the effect of loss of atoms. The measured lifetime τ_D is shown in Fig. 12.3D as a function of angle θ . The solid line is the theoretical curve $\tau_D = \frac{1}{\Delta k v_s} \simeq \frac{73}{\theta} \mu\text{s}$, with $v_s = 0.1$ m/s corresponding to a temperature of $T \simeq 100 \mu\text{K}$, and θ measured in degree. The good agreements between theory and experiment imply that our work provides an alternative way to measure the temperature of an atomic ensemble. Moreover, since the lifetime is only sensitive to the velocity of the atoms in the interaction region, which is determined by the waist of the detection mode and is controllable, one can also use our method to measure the velocity distribution of the atomic ensemble by performing measurement in different regions.

To achieve longer storage time, we use the collinear configuration ($\theta = 0^\circ$), where we have the maximum wavelength of the SW $\lambda \simeq 4.4$ cm and thus $\tau_D \simeq 72$ ms. In this case, the decoherence due to loss of atoms becomes the principal decoherence mechanism. The experimental result is shown in Fig. 12.4, where the “clock state” $(|1, 1\rangle, |2, -1\rangle)$ is also used. Our data give a lifetime of $\tau_L = 1.0 \pm 0.1$ ms, when the retrieval efficiency has dropped to $1/e$. The experiment result is in good agreement with theoretical estimation.

12.3 Discussion

In our experiment, we have successfully realized a long-lived quantum memory for single-quanta SW by exploiting the “clock state” and long wavelength SW. The storage time of 1 ms is 2 orders of magnitude longer than previous results [45, 46, 65, 88]. The coherence time of the quantum memory is limited by the decoherence due to loss of atoms, which can be suppressed by lowering the temperature via optical molasses. A storage time of 3 ms is achievable by reducing the temperature to 10 μ K. This will be the upper limit for the atomic memory in MOT, since longer storage time is prohibited by the falling of the atoms under gravity. Further improvement might be achieved by trapping the atoms in an optical dipole trap, where the decoherence due to loss of atoms and the dephasing induced by atomic random motion can both be suppressed. In this case, the principal decoherence mechanism is the diffusion caused by collisions, which will give a lifetime of a few tens of milliseconds. To inhibit the collision-induced diffusion, one has to trap the atoms in a deep optical lattice, where each atom is tightly confined in a single site and collisions are avoided. The optical lattice has the potential to store the collective excitation for a few tens of seconds, which will reach the requirement in the storage time for a robust and efficient quantum repeater with atomic ensembles [49]. The idea presented in this work can also be applied to the quantum memory based on electromagnetically induced transparency [63, 92]. By using the same method as in our experiment, a lifetime of a few hundred microseconds can be expected.

Our work opens up the possibility to implement many tasks of quantum information processing. Combined with the techniques developed in recent years, one can implement a high-quality on-demand single-photon source, deterministic preparation of multi-qubit entanglement, generation of entanglement between two remote atomic memory qubits over a few hundred kilometers, and even construction of long-lived quantum nodes for scalable quantum networks. More generally, our work presents an experimental investigation on the decoherence of the SW at single quanta level. It is clearly shown that long wavelength SW is robust against dephasing. Besides, our work also provides an approach to measure the temperature or the velocity distribution of an atomic ensemble. Furthermore, since the decoherence of the SW is controllable, one can measure certain important physical quantity by introducing some new physical mechanisms. For example, when performing experiments in optical dipole trap, the lifetime is determined by collision between atoms. Thereby, the s-wave scattering cross section or scattering length might be measured using our approach.

Chapter 13

Conclusion and outlook

Implementing long-distance quantum communication with atomic ensembles and linear optics is attractive because it needs relatively simple ingredients. In this work, we report our recent theoretical and experimental progress along this direction. To conclude this thesis we will give a summary of its main points as well as an outlook to future work.

We have first proposed a robust and efficient quantum repeater architecture with atomic ensembles and linear optics building on the original DLCZ protocol. The interaction between atomic ensembles and light is discussed, where a simple diffraction model is exploited to describe the write and read process, where the spatial mode of the Stokes and anti-Stokes light is easily obtained. The relationship between the retrieval efficiency and decoherence mechanisms in atomic ensemble is discussed as well. The nonclassical correlation between the Stokes photon and anti-Stokes photon is characterized by the violation of the Cauchy-Schwarz inequality. We then review the DLCZ protocol and give a particular analysis on its drawbacks, i.e., phase stabilization problem and low entanglement distribution rate. These drawbacks, which result from the single photon interference in both entanglement generation and entanglement swapping, are severe enough to make a realistic long-distance quantum communication impossible. To solve the phase stabilization problem, a robust quantum repeater is presented by exploiting two-photon Hong-Ou-Mandel-type interference, which relaxes the long distance stability requirements by about 7 orders of magnitude, from sub wavelength for the single photon interference required by DLCZ to the coherence length of the photons. To improve the entanglement distribution rate, we propose to locally generate quasi-ideal entangled pair by partial readout of the ensemble-based memories. The rate improvement compared to the DLCZ protocol is by a factor of 300. Thus the new quantum repeater protocol is both robust with respect to phase fluctuations in the transmission channels and significantly more efficient than all other protocols that use the same ingredients.

We then report our recent experimental progress towards the realistic long-distance quantum communication with atomic ensembles. A deterministic single-photon source based on atomic ensembles is proposed and experimentally demonstrated by the aid of feedback circuit. The Hong-Ou-Mandel-type interference between two single photons generated from two independent atomic ensembles is observed in both time and frequency domain, which are in good agreement with the theoretical predications. The quantum

teleportation between a photonic qubit and an atomic qubit serving as the quantum memory is realized, where the teleportation fidelity is beyond the classical threshold up to $8 \mu\text{s}$. A stable atom-photon entanglement source is proposed and demonstrated by using only one write beam to excite one atomic ensemble, where two spatial modes of the scattered light is extracted to generate the atom-photon entanglement. The entanglement still survives after a storage time of $20.5 \mu\text{s}$, which is proved by violation of the CHSH inequality. With this type of stable entanglement source, we demonstrated entanglement swapping between two remote memory qubits at a distance of 300 m, which can serve as a building-block of the robust and efficient quantum repeater. To extend the coherence time, we use atoms trapped in optical dipole trap as the quantum memory, where a lifetime of $70 \mu\text{s}$ is observed. Moreover, a long-lived quantum memory with millisecond storage time is demonstrated by exploiting “clock state” and a long wavelength spin wave.

Although so many progresses has been achieved in these years, there is still a lot to be done to implement a realistic quantum repeater. Among them, the retrieval efficiency and the lifetime of the quantum memory are the most important two factors to be improved. For current experiments performed in MOT, the lifetime is limited by the residual magnetic field and the dephasing induced by atomic motion. The decoherence induced by residual magnetic field can be eliminated by using the clock state to store the quantum state. The dephasing induced by atomic motion can be bypassed by reducing the angle between the write light and Stokes field. Our recent experiments show that by combing these two techniques, the lifetime can be extended to 1 ms, which is improved by 2 orders of magnitude. However, this is the upper limit for the atomic memory trapped in MOT, because for longer time the atom will fall down under gravity.

A possible solution is to trap the atoms in optical dipole trap, where the atoms are trapped in a relatively small region and won't fly out of the interaction region due to the strong confinement. Our experiment provides the first evidence for the realization of a quantum memory with long storage time employing optically trapped atoms in the clock states. In this case, the lifetime is limited by the light shift of the optical trap and the collision between the atoms. The light shift can be compensated by a classical laser pulse. The decoherence induced by collisions can be solved by trapping the atoms in optical lattice. With these improvement, the lifetime has the potential to be extended to a few tens of seconds. Trapping atoms in optical dipole trap or optical lattice can also help to improve the retrieval efficiency, which is mainly determined by the optical depth of the atomic ensembles. In optical trap, due to the high density, the optical depth can be 100 times higher than that in MOT, which implies a significant improvement in retrieval efficiency.

The theoretical and experimental results presented in this thesis open up an exciting possibility to implement the realistic long-distance quantum communication with atomic ensembles and linear optics. It is expected that by exploiting the new techniques and trapping the atoms in optical lattice, a robust and efficient quantum repeater can be realized in the near future.

Appendix:

Associated Publications

Within the frame work of the presented thesis the following publications have been achieved:

- Zeng-Bing Chen, **Bo Zhao**, Yu-Ao Chen, Jörg Schmiedmayer, and Jian-Wei Pan. Fault-tolerant Quantum Repeater with Atomic Ensembles and Linear Optics. *Phys. Rev. A* **76**, 022329 (2007). (Chapter 3)
- **Bo Zhao**, Zeng-Bing Chen, Yu-Ao Chen, Jörg Schmiedmayer, and Jian-Wei Pan. Robust Creation of Entanglement between Remote Memory Qubits. *Phys. Rev. Lett.* **98**, 240502 (2007). (Chapter 4)
- Nicolas Sangouard, Christoph Simon, **Bo Zhao**, Yu-Ao Chen, Hugues de Riedmatten, Jian-Wei Pan and Nicolas Gisin. Robust and Efficient Quantum Repeaters with Atomic Ensembles and Linear Optics. Accepted by *Phys. Rev. A* (2008). (Chapter 5)
- Shuai Chen, Yu-Ao Chen, Thorsten Strassel, Zhen-Sheng Yuan, **Bo Zhao**, Jörg Schmiedmayer, and Jian-Wei Pan. Deterministic and Storable Single-Photon Source Based on a Quantum Memory. *Phys. Rev. Lett.* **97**, 173004 (2006). (Chapter 6)
- Zhen-Sheng Yuan, Yu-Ao Chen, Shuai Chen, **Bo Zhao**, Markus Koch, Thorsten Strassel, Yong Zhao, Gan-Jun Zhu, Jörg Schmiedmayer, and Jian-Wei Pan. Synchronized Independent Narrow-Band Single Photons and Efficient Generation of Photonic Entanglement. *Phys. Rev. Lett.* **98**, 180503 (2007). (Chapter 7)
- Yu-Ao Chen, Shuai Chen, Zhen.-Sheng. Yuan, **Bo Zhao**, Chih-Sung Chuu, Jörg Schmiedmayer, and Jian-Wei Pan. Memory-built-in Quantum Teleportation between Photonic and Atomic Qubits. *Nature Physics*, **4**, 103 (2008). (Chapter 8)
- Shuai Chen, Yu-Ao Chen, **Bo Zhao**, Zhen-Sheng Yuan, Jörg Schmiedmayer, and Jian-Wei Pan. Demonstration of a Stable Atom-photon Entanglement Source for Quantum Repeater. *Phys. Rev. Lett.* **99**, 180505 (2007). (Chapter 9)
- Zhen-Sheng Yuan, Yu-Ao Chen, **Bo Zhao**, Shuai-Chen, Jörg Schmiedmayer, and Jian-Wei Pan. Entanglement Swapping with Storage and Retrieval of Light: A Building Block of Quantum Repeaters. Submitted to *Nature* (2008). (Chapter 10)

- Chih-Sung Chuu, Thorsten Strassel, **Bo Zhao**, Markus Koch, Yu-Ao Chen, Shuai Chen, Zhen-Sheng Yuan, Jörg Schmiedmayer, and Jian-Wei Pan. Demonstration of a Quantum Memory with Optically Trapped Atoms. Submitted to Phys. Rev. Lett. (2008). (Chapter [11](#))
- **Bo Zhao**, Yu-Ao Chen, Xiao-Hui Bao, Thorsten Strassel, Chih-Sung Chuu, Zhen-Sheng Yuan, Shuai Chen, and Jian-Wei Pan. A Millisecond Quantum Memory for Scalable Quantum Networks. Submitted to Nature Physics (2008). (Chapter [12](#))

Acknowledgement

First of all, I would like to express my gratitude to my supervisor, Prof. Jian-Wei Pan, for his continuous guidance and support through these three and a half years. He taught me with wisdom and encouragement, the way to conduct scientific research, especially how to connect theory with experiment. His physical insight, enthusiasm and curiosity for research make a strong impression and keep me motivated.

I would like to thank my second supervisor, Prof Jörg Schmiedmayer, who is always interested in discussing all the questions I brought to him. I am also grateful to him for introducing the theoreticians in Trento, with whom the cooperation is fruitful. I also want to thank Prof. Zeng-Bing Chen, with whom I collaborated on most of the theoretical work. I am also grateful to him for teaching me how to write a scientific paper.

In all the years of my study, it is my great pleasure to work with the experimenters in the "Quantum Memory group" in Heidelberg. I would like to express my gratitude to Dr. Yu-Ao Chen, Dr. Shuai Chen and Dr. Zhen-Sheng Yuan, without whose collaboration, this work would not have been possible. The discussions with them are always exciting and encouraging. I also would like to thank Dr. Yu-Ao Chen for giving me the thesis template, on which the current work is based.

I would like to thank Dr. Chih-Sung Chuu, Thorsten Strassel, Koch Markus, who are in charge of the optical dipole trap experiment. The discussions with them let me understand more about the experiments. I am also grateful to Thorsten Strassel for reading the thesis. I would like to thank Dr. Qiang Zhang, Alexander Göbel, Claudia Wagenknecht and Dr. Kai Chen, who implemented the multi-photon experiments. I also want to thank Dr. You-Jin Deng for reading my thesis. We also have a fruitful discussion on Bell inequality and nonlocality.

Many thanks to Prof. Yong-De Zhang, my graduate supervisor, for his outstanding guidance and continuous concern on my research and life.

I am grateful to Dr. Alessio Recati, Dr. Grigory E. Astrakharchik, Prof. Tommaso Calarco, and Dr. Christoph Simon, from whom I learned a lot in the collaboration. I also want to thank Yong Zhao and Xiao-Hui Bao for their assistance in my life.

Finally, I would like to thank to my parents, my sister, and my wife for their patience and full support during all these years.

Bibliography

- [1] C. H. Bennett, G. Brassard, C. Crepeau, R. Jozsa, A. Peres, and W. K. Wootters. Teleporting an unknown quantum state via dual classic and Einstein-Podolsky-Rosen channels. *Phys. Rev. Lett.*, 70:1895–1899, 1993.
- [2] D. Bouwmeester, J.-W. Pan, K. Mattle, M. Eibl, H. Weinfurter, and A. Zeilinger. Experimental quantum teleportation. *Nature*, 390:575–579, 1997.
- [3] M. Żukowski, A. Zeilinger, M. A. Horne, and A. K. Ekert. “event-ready-detectors” Bell experiment via entanglement swapping. *Phys. Rev. Lett.*, 71:4287–4290, 1993.
- [4] J.-W. Pan, D. Bouwmeester, H. Weinfurter, and A. Zeilinger. Experimental entanglement swapping: entangling photons that never interacted. *Phys. Rev. Lett.*, 80:3891–3894, 1998.
- [5] M A. Nielsen and Isaac L. Chuang. *Quantum Computation and Quantum Information*. 2001.
- [6] N. Gisin, G. Ribordy, W. Tittel, and H. Zbinden. Quantum cryptography. *Rev. Mod. Phys.*, 74:145, 2002.
- [7] D. Deutsch. Quantum theory, the church-turing principle and the universal quantum computer. *Proceedings of the Royal Society of London A*, 400:97–117., 1985.
- [8] P. W. Shor. Polynomial-time algorithms for prime factorization and discrete logarithms on a quantum computer. In *Proceedings of the 35th Annual Symposium on Foundations of Computer Science*, 1994.
- [9] A. Ekert and R. Jozsa. Quantum computation and shor’s factoring algorithm. *Rev. Mod. Phys.*, 68:733–753, 1996.
- [10] L. K. Grover. Quantum mechanics helps in searching for a needle in a haystack. *Phys. Rev. Lett.*, 79:325, 1997.
- [11] L. K. Vandersypen, M. Steffen, G. Breyta, C. S. Yannoni, M. H. Sherwood, and I. L. Chuang. Experimental realization of shor’s quantum factoring algorithm using nuclear magnetic resonance. *Nature*, 414:883–887, 2001.
- [12] J. A. Jones. *Quantum Computing and NMR in Quantum Computing and Communication*. Springer-Verlag, 1999.
- [13] J. I. Cirac and P. Zoller. Quantum computations with cold trapped ions. *Phys. Rev. Lett.*, 74:4091 – 4094, 1995.
- [14] M. Riebe, H. Häffner, C. F. Roos, W. Hänsel, J. Benhelm, G. P. T. Lancaster, T. W. Körber, C. Becher, F. Schmidt-Kaler, D. F. V. James, and R. Blatt. Deterministic quantum teleportation with atoms. *Nature*, 429:734–737, 2004.
- [15] M. D. Barrett, J. Chiaverini, T. Schaetz, J. Britton, W. M. Itano, J. D. Jost, E. Knill, C. Langer, D. Leibfried, R. Ozeri, and D. J. Wineland. Deterministic quantum teleportation of atomic qubits. *Nature*, 429:737–739, 2004.

- [16] D. Leibfried, E. Knill, S. Seidelin, J. Britton, R. B. Blakestad, J. Chiaverini, D. B. Hume, W. M. Itano, J. D. Jost, C. Langer, R. Ozeri, R. Reichle, and D. J. Wineland. Creation of a six-atom ‘Schrödinger cat’ state. *Nature*, 438:639–642, 2005.
- [17] H. Häffner, W. Hänsel, C. F. Roos, J. Benhelm, D. Chek al kar, M. Chwalla, T. Körber, U. D. Rapol, M. Riebe, P. O. Schmidt, C. Becher, O. Gühne, W. Dür, and R. Blatt. Scalable multiparticle entanglement of trapped ions. *Nature*, 438:643–646, 2005.
- [18] E. Knill, R. Laflamme, and G. J. Milburn. A scheme for efficient quantum computation with linear optics. *Nature*, 409:46–52, 2001.
- [19] M. A. Nielsen. Optical quantum computation using cluster states. *Phys. Rev. Lett.*, 93:040503, 2004.
- [20] N. Yoran and B. Reznik. Deterministic linear optics quantum computation with single photon qubits. *Phys. Rev. Lett.*, 91:037903, 2003.
- [21] P. Kok, W. J. Munro, K. Nemoto, T. C. Ralph, J. P. Dowling, and G. J. Milburn. Linear optical quantum computing with photonic qubits. *Rev. Mod. Phys.*, 79:135–174, 2007.
- [22] S. Popescu. Knill-laflamme-milburn linear optics quantum computation as a measurement-based computation. *Phys. Rev. Lett.*, 99:250501, 2007.
- [23] B. Zhao, Z.-B. Chen, J.-W. Pan, J. Schmiedmayer, A. Recati, G. E. Astrakharchik, and T. Calarco. High-fidelity entanglement via molecular dissociation in integrated atom optics. *Phys. Rev. A*, 75:042312, 2007.
- [24] Z. Zhao, Y.-A. Chen, A.-N. Zhang, T. Yang, H. Briegel, and J.-W. Pan. Experimental demonstration of five-photon entanglement and open-destination teleportation. *Nature*, 430:54–57, 2004.
- [25] Q. Zhang, A. Goebel, C. Wagenknecht, Y.-A. Chen, B. Zhao, T. Yang, A. Mair, J. Schmiedmayer, and J.-W. Pan. Experimental quantum teleportation of a two-qubit composite system. *Nature Physics*, 2:678–682, 2006.
- [26] R. Raussendorf and H. J. Briegel. A one-way quantum computer. *Phys. Rev. Lett.*, 86:5188–5191, 2001.
- [27] P. Walther, K. J. Resch, T. Rudolph, E. Schenck, H. Weinfurter, V. Vedral, M. Aspelmeyer, and A. Zeilinger. Experimental one-way quantum computing. *Nature*, 434:169–176, 2005.
- [28] C.-Y. Lu, X.-Q. Zhou, O. Gühne, W.-B. Gao, J. Zhang, Z.-S. Yuan, A. Goebel, Tao Yang, and Jian-Wei Pan. Experimental entanglement of six photons in graph states. *Nature Physics*, 3:91–95, 2007.
- [29] K. Chen, C.-M. Li, Q. Zhang, Y.-A. Chen, A. Goebel, S. Chen, A. Mair, and J.-W. Pan. Experimental realization of one-way quantum computing with two-photon four-qubit cluster states. *Phys. Rev. Lett.*, 99:120503, 2007.
- [30] M. S. Tame, R. Prevedel, M. Paternostro, P. Böhi, M. S. Kim, and A. Zeilinger. Experimental realization of Deutsch’s algorithm in a one-way quantum computer. *Phys. Rev. Lett.*, 98:140501, 2007.
- [31] C. H. Bennett and G. Brassard. *in Proc. IEEE Int. Conf. on Computers, systems, and signal processing*, Bangalore, India:(IEEE, New York, 1984), 175.
- [32] C.-Z. Peng, J. Zhang, D. Yang, W.-B. Gao, H.-X. Ma, H. Yin, H.-P. Zeng, T. Yang, X.-B. Wang, and J.-W. Pan. Experimental long-distance decoy-state quantum key distribution based on polarization encoding. *Phys. Rev. Lett.*, 98:010505, 2007.

-
- [33] T. Schmitt-Manderbach, H. Weier, M. Fürst, R. Ursin, F. Tiefenbacher, T. Scheidl, J. Perdigues, Z. Sodnik, C. Kurtsiefer, J. G. Rarity, A. Zeilinger, and H. Weinfurter. Experimental demonstration of free-space decoy-state quantum key distribution over 144 km. *Phys. Rev. Lett.*, 98:010504, 2007.
- [34] R. Ursin, F. Tiefenbacher, T. Schmitt-Manderbach, H. Weier, T. Scheidl, M. Lindenthal, B. Blauensteiner, T. Jennewein, J. Perdigues, P. Trojek, B. Ömer, M. Fürst, M. Meyenburg, J. Rarity, Z. Sodnik, C. Barbieri, H. Weinfurter, and A. Zeilinger. Entanglement-based quantum communication over 144 km. *Nature Physics*, 3:481, 2007.
- [35] A. K. Ekert. Quantum cryptography based on Bell’s theorem. *Phys. Rev. Lett.*, 67:661–663, 1991.
- [36] H. J. Briegel, W. Dur, J. I. Cirac, and P. Zoller. Quantum repeaters: the role of imperfect local operations in quantum communication. *Phys. Rev. Lett.*, 81:5932–5935, 1998.
- [37] W. Dür, H.-J. Briegel, J. I. Cirac, and P. Zoller. Quantum repeaters based on entanglement purification. *Phys. Rev. A*, 59:169–181, 1999.
- [38] D. Deutsch, A. Ekert, R. Jozsa, C. Macchiavello, S. Popescu, and A. Sanpera. Quantum privacy amplification and the security of quantum cryptography over noisy channels. *Phys. Rev. Lett.*, 77:2818–2821, 1996.
- [39] C. H. Bennett, G. Brassard, S. Popescu, B. Schumacher, J. A. Smolin, and W. K. Wootters. Purification of noisy entanglement and faithful teleportation via noisy channels. *Phys. Rev. Lett.*, 76:722–725, 1996.
- [40] J. I. Cirac, P. Zoller, H. J. Kimble, and H. Mabuchi. Quantum state transfer and entanglement distribution among distant nodes in a quantum network. *Phys. Rev. Lett.*, 78:3221, 1997.
- [41] S.J. van Enk, J.I. Cirac, and P. Zoller. Photonic channels for quantum communication. *Science*, 279:205–208, 1998.
- [42] L.-M. Duan, M. D. Lukin, J. I. Cirac, and P. Zoller. Long-distance quantum communication with atomic ensembles and linear optics. *Nature*, 414:413–418, 2001.
- [43] A. Kuzmich, W. P. Bowen, A. D. Boozer, A. Boca, C. W. Chou, L.-M. Duan, and H. J. Kimble. Generation of nonclassical photon pairs for scalable quantum communication with atomic ensembles. *Nature (London)*, 423:731, 2003.
- [44] C. H. van der Wal, M. D. Eisaman, A. André, R. L. Walsworth, D. F. Phillips, A. S. Zibrov, , and M. D. Lukin. Atomic memory for correlated photon states. *Science*, 301:196–200, 2003.
- [45] D. N. Matsukevich, T. Chanelière, S. D. Jenkins, S.-Y. Lan, T. A. B. Kennedy, and A. Kuzmich. Deterministic single photons via conditional quantum evolution. *Phys. Rev. Lett.*, 97:013601, 2006.
- [46] S. Chen, Y.-A. Chen, T. Strassel, Z.-S. Yuan, B. Zhao, J. Schmiedmayer, and J.-W. Pan. Deterministic and storable single-photon source based on quantum memory. *Phys. Rev. Lett.*, 97:173004, 2006.
- [47] C. W. Chou, H. de Riedmatten, D. Felinto, S. V. Polyakov, S. J. van Enk, and H. J. Kimble. Measurement-induced entanglement for excitation stored in remote atomic ensembles. *Nature*, 438:828–832, 2005.
- [48] Z.-B. Chen, B. Zhao, Y.-A. Chen, J. Schmiedmayer, and J.-Wei Pan. Fault-tolerant quantum repeater with atomic ensembles and linear optics. *Phys. Rev. A*, 76:022329, 2007.
- [49] N. Sangouard, C. Simon, B. Zhao, Y.-A. Chen, H. de Riedmatten, J.-W. Pan, and N. Gisin. Robust and efficient quantum repeaters with atomic ensembles and linear optics. *Phys. Rev. A (to be published)*, 2007.

- [50] M. D. Lukin. Colloquium: Trapping and manipulating photon states in atomic ensembles. *Rev. Mod. Phys.*, 75:457–472, 2003.
- [51] A. André. *Nonclassical States of Light and Atomic Ensembles: Generation and New Applications*. PhD thesis, Harvard University, Graduate School of Arts and Sciences, 2005.
- [52] L. M. Duan, J. I. Cirac, and P. Zoller. Three-dimensional theory for interaction between atomic ensembles and free-space light. *Phys. Rev. A*, 66:023818, 2002.
- [53] M. G. Raymer and J. Mostowski. Stimulated Raman scattering: Unified treatment of spontaneous initiation and spatial propagation. *Phys. Rev. A*, 24:1980–1993, 1981.
- [54] C. M. Bowden and C. C. Sung. Initiation of superfluorescence in coherently pumped three-level systems. *Phys. Rev. Lett.*, 50:156, 1983.
- [55] J. C. Englund and C. M. Bowden. Spontaneous generation of phase waves and solitons in stimulated raman scattering: Quantum-mechanical models of stimulated raman scattering. *Phys. Rev. A*, 42:2870, 1990.
- [56] L. Mandel and E. Wolf. *Optical Coherence and Quantum Optics*. Cambridge University Press., Cambridge, UK, 1995.
- [57] Marlan O. Scully and M. Suhail Zubairy. *Quantum Optics*. Cambridge University Press, 1997.
- [58] M. Fleischhauer, A. Imamoglu, and J. P. Marangos. Electromagnetically induced transparency: Optics in coherent media. *Rev. Mod. Phys.*, 77:633–673, 2005.
- [59] A. V. Gorshkov, A. André, M. D. Lukin, and A. S. Sørensen. Photon storage in Λ -type optically dense atomic media. ii. free-space model. *Phys. Rev. A*, 76:033805, 2007.
- [60] D. Felinto, C. W. Chou, H. de Riedmatten, S. V. Polyakov, and H. J. Kimble. Control of decoherence in the generation of photon pairs from atomic ensembles. *Phys. Rev. A*, 72:053809, 2005.
- [61] Koch Markus. Atomic ensembles in an optical dipole trap: Towards a quantum memory with a long storage time. Master’s thesis, Univeisity Heidelberg, 2007.
- [62] M. D. Lukin, S. F. Yelin, and M. Fleischhauer. Entanglement of atomic ensembles by trapping correlated photon states. *Phys. Rev. Lett.*, 84:4232–4235, 2000.
- [63] M. Fleischhauer and M. D. Lukin. Dark-state polaritons in electromagnetically induced transparency. *Phys. Rev. Lett.*, 84:5094–5097, 2000.
- [64] S. D. Jenkins. *Theory of Light $\dot{I}C$ Atomic Ensemble Interactions: Entanglement, Storage, and Retrieval*. PhD thesis, Georgia Institute of Technology, 2006.
- [65] Chin-Wen Chou, Julien Laurat, Hui Deng, Kyung Soo Choi, Hugues de Riedmatten, Daniel Felinto, and H. Jeff Kimble. Functional quantum nodes for entanglement distribution over scalable quantum networks. *Science*, 316:1316, 2007.
- [66] B. Zhao, Z.-B. Chen, Y.-A. Chen, J. Schmiedmayer, and J.-W. Pan. Robust creation of entanglement between remote memory qubits. *Phys. Rev. Lett.*, 98:240502, 2007.
- [67] L. Jiang, J. M. Taylor, and M. D. Lukin. A fast and robust approach to long-distance quantum communication with atomic ensembles. *Phys. Rev. A*, 76:012301, 2007.
- [68] C. Simon, H. de Riedmatten, M. Afzelius, N. Sangouard, H. Zbinden, and N. Gisin. Quantum repeaters with photon pair sources and multimode memories. *Phys. Rev. Lett.*, 98:190503, 2007.
- [69] K.W. Holman, D.D. Hudson, J. Ye, and D. J. Jones. Remote transfer of a high-stability and ultralow-jitter timing signal. *Opt. Lett.*, 30:1225, 2005.

- [70] C.-Z. Peng, T. Yang, X.-H. Bao, J. Zhang, X.-M. Jin, F.-Y. Feng, B. Yang, J. Yang, J. Yin, Q. Zhang, N. Li, B.-L. Tian, and J.-W. Pan. Experimental free-space distribution of entangled photon pairs over 13 km: towards satellite-based global quantum communication. *Phys. Rev. Lett.*, 94:150501, 2005.
- [71] C. K. Hong, Z. Y. Ou, and L. Mandel. Measurement of subpicosecond time intervals between two photons by interference. *Phys. Rev. Lett.*, 59:2044–2046, 1987.
- [72] C. Simon and W. T. M. Irvine. Robust long-distance entanglement and a loophole-free Bell test with ions and photons. *Phys. Rev. Lett.*, 91:110405, 2003.
- [73] X.-L. Feng, Z.-M. Zhang, X.-D. Li, S.-Q. Gong, and Zhi-Zhan Xu. Entangling distant atoms by interference of polarized photons. *Phys. Rev. Lett.*, 90:217902, 2003.
- [74] M. D. Eisaman, L. Childress, A. André, F. Massou, A. S. Zibrov, and M. D. Lukin. Shaping quantum pulses of light via coherent atomic memory. *Phys. Rev. Lett.*, 93:233602, 2004.
- [75] M. D. Eisaman, A. André, F. Massou, M. Fleischhauer, A. S. Zibrov, and M. D. Lukin. Electromagnetically induced transparency with tunable single-photon pulses. *Nature*, 438:837, 2005.
- [76] T. Chanelière, D. N. Matsukevich, S. D. Jenkins, S.-Y. Lan, R. Zhao, T. A. B. Kennedy, and A. Kuzmich. Quantum interference of electromagnetic fields from remote quantum memories. *Phys. Rev. Lett.*, 98:113602, 2007.
- [77] Z.-S. Yuan, Y.-A. Chen, S. Chen, B. Zhao, M. Koch, T. Strassel, Y. Zhao, G.-J. Zhu, J. Schmiedmayer, and J.-W. Pan. Synchronized independent narrow-band single photons and efficient generation of photonic entanglement. *Phys. Rev. Lett.*, 98:180503, 2007.
- [78] D. Felinto, C. W. Chou, J. Laurat, E. W. Schomburg, H. de Riedmatten, and H. J. Kimble. Conditional control of the quantum states of remote atomic memories for quantum networking. *Nature Physics*, 2:844, 2006.
- [79] J.-W. Pan, Z.-B. Chen, M. Żukowski, H. Weinfurter, and Anton Zeilinger. Multi-photon entanglement and interferometry. *Rev. Mod. Phys.*, in press (2007).
- [80] D. E. Browne and T. Rudolph. Resource-efficient linear optical quantum computation. *Phys. Rev. Lett.*, 95:010501, 2005.
- [81] D. N. Matsukevich and A. Kuzmich. Quantum state transfer between matter and light. *Science*, 306:663, 2004.
- [82] A. V. Gorshkov, A. André, M. Fleischhauer, A. S. Sørensen, and M. D. Lukin. Universal approach to optimal photon storage in atomic media. *Phys. Rev. Lett.*, 98:123601, 2007.
- [83] J.-W. Pan, C. Simon, C. Brukner, and A. Zeilinger. Entanglement purification for quantum communication. *Nature*, 410:1067–1070, 2001.
- [84] J.-W. Pan, S. Gasparoni, U. Rupert, G. Weihs, and A. Zeilinger. Experimental entanglement purification of arbitrary unknown states. *Nature*, 423:417–422, 2003.
- [85] D. F. V. James and P. G. Kwiat. Atomic-vapor-based high efficiency optical detectors with photon number resolution. *Phys. Rev. Lett.*, 89:183601, 2002.
- [86] A. Imamoglu. High efficiency photon counting using stored light. *Phys. Rev. Lett.*, 89:163602, 2002.
- [87] Y.-A. Chen, S. Chen, Z.-S. Yuan, B. Zhao, C.-S. Chuu, J. Schmiedmayer, and J.-W. Pan. Memory-built-in quantum teleportation with photonic and atomic qubits. *Nature Physics*, 4:103, 2008.
- [88] J. Simon, H. Tanji, J. K. Thompson, and V. Vuletić. Interfacing collective atomic excitations and single photons. *Phys. Rev. Lett.*, 98:183601, 2007.

- [89] J. Minar, H. de Riedmatten, C. Simon, H. Zbinden, and N. Gisin. Phase noise measurements in long fiber interferometers for quantum repeaters applications. *arXiv:quant-ph/0712.0740*.
- [90] N. Sangouard, C. Simon, J. Minar, H. Zbinden, H. de Riedmatten, and N. Gisin. Long-distance entanglement distribution with single-photon sources. *Phys. Rev. A*, 76:050301, 2007.
- [91] Q. Zhang, X.-H. Bao, C.-Y. Lu, X.-Q. Zhou, T. Yang, T. Rudolph, and J.-W. Pan. Demonstration of efficient scheme for generation of “event ready” entangled photon pairs from single photon source. *arXiv:quant-ph/0610145*, 2006.
- [92] T. Chanelière, D. N. Matsukevich, S. D. Jenkins, S.-Y. Lan, T. A. B. Kennedy, and A. Kuzmich. Storage and retrieval of single photons transmitted between remote quantum memories. *Nature*, 438:833–836, 2005.
- [93] C. Sliwa and K. Banaszek. Conditional preparation of maximal polarization entanglement. *Phys. Rev. A*, 67:030101(R), 2003.
- [94] P. Walther, M. Aspelmeyer, and A. Zeilinger. Heralded generation of multiphoton entanglement. *Phys. Rev. A*, 75:012313, 2007.
- [95] S. A. Moiseev and S. Kröll. Complete reconstruction of the quantum state of a single-photon wave packet absorbed by a doppler-broadened transition. *Phys. Rev. Lett.*, 87:173601, 2001.
- [96] M. Nilsson and S. Kroell. Solid state quantum memory using complete absorption and re-emission of photons by tailored and externally controlled inhomogeneous absorption profiles. *Optics Communications*, 247:393, 2005.
- [97] B. Kraus, W. Tittel, N. Gisin, M. Nilsson, S. Kröll, and J. I. Cirac. Quantum memory for nonstationary light fields based on controlled reversible inhomogeneous broadening. *Phys. Rev. A*, 73:020302(R), 2006.
- [98] A. L. Alexander, J. J. Longdell, M. J. Sellars, and N. B. Manson. Photon echoes produced by switching electric fields. *Phys. Rev. Lett.*, 96:043602, 2006.
- [99] E. Fraval, M. J. Sellars, and J. J. Longdell. Dynamic decoherence control of a solid-state nuclear-quadrupole qubit. *Phys. Rev. Lett.*, 95(3):030506, 2005.
- [100] G. Hétet, J. J. Longdell, A. L. Alexander, P. K. Lam, and M. J. Sellars. Electro-optic quantum memory for light using two-level atoms. *Phys. Rev. Lett.*, 100:023601, 2008.
- [101] O. A. Collins, S. D. Jenkins, A. Kuzmich, and T. A. B. Kennedy. Multiplexed memory-insensitive quantum repeaters. *Phys. Rev. Lett.*, 98:060502, 2007.
- [102] M. U. Staudt, S. R. Hastings-Simon, M. Nilsson, M. Afzelius, V. Scarani, R. Ricken, H. Suche, W. Sohler, W. Tittel, and N. Gisin. Fidelity of an optical memory based on stimulated photon echoes. *Phys. Rev. Lett.*, 98:113601, 2007.
- [103] M. U. Staudt, M. Afzelius, H. de Riedmatten, S. R. Hastings-Simon, C. Simon, R. Ricken, H. Suche, W. Sohler, , and N. Gisin. Interference of multimode photon echoes generated in spatially separated solid-state atomic ensembles. *Phys. Rev. Lett.*, 99:173602, 2007.
- [104] S. Tanzilli, W. Tittel, M. Halder, O. Alibart, P. Baldi, N. Gisin, and H. Zbinden. A photonic quantum information interface. *Nature*, 437:116, 2005.
- [105] D. Rosenberg, A.E. Lita, A.J. Miller, and S.W. Nam. Noise-free high-efficiency photon-number-resolving detectors. *Phys. Rev. A*, 71:061803(R), 2005.
- [106] A.J. Miller and S.W. Nam, J.M. Martinis, and A.V. Sergienko. Demonstration of a low-noise near-infrared photon counter with multiphoton discrimination. *Appl. Phys. Lett.*, 83:791, 2003.
- [107] K. M. Rosfjord, J. K. W. Yang, E. A. Dauler, A. J. Kerman, V. Anant, B. M. Voronov, G. N. Gol’tsman, and K. K. Berggren. Nanowire single-photon detector with an integrated optical cavity and anti-reflection coating. *Optics Express.*, 14:527, 2006.

-
- [108] B.B. Blinov, D.L. Moehring, L.-M. Duan, and C. Monroe. Observation of entanglement between a single trapped atom and a single photon. *Nature*, 428:153, 2004.
- [109] J. Volz, M. Weber, D. Schlenk, W. Rosenfeld, J. Vrana, K. Saucke, C. Kurtsiefer, and H. Weinfurter. Observation of entanglement of a single photon with a trapped atom. *Phys. Rev. Lett.*, 96:030404, 2006.
- [110] O. Benson, C. Santori, M. Pelton, and Y. Yamamoto. Regulated and entangled photons from a single quantum dot. *Phys. Rev. Lett.*, 84:2513, 2000.
- [111] C. Simon and J.P. Poizat. Creating single time-bin-entangled photon pairs. *Phys. Rev. Lett.*, 94:030502, 2005.
- [112] B. Lounis and M. Orrit. Single-photon sources. *Rep. Prog. Phys.*, 68:1129–1179, 2005.
- [113] T. P. Bodiya and L.-M. Duan. Scalable generation of graph-state entanglement through realistic linear optics. *Phys. Rev. Lett.*, 97:143601, 2006.
- [114] P. Michler, A. Kiraz, C. Becher, W. V. Schoenfeld, P. M. Petroff, L. D. Zhang, E. Hu, and A. Imamoglu. A quantum dot single-photon turnstile device. *Science*, 290:2282–2285, 2000.
- [115] C. Santori, M. Pelton, G. Solomon, Y. Dale, and Y. Yamamoto. Triggered single photons from a quantum dot. *Phys. Rev. Lett.*, 86:1502–1505, 2001.
- [116] C. Santori, D. Fattal, J. Vuckovic, G. S. Solomon, and Y. Yamamoto. Single-photon generation with InAs quantum dots. *New J. Phys.*, 6:89, 2004.
- [117] Axel Kuhn, Markus Hennrich, and Gerhard Rempe. Deterministic single-photon source for distributed quantum networking. *Phys. Rev. Lett.*, 89:067901, 2002.
- [118] J. McKeever, A. Boca, A. D. Boozer, R. Miller, J. R. Buck, A. Kuzmich, and H. J. Kimble. Deterministic generation of single photons from one atom trapped in a cavity. *Science*, 303:1992–1994, 2004.
- [119] M. Keller, B. Lange, K. Hayasaka, W. Lange, and H. Walther. Continuous generation of single photons with controlled waveform in an ion-trap cavity system. *Nature*, 431:1075–1078, 2004.
- [120] C. Kurtsiefer, S. Mayer, P. Zarda, and H. Weinfurter. Stable solid-state source of single photons. *Phys. Rev. Lett.*, 85:290–293, 2000.
- [121] C. W. Chou, S. V. Polyakov, A. Kuzmich, and H. J. Kimble. Single-photon generation from stored excitation in an atomic ensemble. *Phys. Rev. Lett.*, 92:213601, 2004.
- [122] P. Grangier, G. Roger, and A. Aspect. Experimental evidence for a photon anticorrelation effect on a beam splitter: a new light on single-photon interferences. *Europhys. Lett.*, 1:173–179, 1986.
- [123] D. A. Steck. *Rubidium 87 D line data*. <http://george.ph.utexas.edu/~dsteck/alkalidata>, 2003.
- [124] J. F. Clauser and M. A. Horne. Experimental consequences of objective local theories. *Phys. Rev. D*, 10:526–535, 1974.
- [125] D. M. Harber, H. J. Lewandowski, J. M. McGuirk, and E. A. Cornell. Effect of cold collisions on spin coherence and resonance shifts in a magnetically trapped ultracold gas. *Phys. Rev. A*, 66:053616, 2002.
- [126] R. Prevedel, P. Walther, F. Tiefenbacher, P. Böhi, R. Kaltenbaek, T. Jennewein, and A. Zeilinger. High-speed linear optics quantum computing using active feed-forward. *Nature*, 445:65–69, 2007.
- [127] Tao Yang, Qiang Zhang, Teng-Yun Chen, Shan Lu, Juan Yin, Jian-Wei Pan, Zhi-Yi Wei, Jing-Rong Tian, and Jie Zhang. Experimental synchronization of independent entangled photon sources. *Phys. Rev. Lett.*, 96(11):110501, 2006.

- [128] R. Kaltenbaek, B. Blauensteiner, M. Żukowski, M. Aspelmeyer, and A. Zeilinger. Experimental interference of independent photons. *Phys. Rev. Lett.*, 96:240502, 2006.
- [129] P. G. Kwiat, K. Mattle, H. Weinfurter, A. Zeilinger, A. V. Sergienko, and Y. Shih. New high-intensity source of polarization-entangled photon pairs. *Phys. Rev. Lett.*, 75:4337–4341, 1995.
- [130] D. A. Braje, V. Balić, S. Goda, G. Y. Yin, and S. E. Harris. Frequency mixing using electromagnetically induced transparency in cold atoms. *Phys. Rev. Lett.*, 93:183601, 2004.
- [131] T. Legero, T. Wilk, A. Kuhn, and G. Rempe. Time-resolved two-photon quantum interference. *Appl. Phys. B*, 77:797, 2003.
- [132] T. Legero, T. Wilk, M. Hennrich, G. Rempe, and A. Kuhn. Quantum beat of two single photons. *Phys. Rev. Lett.*, 93:070503, 2004.
- [133] Y. H. Shih and C. O. Alley. New type of Einstein-Podolsky-Rosen-Bohm experiment using pairs of light quanta produced by optical parametric down conversion. *Phys. Rev. Lett.*, 61:2921, 1988.
- [134] W. D. Phillips. *Optical Traps and Optical Molasses*. in *Fundamental Systems in Quantum Optics*, Les Houches, 1990 Session LIII.
- [135] C. H. Bennett. "Quantum and classical information: Transmission and computation". *Physics Today*, 48(10):24–30, 1995.
- [136] J.-W. Pan, M. Daniell, S. Gasparoni, G. Weihs, and A. Zeilinger. Experimental demonstration of four-photon entanglement and high-fidelity teleportation. *Phys. Rev. Lett.*, 86:4435, 2001.
- [137] H. de Riedmatten, I. Marcikic, W. Tittel, H. Zbinden, D. Collins, and N. Gisin. Long distance quantum teleportation in a quantum relay configuration. *Phys. Rev. Lett.*, 92:047904, 2004.
- [138] A. Kuzmich and E. S. Polzik. Atomic quantum state teleportation and swapping. *Phys. Rev. Lett.*, 85(26):5639, December 2000.
- [139] J. F. Sherson, H. Krauter, R. K. Olsson, B. Julsgaard, K. Hammerer, I. Cirac, and E. S. Polzik. Quantum teleportation between light and matter. *Nature*, 443:557–560, 2006.
- [140] A. Furusawa, J. L. Sørensen, S. L. Braunstein, C. A. Fuchs, H. J. Kimble, and E. S. Polzik. Unconditional quantum teleportation. *Science*, 282:706–709, 1998.
- [141] I. Marcikic, H. de Riedmatten, W. Tittel, H. Zbinden, and N. Gisin. Long-distance teleportation of qubits at telecommunication wavelengths. *Nature*, 421:509–513, 2003.
- [142] W. Tittel, J. Brendel, H. Zbinden, and N. Gisin. Quantum cryptography using entangled photons in energy-time bell states. *Phys. Rev. Lett.*, 84:4737–4740, 2000.
- [143] D. N. Matsukevich, T. Chanelière, M. Bhattacharya, S.-Y. Lan, S. D. Jenkins, T. A. B. Kennedy, and A. Kuzmich. Entanglement of a photon and a collective atomic excitation. *Phys. Rev. Lett.*, 95:040405, 2005.
- [144] S.-Y. Lan, S. D. Jenkins, T. Chaneliere, D. N. Matsukevich, C. J. Campbell, R. Zhao, T. A. B. Kennedy, and A. Kuzmich. Dual species matter qubit entangled with light. *Phys. Rev. Lett.*, 98:123602, 2007.
- [145] J. T. Barreiro, N. K. Langford, N. A. Peters, and Paul G. Kwiat. Generation of hyperentangled photon pairs. *Phys. Rev. Lett.*, 95:260501, 2005.
- [146] O. Gühne, P. Hyllus, D. Bruß, A. Ekert, M. Lewenstein, C. Macchiavello, and A. Sanpera. Detection of entanglement with few local measurements. *Phys. Rev. A*, 66:062305, 2002.
- [147] D. L. Moehring, P. Maunz, S. Olmschenk, K. C. Younge, D. N. Matsukevich, L.-M. Duan, and C. Monroe. Entanglement of single-atom quantum bits at a distance. *Nature*, 449:68–71, 2007.

-
- [148] T. Wilk, S. C. Webster, A. Kuhn, and G. Rempe. Single-atom single-photon quantum interface. *Science*, 317:488–490, 2007.
- [149] S. Chen, Y.-A. Chen, B. Zhao, Z.-S. Yuan, J. Schmiedmayer, and J.-W. Pan. Demonstration of a stable atom-photon entanglement source for quantum repeaters. *Phys. Rev. Lett.*, 99:180505, 2007.
- [150] Z.-S. Yuan, Y.-A. Chen, B. Zhao, S. Chen, J. Schmiedmayer, and J.-Wei Pan. Entanglement swapping between light and matter: A building block of quantum repeaters. <http://arxiv.org/abs/0803.1810>.
- [151] N. Davidson, H. J. Lee, C. S. Adams, M. Kasevich, and S. Chu. Long atomic coherence times in an optical dipole trap. *Phys. Rev. Lett.*, 74:1311, 1995.
- [152] K. M. O’Hara, S. R. Granade, M. E. Gehm, T. A. Savard, S. Bali, C. Freed, and J. E. Thomas. Ultrastable co2 laser trapping of lithium fermions. *Phys. Rev. Lett.*, 82:4204, 1999.
- [153] A. Corney. *Atomic and Laser Spectroscopy* (Clarendon. Press, Oxford, UK, 1977.
- [154] H. J. Lewandowski, D. M. Harber, D. L. Whitaker, and E. A. Cornell. Observation of anomalous spin-state segregation in a trapped ultracold vapor. *Phys. Rev. Lett.*, 88:070403, 2002.
- [155] M. D. Barrett, J. A. Sauer, and M. S. Chapman. All-optical formation of an atomic bose-einstein condensate. *Phys. Rev. Lett.*, 87:010404, 2001.
- [156] R. H. Dicke. The effect of collisions upon the doppler width of spectral lines. *Phys. Rev.*, 89:472, 1953.
- [157] C.-S. Chuu, F. Schreck, T. P. Meyrath, J. H. Hanssen, G. N. Price, and M. G. Raizen. Direct observation of sub-poissonian number statistics in a degenerate bose gas. *Phys. Rev. Lett.*, 95:260403, 2005.
- [158] T. Kuga, Y. Torii, N. Shiokawa, T. Hirano, Y. Shimizu, and H. Sasada. Novel optical trap of atoms with a doughnut beam. *Phys. Rev. Lett.*, 78:4713, 1997.
- [159] C. Mewes and M. Fleischhauer. Decoherence in collective quantum memories for photons. *Phys. Rev. A*, 72:022327, 2005.